

Novel Ruthenium(II/III) Complexes with Multidentate Schiff Base Chelates Containing Biologically Relevant Moieties.

by

Sanam Maikoo

Submitted in the fulfilment of the requirements for the degree of

Master of Science

In the School of Chemistry and Physics at the

University of KwaZulu-Natal

March 2014

Supervisor: Dr. Irvin N. Booysen

As the candidates supervisor I have approved this dissertation for
submission:

Signed: _____

Date: _____

Table of Contents

Abstract	i
Preface	iv
Declaration 1 – Plagiarism	v
Declaration 2 – Publications	vi
Acknowledgements	viii
Crystallographic Data	ix

Chapter 1

Introduction

1.1	General Background	1
1.2	Aim and Motivation	2
1.3	Schiff Bases and Benz(imidazole/othiazole) Compounds	6
1.4	Ruthenium Metallopharmaceuticals	9
1.5	General Chemistry of Ruthenium(II/ III)	11
1.6	Coordination Chemistry of Ruthenium (II/III)	14
1.7	References	18

Chapter 2

Experimental

2.1	Handling of Ruthenium	22
2.2	Materials	22

2.3	Synthetic Procedures of Schiff Base Ligands	23
2.4	Instrumentation	27
2.5	References	29

Chapter 3

Ruthenium(II) and (IV) complexes with potentially tridentate Schiff base chelates containing the Uracil moiety

3.1	Introduction	31
3.2	Experimental	33
3.3	X-Ray Crystallography	35
3.4	Computational Details	35
3.5	Results and Discussion	36
3.6	References	58

Chapter 4

Novel Ruthenium(II) and (III) compounds with Multidentate Schiff base chelates bearing the Chromone or 4-Aminoantipyrine moieties

4.1	Introduction	61
4.2	Experimental	62
4.3	X-Ray Crystallography	63
4.4	Results and Discussion	64
4.5	References	80

Chapter 5

Isolation of Ruthenium compounds from the analogous chelating behaviour of 2-Hydroxyphenylbenz(imidazole/othiazole)

5.1	Introduction	82
5.2	Experimental	84
5.3	X-Ray Crystallography	85
5.4	Computational Details	85
5.5	Results and Discussion	86
5.6	References	104

Chapter 6

Conclusion

	Conclusion and Future Work	106
--	-----------------------------------	------------

Abstract

The discovery of novel ruthenium metallopharmaceuticals is highly dependent on its coordination chemistry. As emphasized in Chapter 1, the biodistribution pathway of a potential ruthenium metallopharmaceutical depends on its oxidation state, aqueous solubility and the size of its metallic core. Recent developments are geared towards the utilization of biocompatible ligands which may facilitate biodistribution and fine-tune solubility in the blood stream of the formulated ruthenium anticancer agents. This design approach has motivated us to explore the coordination behaviour of multidentate N-donor ligands incorporating various biologically active components (*viz.* uracil, antipyrine, chromone or benz(imidazole/othiazole) moieties) towards the diamagnetic ruthenium(II) core. The resultant ruthenium compounds were characterized *via* various spectroscopic techniques and structural elucidations were confirmed using single X-ray analysis. The structural elucidations were complemented with electro-analytical and DFT studies.

In Chapter 3, the coordination reactions of *trans*-[Ru^{II}Cl₂(PPh₃)₃] with Schiff bases derived from 5,6-diamino-1,3-dimethyl uracil (H₂ddd) are reported. In the diamagnetic ruthenium(II) complexes, *trans*-[RuCl(PPh₃)₂(Htdp)](**1**) {H₂tdp = 5-((thiophen-3-yl)methyleneamino)-6-amino-1,3-dimethyluracil} and *trans*-[RuCl(PPh₃)₂(Hsdp)](**2**) {H₂sdp = 5-(2-(methylthio)benzylideneamino)-6-amino-1,3-dimethyluracil}, the Schiff base ligands (*i.e.* Htdp and Hsdp) act as monoanionic tridentate chelators. Similarly, the diimine H₃ucp chelator coordinated as a

monoanionic tridentate moiety in complex **3**, $[\text{Ru}^{\text{II}}\text{Cl}(\text{PPh}_3)(\text{H}_3\text{ucp})]$ (H_4ucp = 2,6-bis-((6-amino-1,3-dimethyluracilimino)methylene)pyridine). Upon reacting 5-(2-hydroxybenzylideneamino)-6-amino-1,3-dimethyluracil (H_3hdp) with the metal precursor, the paramagnetic complex, *trans*- $[\text{Ru}^{\text{IV}}\text{Cl}_2(\text{ddd})(\text{PPh}_3)_2]$ (**4**) was isolated, in which the bidentate dianionic ddd co-ligand was formed by hydrolysis. The presence of the paramagnetic metal centre for **4** was confirmed by ESR spectroscopy. DFT studies of complex **3** were conducted to provide insight into its intrinsic solid state structural features. The redox properties were probed *via* cyclic voltammetry: complexes **1**, **2** and **4** exhibited comparable electrochemical behaviour with half-wave potentials ($E_{1/2}$) at 0.70 V (for **1**), 0.725 V (for **2**) and 0.68 V (for **4**) *vs* Ag|AgCl respectively while the attained half-wave potential (0.37 V *vs* Ag|AgCl) of **3** was significantly lower.

Chapter 4 focuses on the isolation of novel ruthenium(II/III) compounds from the respective reactions of the metal precursor, *trans*- $[\text{RuCl}_2(\text{PPh}_3)_3]$ with multidentate Schiff base ligands bearing the chromone and antipyrine moieties. From these coordination reactions of *trans*- $[\text{RuCl}_2(\text{PPh}_3)_3]$ with 4-((pyridine-2-ylimino)methylene)-chromone (pch) and 2,6-bis-((antipyrine-imino)methylene)pyridine (bpap); the ruthenium(II/III) complexes: *trans*-P, *cis*-Cl- $[\text{Ru}^{\text{III}}(\text{pch})\text{Cl}_2(\text{PPh}_3)_2]$ (**1**) and *cis*- $[\text{RuCl}_2(\text{bpap})(\text{PPh}_3)]$ (**2**) were formed, respectively. The presence of the paramagnetic metal centre of **1** was confirmed *via* room temperature solution ESR spectroscopy. The more delocalized nature of the diimine chelator of **2** promotes faster electron transfer resulting in a lower redox potential in

contrast to the mono-imine chelator of **1**. The electronic spectra of the metallic compounds exhibited common intraligand π - π^* and red-shifted Metal-to-Ligand-Charge-Transfer electronic transitions whilst a d - d electronic transition was only observed for the paramagnetic compound **1**.

In Chapter 5, the analogous chelating behaviour of bidentate N,O-donor heterocyclic ligands which coordinated in a '2+2' coordination mode, is described. The 1:2 molar ratio reactions of *trans*-[RuCl₂(PPh₃)₃] with 2-hydroxyphenylbenzimidazole (Hobz) and 2-hydroxyphenylbenzothiazole (Hobs), respectively led to the formation of the diamagnetic ruthenium(II) complex salt, [RuCl(Hobz)₂(PPh₃)]Cl (**1**) as well as the paramagnetic ruthenium complex, [Ru^{III}Cl(obs)₂(PPh₃)] (**2**). The X-ray crystal structures of both metallic compounds confers a distorted octahedral geometry imposed by the mutual '2+2' coordination modes of the chelators. DFT studies indicated that the complex cation of **1** was more energetically favourable than the neutral complex **2**. Solid state ESR analysis of the paramagnetic complex **2** gave rise to a distorted rhombic spectra whilst the liquid state ESR afforded an isotropic singlet (at 298 K) and three distinctive signals (at 77 K).

Keywords: Ruthenium (II/III/IV); Schiff base ligands; Electron Spin Resonance (ESR); Voltammetric analysis; Density functional Theory (DFT); Chromone; Antipyrine; Uracil; Electronic Spectra; Heterocyclic, Benz(imidazole/othiazole), X-ray crystal structures.

Preface

The experimental work in this dissertation was carried out in the School of Chemistry and Physics, University of KwaZulu-Natal, Pietermaritzburg, from January 2013 to March 2014, under the supervision of Doctor Irvin N. Booysen.

These studies represent original work by the author and have not otherwise been submitted in any form for any other degree or diploma to any tertiary institution. Where use has been made of the work of others, it is duly acknowledged in the text.

Declaration 1 – Plagiarism

I, Sanam Maikoo, declare that:

1. The research reported in this dissertation, except where otherwise indicated, is my original research.
2. This dissertation has not been submitted for any degree or examination at any other university.
3. This dissertation does not contain any other persons' data, pictures, graphs or other information, unless specifically acknowledged as being sourced from other persons'.
4. This dissertation does not contain any other persons' writing, unless specifically acknowledged as being sourced from other researchers. Where other written sources have been quoted, then:
 - a. Their words have been re-written but the general information attributed to them has been referenced.
 - b. Where their exact words have been used, then their writing has been placed in italics and inside quotation marks, and referenced.
5. This dissertation does not contain text, graphics or tables copied and pasted from the internet, unless specifically acknowledged, and the source being detailed in the dissertation and in the references section.

Signed: _____

Declaration 2 – Publications

Manuscripts Published

- Booysen, I.N., Maikoo, S., Akerman, M.P., Xulu, B., Munro, O. "Ruthenium(II/IV) complexes with potentially tridentate Schiff base chelates containing the uracil moiety." *J. Coord. Chem.*, 2013, **66**, 3673.
- Booysen, I.N., Maikoo, S., Akerman, M.P., Xulu, B. "Novel Ruthenium(II) and (III) compounds with Multidentate Schiff base chelates bearing biologically significant moieties." *Polyhedron*, 2014, in press, <http://dx.doi.org/10.1016/j.poly.2014.05.021>.

In Preparation

- Booysen, I.N., Maikoo, S., Akerman, M.P., Xulu, B. "Isolation of ruthenium compounds from the analogous chelating behaviour of 2-hydroxyphenylbenz(imidazole/othiazole)." *Trans. Met. Chem.*, 2014.

The formulated compounds in the aforementioned manuscripts have been synthesized, characterized and analysed by myself. For publication 1, single crystal samples were run and solved by Prof. O. Munro and Dr M. Akerman. The ESR spectrum was run by Dr B. Xulu and the paper was written by Dr I. Booysen for publication. For the manuscript submitted for review, single crystal samples were run and solved by Dr M. Akerman. The ESR spectrum was run by Dr B. Xulu. Dr I. Booysen, wrote the paper for submission. The article currently in preparation is being written by Dr I. Booysen. The single crystal XRD samples were run and solved by Dr M. Akerman and the ESR spectra was run by Dr B. Xulu.

Signed: _____

Sanam Maikoo

Signed: _____

Dr I.N. Booysen

Signed: _____

Prof. O.Q. Munro

Signed: _____

Dr M.P. Akerman

Signed: _____

Dr B. Xulu

Acknowledgements

I would like to express my first debt of gratitude to my supervisor, Dr. Irvin N. Booysen for his never ending patience, the countless hours of his time as well as the fine balance of intellectual support and guidance that he has provided to me during this study.

Furthermore, I would also like to express my appreciation to our research group, M. Ismail, T. Hlela, A. Adebisi and S. Chohan as well as my other chemistry colleagues and friends, S. Seunarian, S. Bhikraj, L. Hunter, L. Dralle, V. Chiazzari and T. Zacca for their help and support.

In addition, I am grateful to Prof. O.Q. Munro and Dr. M.P Akerman for running our single crystal X-ray crystallographic samples and to Dr. B.X. Xulu for attaining our raw Electron Spin Resonance data.

My studies would not have been conceivable without my mum, Prema Maikoo. In particular, her love, support and many sacrifices she has made for me. I would also like to thank my father, Subhash Maikoo, for his encouragement and support.

I am thankful towards the University of KwaZulu-Natal for providing me with the laboratory and equipment required for this study.

Lastly, but most importantly, I am highly grateful to God for the courage and strength that has made me who I am today.

Crystallographic Data

Supplementary data for all the crystal structures obtained during this study are stored on a compact disk that is attached to the inside back cover of this dissertation.

This data includes the following:

- Final coordinates and equivalent isotropic displacement parameters of the non-hydrogen atoms;
- Final crystal data and details of the structure determinations;
- Isotropic displacement parameters;
- Hydrogen atom positions;
- Contact distances;
- Torsion angles;
- Hydrogen-bonds.

Chapter 1

Introduction

1.1 General Background

Ruthenium is a $4d$ element with an atomic number of 44. This rare transition metal is the 74th most abundant element on earth and occurs naturally in the ores of the platinum group metals, *e.g.* pyroxenite in South Africa. Seven natural occurring isotopes (*viz.* $^{96, 98-104}\text{Ru}$) are known while several radioisotopes have been discovered with atomic masses ranging from 87 to 124 [1, 2]. Furthermore, this metal $[\text{Kr}4d^75s^1]$ exhibits variable oxidation states ranging from 0 to +8 by utilizing its valence d - and s -electrons but can also extend into its krypton core attaining the -2 oxidation state, *e.g.* $[\text{Ru}(\text{CO})_4]^{2-}$ [3]. Characteristic to most d -block elements, the acidic cores of ruthenium are commonly stabilized by N^{3-} and O^{2-} moieties while lower oxidation states are stabilized by strong π -back bonding ligands like the carbonyls [4].

Numerous ruthenium complexes with N-donor heterocyclic chelators have been isolated due to the metal centre's characteristic affinity for neutral nitrogen donor atoms (*e.g.* pyridyl). Most recently, the discovery of NAMI-A, *trans*- $[\text{RuCl}_4(\text{DMSO})(\text{Im})](\text{ImH})$ {ImH = imidazole} as a potential metallopharmaceutical for metastatic cancer, has led to a renewed interest into the medicinal inorganic chemistry of ruthenium [5]. In addition, as a result of the emergence of ruthenium radiochemistry, the radio-therapeutic applications of the ^{106}Ru radionuclide have been widely investigated due to its optimal half-life (371.8 days) and β -max energy [3, 6].

Beside these promising medicinal applications, the rich organometallic chemistry of ruthenium coupled with its easily accessible oxidation states have afforded metal complexes with profound catalytic properties [7, 8]. This class of metal complexes is readily stabilized by either aliphatic (*e.g.* allyl) or aromatic (*e.g.* arene) carbon-based

cores [8, 9]. The most prominent of them all, is the Grubbs catalysts which are the most widely utilized organoruthenium catalyst in olefin metathesis [10].

1.2 Aim and Motivation

In the last decade, there has been a growing interest in the development of new ruthenium metallopharmaceuticals due to the discovery of NAMI-A, *trans*-[RuCl₄(DMSO)(Im)](ImH) {Im = imidazole}. NAMI-A has recently entered Phase II clinical trials due to its excellent metastatic cancer activity which is accompanied with fewer significant side effects than platinum-based metallopharmaceuticals [11]. Recent developments are geared towards the utilization of biocompatible ligands which may facilitate biodistribution and fine-tune solubility in the blood stream of the formulated ruthenium anticancer agents [12, 13]. This design approach has motivated us to explore the coordination behaviour of multidentate Schiff base ligands (incorporating biologically relevant moieties) as well as benz(othiazole/imidazole)-derived chelators (see **Figure 1.1**) towards the Ru^{II/III} cores. In particular, Schiff bases derived from 3-formylchromone, 4-aminoantipyrine and 5,6-diamino-1,3-dimethyluracil (H₂ddd) were considered in this study, see **Figures 1.2** and **1.3**.

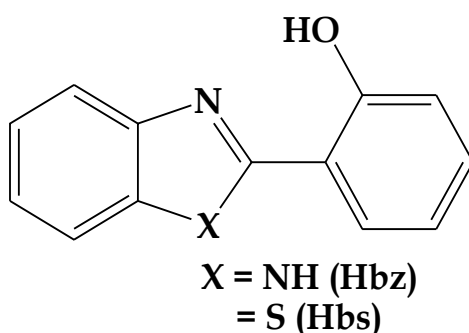
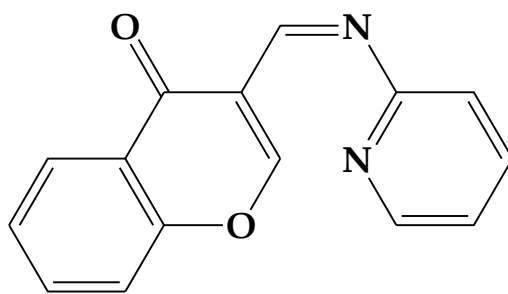
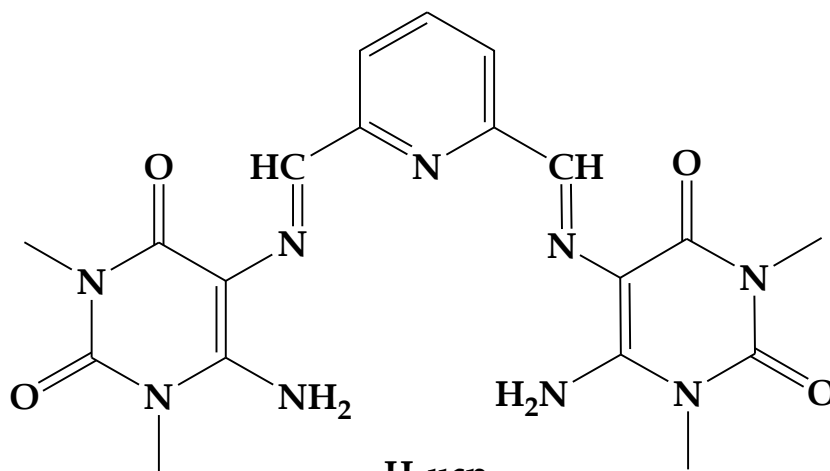


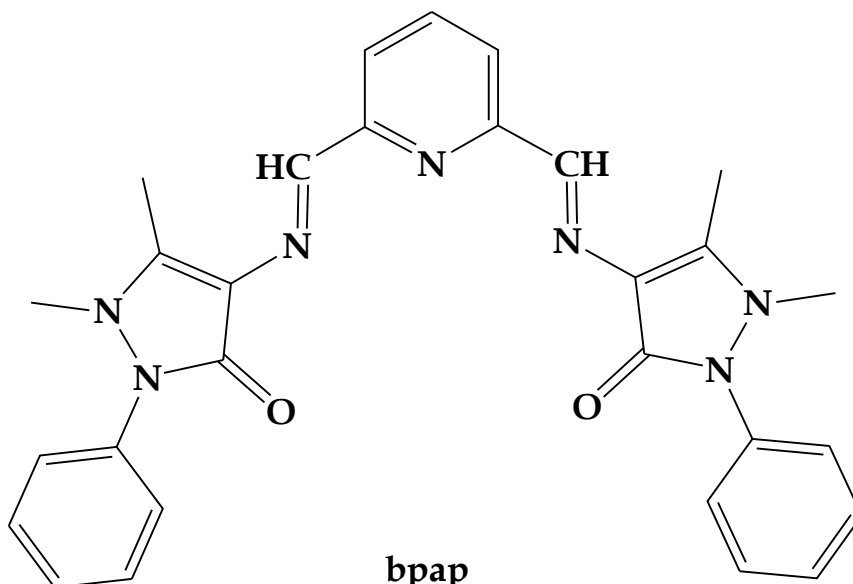
Figure 1.1: Generic structure of the heterocyclic ligands: 2-hydroxyphenyl-1H-benzimidazole (Hbz) and 2-hydroxyphenyl-1H-benzothiazole (Hbs).



pch



H₄ucp



bpap

Figure 1.2: Structures of 4-((pyridine-2-ylimino)methylene)-chromone (*pch*), 2,6-bis-((6-amino-1, 3-dimethyluracilimino)methylene)pyridine (*H₄ucp*) and 2,6-bis-((antipyrine-imino)methylene)pyridine (*bpap*).

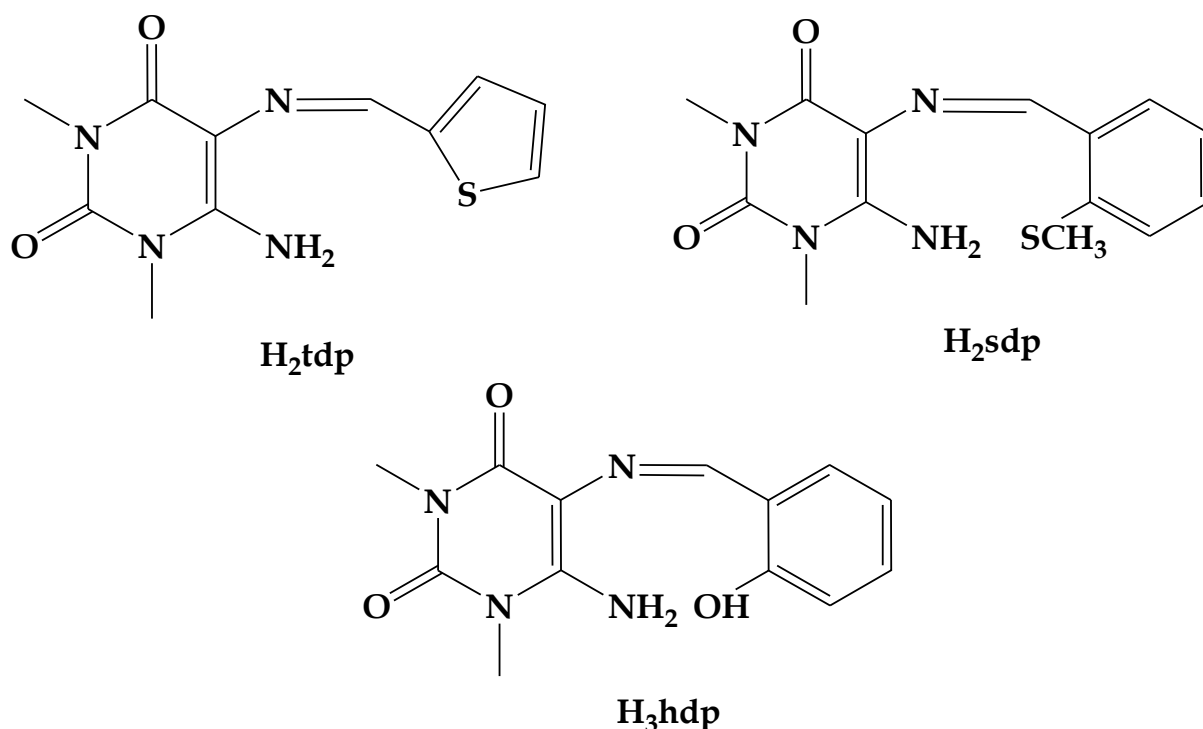


Figure 1.3: Structures of 5-((thiophen-3-yl)methyleneamino)-6-amino-1,3-dimethyluracil (H₂tdp), 5-(2-(methylthio)benzylideneamino)-6-amino-1,3-dimethyluracil (H₂sdp) and 5-(2-hydroxybenzylideneamino)-6-amino-1,3-dimethyluracil (H₃hdp).

Schiff bases are known to stabilize ruthenium in the oxidation states +II and +III which is emphasized by the metal center's preferential coordination affinity towards neutral nitrogen donor atoms, like imino and pyridyl nitrogens [14, 15]. Furthermore, the utilization of multidentate Schiff base ligands renders additional thermodynamic stability through the formation of chelate rings [16]. These organic molecules can also be readily synthesized by condensation reactions in either organic media or *via* solvent-free methods [17]. In addition, derivatization of Schiff bases allows for the incorporation of biomolecules and functionalization allows for manipulation of solubility in aqueous or organic media [18]. Due to the above reasons, many transition metal complexes have shown inherent and enhanced biological activities with respect to their free Schiff base ligands [19].

In particular, Schiff bases derived from 4-aminoantipyrine and their ruthenium complexes have shown an array of biological activities including antioxidant, antibacterial and anti-oxidant activities as well as DNA binding capability [20]. Like

in the case of the organometallic ruthenium(II) complex, $[\text{RuCl}(\text{CO})(\text{B})(\text{oap})]$ (Hoap = 4-((2-hydroxybenzylidene)imino)-aminoantipyrine, B = $\text{PPh}_3/\text{AsPh}_3/\text{py}$) containing the monoanionic $\text{O}_{\text{keto}}\text{N}_{\text{imino}}\text{O}$ tridentate oap chelator, showed optimal DNA cleavage activity [21]. Our selection of the chromone moiety is based on its biological relevance as a secondary metabolite. In addition, chromone Schiff base transition metals complexes have shown to exhibit excellent anti-tumour behaviour [22]. The motivation behind the use of 5,6-diamino-1,3-dimethyluracil is its biological relevance as a nucleotide base derivative as well as the fact that uracil-derivatives are well established chemotherapeutic drugs (*e.g.* uracil-mustard), see **Figure 1.4** [23].

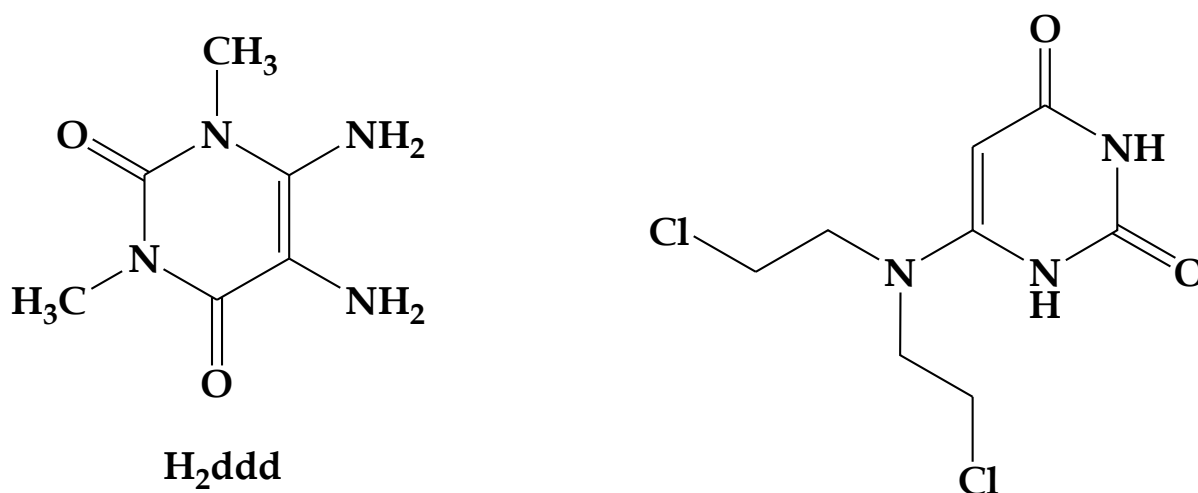


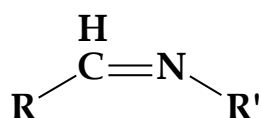
Figure 1.4: Structures of 5,6-diamino-1,3-dimethyluracil (H_2ddd) and uracil mustard.

Ruthenium complexes containing 2-pyridylbenz(imidazole/othiazole)-derived ligands have been widely investigated due to their excellent electrochemiluminescence (ECL) properties [24]. Indicative to the ruthenium Schiff base compounds, ruthenium complexes with these N-donor heterocyclic chelators have been found to exhibit numerous pharmacological activities such as anticancer, antifungal and antimicrobial properties [25]. The combinations of these ECL and biological properties have proven useful in the advancement towards new ruthenium diagnostic agents. For example, the DNA binding modes of a number of benzothiazole-substituted *tris*-bipyridine ruthenium(II) analogues were investigated by using fluorescent intercalator displacement studies [26].

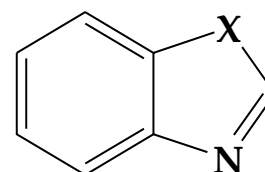
In this study, X-ray analysis indicated that the mono-imine and the highly delocalized diimine ligands afforded either bidentate, tridentate or tetradentate chelators whilst the heterocyclic ligands coordinated in a '2+2' manner to the ruthenium metal centre. The formulated ruthenium complexes showed comparable geometrical parameters as other ruthenium complexes found in the literature [27, 28].

1.3 Schiff Bases and Benz(imidazole/othiazole) Compounds

Schiff bases and benz(imidazole/othiazole) compounds are intriguing organic constituents which both contain sp^2 -hybridized carbon to nitrogen (C=N) double bonds where in Schiff bases the characteristic functional group is an aliphatic bridge R-C=N-R' while the C=N bonds of the benz(imidazole/othiazole) compounds forms part of constrained five-membered chelate rings, see **Figure 1.5** [14, 29, 30]. Derivatization and functionalization of their general structures have led to unique structure-activity relationships [31]. For this reason, Schiff bases with a wide range of biological activities have been isolated and benz(imidazole/othiazole) moieties are the building blocks of many commercially available pharmaceuticals [32, 33].



R or/and R' = aliphatic or aromatic groups



X = S (Benzothiazole)
or NH (Benzimidazole)

Figure 1.5: General structures of Schiff bases and benz(imidazole/othiazole) compounds.

Among the numerous examples is 2-dodecyloxy(benzylidene)-acetic acid which displays significant antitumor activity against a wide range of cell lines [34]. In addition, Riluzole (6-trifluoromethoxy-2-benzothiazolamine, (see **Figure 1.6**) is a drug used to treat lateral sclerosis as it was found to hinder glutamate neurotransmission

during electrophysiological and biochemical behavioural experiments [35]. Another example is the benzothiazole-derived radiopharmaceutical, Pittsburgh Compound B (see **Figure 1.7**) which is used for the diagnosis of amyloid plaques in the brain which is the primary cause of Alzheimer's disease [36]. Organic compounds containing benzimidazole moieties have also illustrated profound biological activities, like in the case of 4-(5,6-dimethyl-1*H*-benzimidazol-2-yl)benzene-1,3-diol which was found to display antiproliferative activity against the human bladder cancer cell lines, see **Figure 1.7** [37].

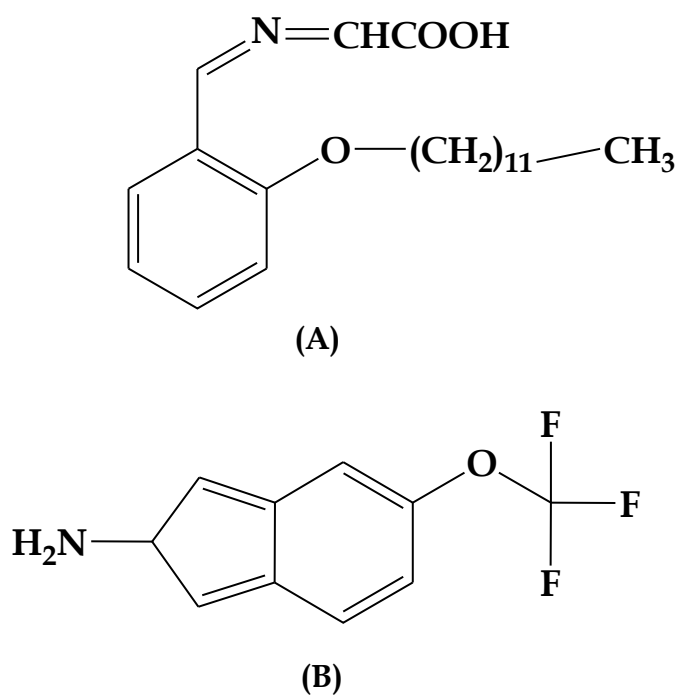
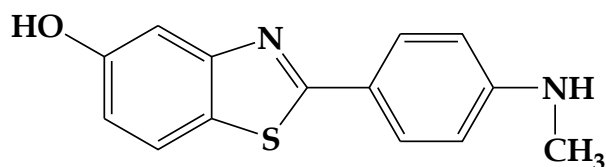
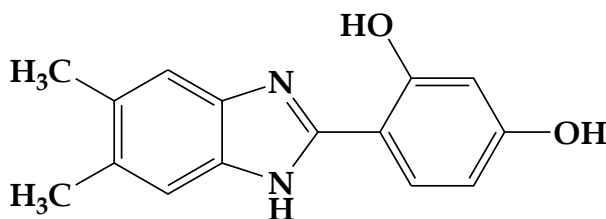


Figure 1.6: Structures of 2-dodecyloxy(benzylidene) acetic acid (A) and the drug, Riluzole (B).



(A)



(B)

Figure 1.7: Structures of Pittsburgh compound B (A) and 4-(5,6-Dimethyl-1H-benzimidazol-2-yl)benzene-1,3-diol (B).

Schiff bases and benz(imidazole/othiazole) compounds typically show higher biological activities upon coordination since the resultant metal complexes have shown stronger *in vivo* interactions *via* covalent or ionic bonding and also combines the unique stereo-electronic properties of their chelators for interactions with biological targets. Thus the increased activity is ascribed to stronger covalent interactions between the metal and the donor atoms of the biological target molecule. In addition, the metal is able to position the ligands in appropriate positions so that optimal interactions may occur between the biological target and the ligands. This metal-ligand synergistic relationship has been observed in numerous examples, *e.g.* complexes of M(II) {M = Ni, Co, Zn and Cu} containing a Schiff base (derived from 3-ethoxy-salicylaldehyde and 2-aminobenzoic acid) showed an increase in antibacterial activity compared to their free ligands [38, 39]. Also, the interaction of the copper(II) compound, Cu(bzap)(ClO₄)₂ (bzap = *N,N,N',N'*-tetrakis[(2-benzimidazolyl)methyl]-1,3-diaminopropane) with DNA was investigated and it was found that the complex is able to bind to the phosphate backbone of the DNA backbone and partially intercalate into the double helix due to the planarity of the highly conjugated, benzimidazole rings [40].

1.4 Ruthenium Metallopharmaceuticals

Cisplatin, *cis*-[Pt(NH₃)₂Cl₂] (see **Figure 1.8**) was the very first metal-based anticancer drug approved by the FDA in 1978 [41]. This metallo-drug destroys tumour cells *via* the interference of transcription and replication processes which subsequently triggers apoptosis [42]. However, there are numerous side effects that accompany the use of cisplatin and this could be attributed to the fact that it does not specifically target tumour cells but also targets other healthy cells in the body, such as, the rapidly dividing cells of the gastrointestinal tract, the hair follicles and bone marrow. This causes numerous side-effects like hair loss and nausea and in addition the development of drug resistance in tumour cells may occur [43]. Therefore, cancer treatment with the use of metal-based anticancer drugs requires selectivity for cancerous tissue; with no or little harm to normal healthy cells.

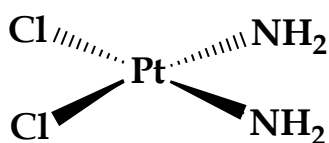


Figure 1.8: Structure of Cisplatin.

In comparison to platinum-based anticancer drugs, there are numerous traits of ruthenium compounds which make them promising for the design of novel antitumour drugs. Literature studies have shown that ruthenium anticancer drugs show antimetastatic activity (*i.e.* prevention of the spreading of cancer cells to other tissues or organs) in cells that have previously developed a resistance to cisplatin. These anticancer ruthenium-based drugs adopt biological mechanisms of activities which are highly dependent on their respective oxidation states. For example, selected ruthenium(III) complexes have been classified as pro-drugs which are activated through ‘activation by reduction’ theory. This reduction phenomenon induces more selective toxicity and is thought to be induced by the lower pH and oxygen content within tumour cells and by the covalent-binding of low-molecular weight biomolecules [44, 45, 46]. This is further supported by the fact that Pt(II) pro-drugs

and Ru(III) anticancer compounds have comparative substitution kinetics with various biological nucleophiles [47].

Ruthenium(III) complexes have also shown lower toxicity (compared to cisplatin) as these metallo-drugs target the cancer cells *via* transferrin receptors [48]. This is ascribed to the mimetic capability of ruthenium to its group congener iron's binding to transferrin, a protein found within mammals. In particular, the leading ruthenium anticancer compounds, NAMI-A and indazolium-*trans*-[tetrachloro-*bis*(1*H*-indazole)ruthenate(III)] (KP1019) are converted to the active Ru(II) species by the stepwise dissociation of two chlorides under physiological conditions, see **Figure 1.9**. These active species are able to bind to enzymes and proteins on tumour cell membranes and induces apoptosis *via* the mitochondrial pathway (for KP1019) or by interfering with type IV collagenolytic activity (for NAMI-A) [45, 49, 50, 51].

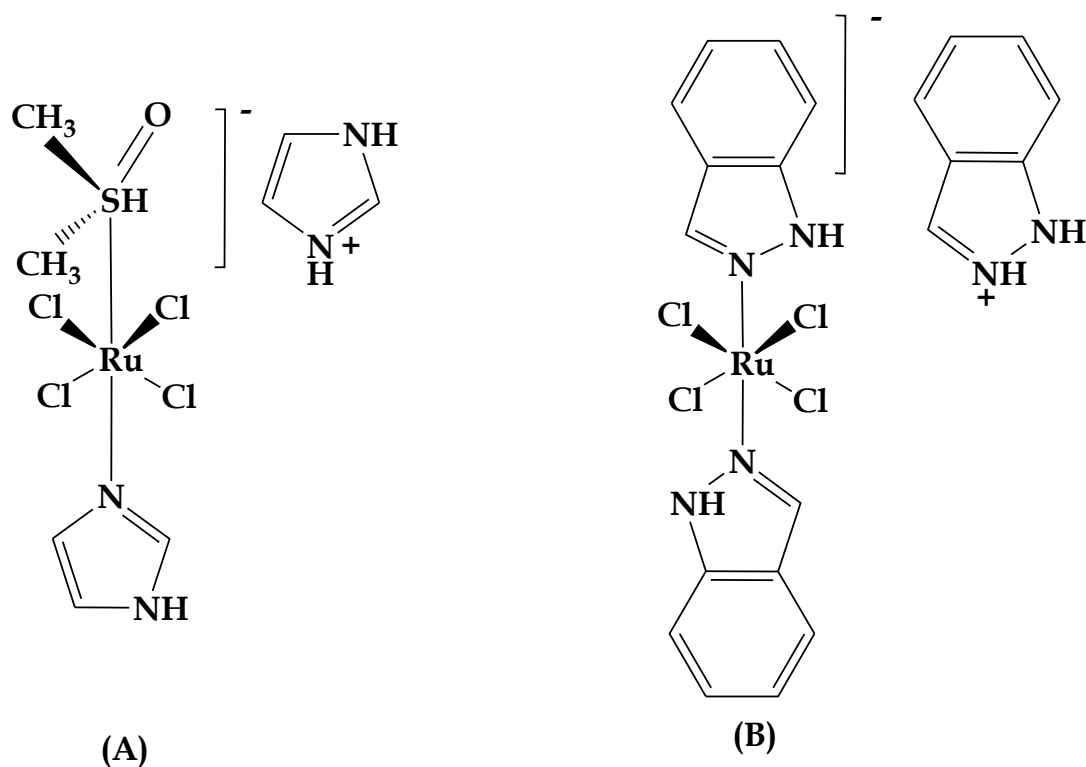


Figure 1.9: The leading candidates for the first ruthenium metallopharmaceuticals: NAMI-A (A) and KP1019 (B).

Furthermore, arene ruthenium(II) complexes have largely acted as Topoisomerase II inhibitors whereas octahedral saturated complexes containing the $[\text{Ru}(\text{bpy})_2]^{2+}$ core have been found to exhibit DNA interchelating activities. In addition, several ruthenium-nucleotide base complexes have been isolated which suggest that ruthenium complexes can also coordinate preferentially directly on the DNA double helix. For example, the organometallic ruthenium(II) complex, $[\text{RuCl}_2(p\text{-cymene})\text{adp}]$ (adp = 3-aza-5*H*-phenanthridin-6-one) have shown several modes of anticancer activity *via* DNA binding facilitated by the monodentate adp moiety as well as through inhibition of transcription and Poly(ADP-ribose) polymerase-1 (PARP-1), see **Figure 1.10** [52].

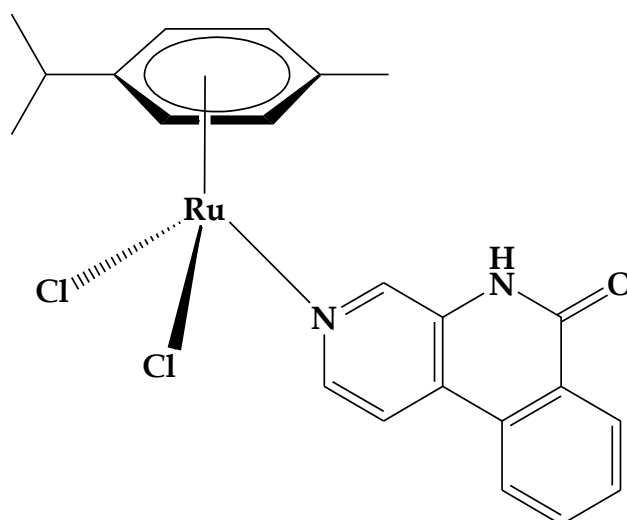


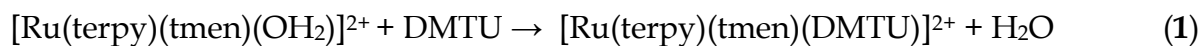
Figure 1.10: Structure of the metal-based DNA interchelator, $[\text{RuCl}_2(\text{cymene})\text{adp}]$.

1.5 General Chemistry of Ruthenium(II/ III)

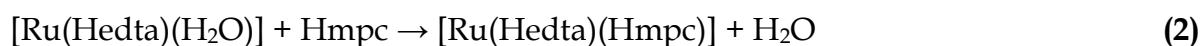
1.5.1 Ligand Substitution

The low-spin ruthenium(II) centre is predominately kinetically inert but ligand substitution can be promoted by utilizing metal precursors (*e.g.* *cis*- $[\text{RuCl}_2(\text{bpy})]$, *trans*- $[\text{RuCl}_2(\text{PPh}_3)_3]$ and $(\mu\text{-Cl})_2[\text{RuCl}(p\text{-cymene})]_2$ with labile co-ligands within their coordination spheres [53]. For example, substitution kinetic studies of the ruthenium(II) complexes, $[\text{Ru}(\text{terpy})(\text{tmen})(\text{OH}_2)]^{2+}$ (terpy = 2,2': 6',2''-terpyridine,

bipy = 2,2'-bipyridine and tmen = *N,N,N',N'*-tetramethylethylenediamine) suggests that the metal complex bearing the more π -conjugated tmen bidentate chelator aids faster ligand exchange of DMTU (1,3-dimethyl-2-thiourea), refer to **Equation (1)** [54].

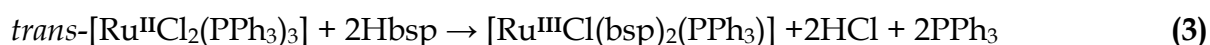


Indicative to the aforementioned, the paramagnetic ruthenium(III) complex, $[\text{Ru}(\text{edta})(\text{H}_2\text{O})]$ (H_3edta = ethylenediaminetetraacetic acid) undergoes dehydration upon the reaction with 2-mercaptophenylcarboxylate (Hmpc); retaining the low-spin d^5 metal centre in $[\text{Ru}(\text{Hedta})(\text{Hmpc})]$ [55], refer to **Equation (2)**.



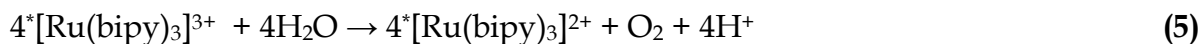
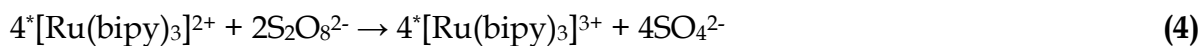
1.5.2 Redox Reactions

Ruthenium complexes in its oxidation states +II and +III are typically highly redox active and therefore are prone to ligand-induced oxidation and reduction reactions. This can be seen in **Equation (3)** in the formation of the '2+2' ruthenium(III) complex, $[\text{Ru}^{\text{III}}\text{Cl}(\text{bsp})_2(\text{PPh}_3)]$ (Hbsp = *N*-(2-hydroxybenzylidene)-benzimidazole) from the diamagnetic metal precursor, *trans*- $[\text{Ru}^{\text{II}}\text{Cl}_2(\text{PPh}_3)_3]$ [56].



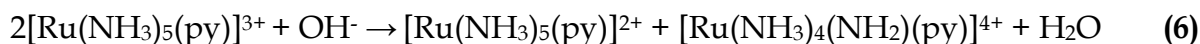
Some ruthenium(III) complexes also have the propensity to be oxidized to its $\text{Ru}^{+\text{IV}}$ or $\text{Ru}^{+\text{V}}$ species by oxidants such as O_2 and H_2O_2 . A typical example is the ruthenium(III) polyaminecarboxylato complex $[\text{Ru}^{\text{III}}(\text{edta})(\text{H}_2\text{O})]^-$ which is oxidized by a reaction with H_2O_2 to produce the $[\text{Ru}^{\text{V}}(\text{edta})(\text{O})]^-$ specie which is used in the hydroxylation of arginine [57, 58]. Furthermore, ruthenium(II) polypyridyl complexes have a tendency to be converted to its excited state by visible light which is subsequently reduced or oxidized by appropriate quenching agents. This excited state seems to result from the transfer of an electron from the metal t_{2g} orbitals to the ligand π^* orbital [59]. For

example, during the photocatalytic oxidation of water to produce dimolecular oxygen; the excited $^*[Ru(bipy)_3]^{3+}$ (bipy = bipyridine) is generated from the oxidation of $^*[Ru(bipy)_3]^{2+}$ by an oxidant, $S_2O_8^{2-}$, refer to **Equations (4) and (5)** [60].

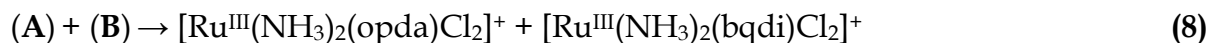


1.5.3 Disproportionation

The disproportionation reactions of ruthenium(II/III) complexes have been extensively studied due to the relevance of the products (as oxidants and reductants) in organometallic catalysis and in DNA-oxidation studies [61, 62]. More specifically, ruthenium(III) complexes have been known to disproportionate into Ru^{II} and Ru^{IV} species under basic conditions. Taube *et al.* reported the disproportionation of $[Ru^{III}(NH_3)_5(py)]$ under basic conditions which yielded $[Ru^{II}(NH_3)_5(py)]$ and $[Ru^{IV}(NH_3)_4(NH_2)(py)]$ [63], refer to **Equation (6)**.



Disproportionation for ruthenium(II) complexes are not common but similar to the abovementioned example, a very unusual proton-assisted disproportionation, involving the complex $Ru^{II}(NH_3)_2(bqdi)Cl_2$ (bqdi = *o*-benzoquinonediimine), was reported by Kapovsky *et al.* It was observed that the complex, $[Ru^{II}(NH_3)_2(bqdi)Cl_2]$ (**A**) undergoes disproportionation, upon exposure to ultraviolet-visible light, forming the two final ruthenium(III) species (one reductant and one oxidant), refer to **Equations (7) and (8)**. Initially, the intermediate **B**, $[Ru^{IV}(NH_3)_2(opda)Cl_2]^{2+}$ (opda = 1,2-phenylenediamine) is formed *via* the protonation of the diimine nitrogen donors of the bqdi moiety. The resultant intermediate (**B**) induces oxidation of the remaining molecules of (**A**) to afford the paramagnetic complex cations, $[Ru^{III}(NH_3)_2(opda)Cl_2]^+$ and $[Ru^{III}(NH_3)_2(bqdi)Cl_2]^+$ [62].



1.6 Coordination Chemistry of Ruthenium (II/III)

1.6.1 Ruthenium Compounds with N, N-donor ligands

Ruthenium demonstrates a general affinity towards neutral nitrogen-donor atoms like imino and pyridyl nitrogens [64, 65]. Typical examples includes the ruthenium(II) compounds $[\text{Ru}(\text{bbz})\text{Cl}(\text{PPh}_3)]^+$ (bbz = *N,N'*-bis(benzimidazol-2-yl-ethyl)ethylenediamine) and *trans*- $[\text{RuCl}(\text{trpy})(\text{PPh}_3)_2](\text{PF}_6)$ (trpy = 4,4',4''-tri-*t*-butyl-2,2':6',2''-terpyridine), see **Figures 1.11** and **1.12** [66, 67]. However, high and low oxidation states of ruthenium are readily stabilized by the deprotonated forms of nitrogen-donor atoms (*e.g.* amido) as these function as good σ -donors [68]. Therefore, it comes as no surprise that the majority of ruthenium compounds contain multidentate N-donor ligands.

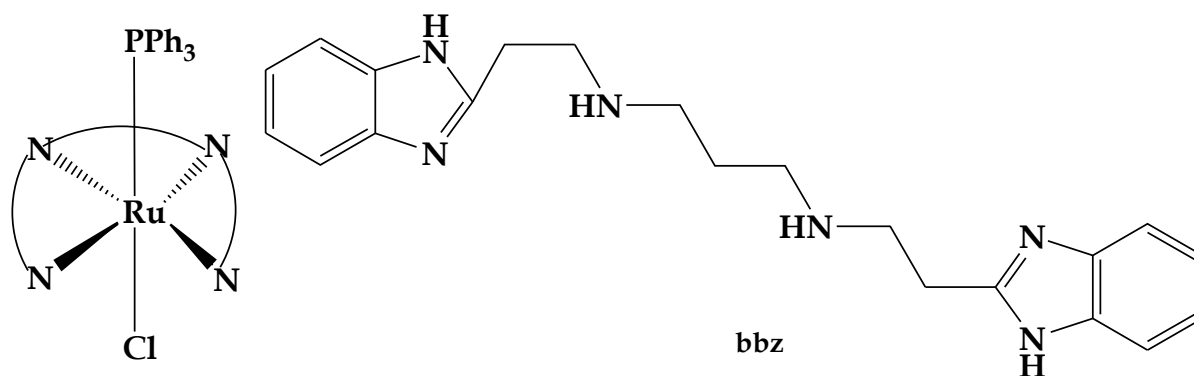


Figure 1.11: Structures of the free bbz ligand and its corresponding complex cation illustrating the neutral tetradentate moiety occupying the equatorial position.

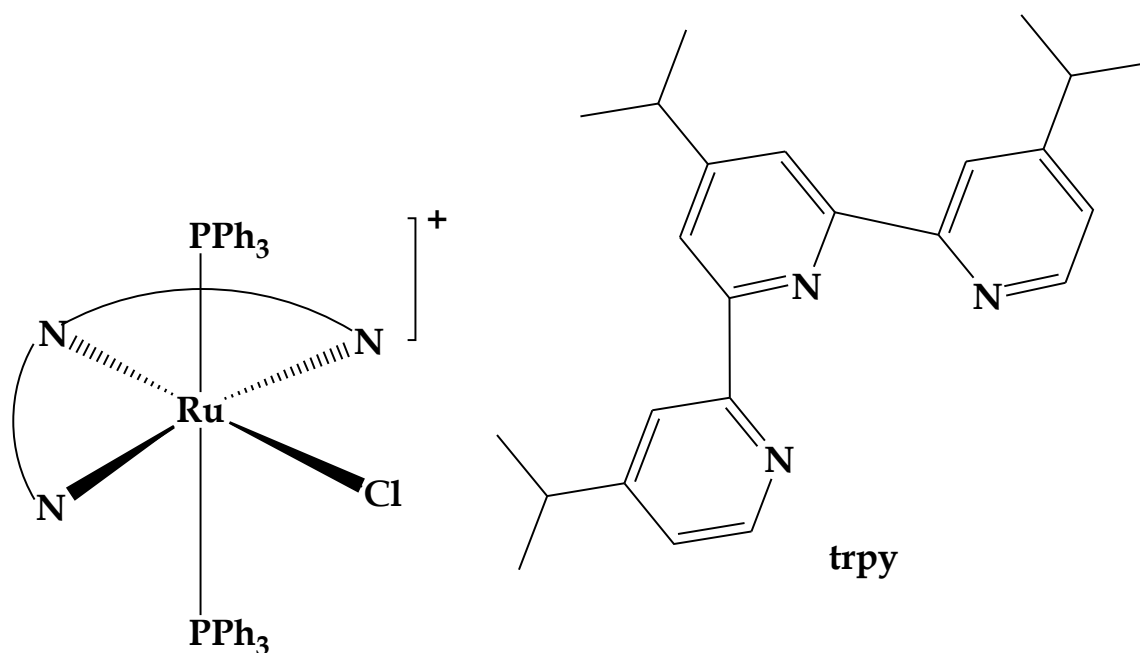


Figure 1.12: Structure of the $\text{trans-[RuCl(trpy)(PPh}_3)_2]^+$ ion and its free trpy ligand which acts as a neutral tridentate chelator.

1.6.2 Ruthenium Compounds with N, S-donor ligands

Metal complexes of ruthenium containing nitrogen, sulfur-donor ligands are of considerable interest due to their intricate redox and electronic properties which stems from their unusual structural features [69, 70]. Sulfur donors can readily exist in several hybridized forms and when coordinated to ruthenium; can either be σ -donors or can be strong $3d_\pi$ back-bonding ligands [71]. This phenomenon can be illustrated in the following ruthenium(II) Schiff base complex, $\text{trans-[Ru(mpnap)(CO)(PPh}_3)_2]$ (H_2mpnap = 1-(2-mercaptophenylimino)methylnaphthalen-2-ol) where sigma-bond donation occurs between from the deprotonated thiol atom to the metal centre [14], see **Figure 1.13**. In the case of the mononuclear complexes, $[\text{Na}][\text{trans-Ru}^{\text{III}}\text{Cl}_4(\text{DMSO})(\text{L})]$ and its dimer, $[\text{Na}]_2[\{\text{trans-Ru}^{\text{III}}\text{Cl}_4(\text{DMSO})\}_2(\text{L})]$, the neutral DMSO coordination bonds are formed *via* pi-back donation from the metal into the vacant $3d_\pi$ -orbitals of the sulfur donors [72], see **Figure 1.14**.

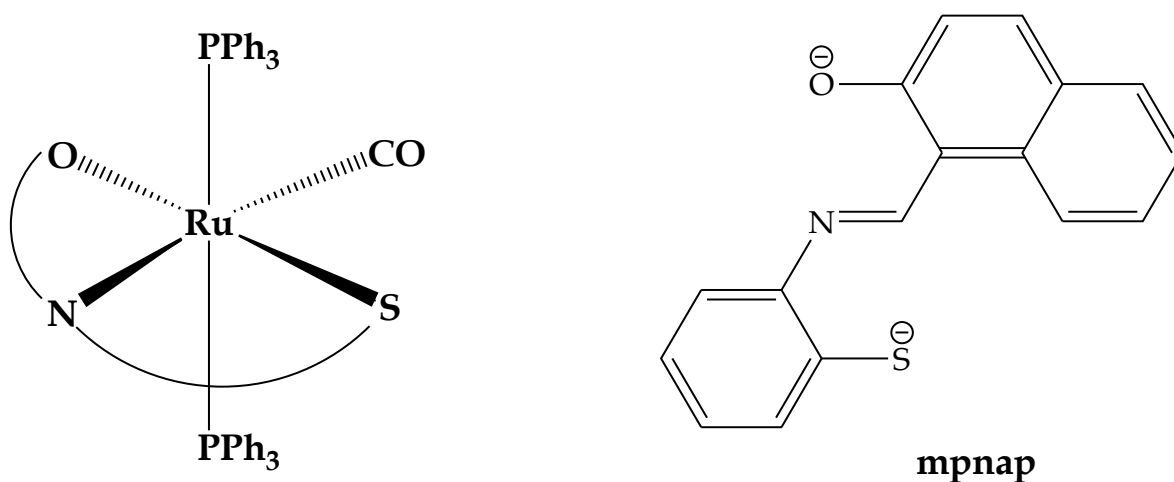


Figure 1.13: The structure of the dianionic, tridentate mpnap moiety and the skeletal structure of its complex, *trans*-[Ru(mpnap)(CO)(PPh₃)₂].

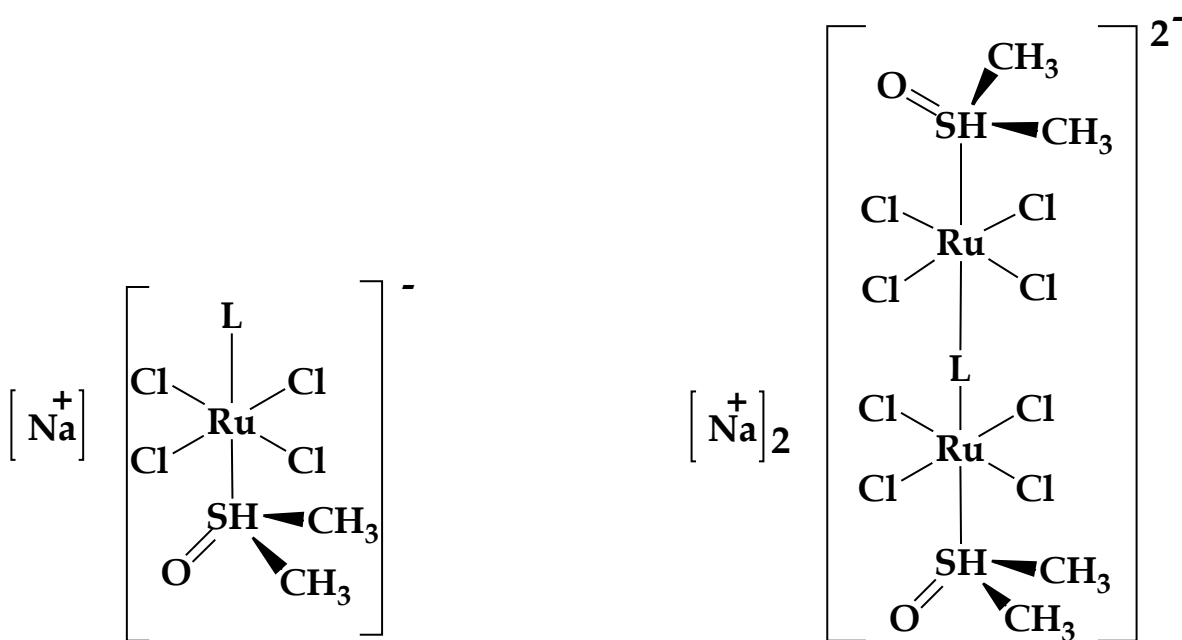


Figure 1.14: The monomeric (A) and dimeric (B) forms of [Na][*trans*-Ru^{III}Cl₄(DMSO)(L)].

1.6.3 Ruthenium Compounds with N, O-donor Ligands

Schiff bases that contain nitrogen and sulfur atoms have attracted much research interest due to their versatile electronic and steric properties [73]. Designing Schiff base ligands with hard and soft donors have proven favorable in the isolation of

numerous ruthenium(II/III) complexes [74, 75]. Some isolated complexes of this nature include the monoamine and diimine ruthenium complexes, $[\text{Ru}^{\text{III}}(\text{ahsH})(\text{PPh}_3)_2\text{Cl}]$ ($\text{H}_2\text{ahsH} = N\text{-(acetyl)-}N'\text{-(salicylidene)hydrazines}$) and $[\text{Ru}^{\text{II}}(\text{salen})(\text{PPh}_3)_2]$ containing the N_2O and N_2O_2 donor sets within the equatorial plane, respectively as well as for both complexes, being re-enforced by the *trans*- $[\text{Ru}(\text{PPh}_3)_2]$ core [76, 77].

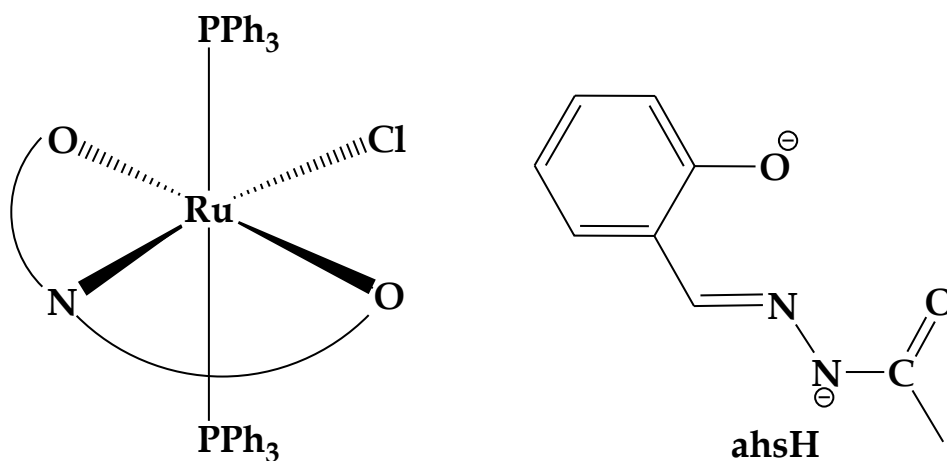


Figure 1.15: Structure of $[\text{Ru}(\text{ahsH})(\text{PPh}_3)_2\text{Cl}]$.

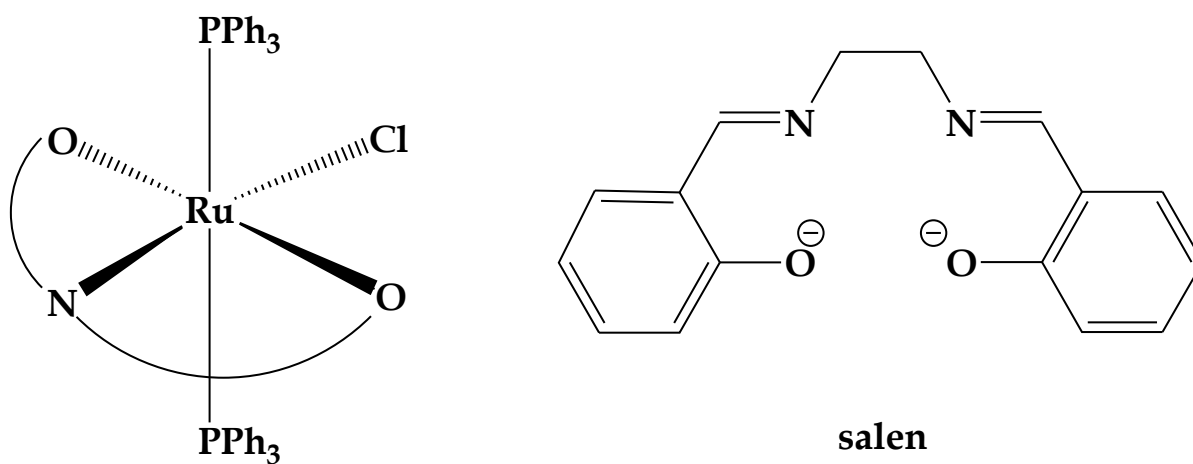


Figure 1.16: Structure of $[\text{Ru}^{\text{III}}\text{Cl}(\text{salen})(\text{PPh}_3)_2]$.

1.7 References:

1. Lide, D.R. *The CRC handbook of Chemistry and Physics*, 84th ed., Taylor and Francis, 2003.
2. Krebs, R.E. *The History and Use of Our Earth's Chemical Elements: A Reference Guide*, 2nd ed., Greenwood Publishing Group, 2006.
3. Earnshaw, A., Greenwood, N. *Chemistry of the Elements*, 2nd ed. Elsevier, 1997; Barnard, C.F.J., Bennett S.C. *Platinum Metals Rev.*, 2004, **48**, 157.
4. Griffith, W.P. *Ruthenium Oxidation Complexes: Their Uses as Homogenous Organic Catalysts - Catalysis by metal complexes*, Springer, 2010; Che, C. *Pure Appl. Chem.*, 1995, **67**, 225.
5. Bratsos, I., Jedner, S., Gianferrara, T., Alessio, E. *Chimia*, 2007, **61**, 692.
6. Arblaster, J.W. *Platinum Met. Rev.*, 2011, **55**, 251.
7. Georgios, C. Vougioukalakis, G.C., Grubbs, R.H. *Chem. Rev.*, 2010, **110**, 1746.
8. Bruneau, C., Achard, M. *Coord. Chem. Rev.*, 2012, **256**, 525.
9. Therrien, B. *Coord. Chem. Rev.*, 2009, **253**, 493.
10. Grubbs, R.H. *Handbook of Metathesis*, Wiley-VCH, 2003.
11. Allesio, E., Mestroni, G., Bergamo, A., Savan, G. *Curr. Top. Med. Chem.*, 2004, **4**, 1525.
12. Anitha, P., Chitrapriya, N., Jang, Y.J., Viswanathamurthi, P. *J. Photochem. Photobiol. B, Biol*, 2013, **129**, 17.
13. Santamaria, R., Irace, C., D'Errico, G., Montesarchio, D., Paduano, L. *J Pharm Drug Devel*, 2013, **1**, e201.
14. Tamizh, M.M., Mereiter, K., Kerchner, K., Karvembu, R. *J. Organomet. Chem.*, 2012, **700**, 194.
15. Chakravarty, J., Bhattacharya, S. *Chem. Sci.*, 1995, **107**, 361.
16. Mandal, S., Seth, D.K., Gupta, P. *Polyhedron*, 2012, **31**, 167.
17. Imrie, C., Nyamori, V.O., Gerber, T.I.A. *J. Organomet. Chem.*, 2004, **689**, 1617.
18. Branham, M.L., Singh, P., Bisetty, K., Sabela, M., Goveder, T. *Molecules*, 16, 10269.
19. Mohamed, G.G., Omar, M.M., Hindy, A.M. *Turk J Chem*, 2006, **30**, 361.

20. Mahalingam, V., Chitrapriya, N., Fronczek, F.R., Natarajan, K. *Polyhedron*, 2010, **29**, 3363.
21. Raja, G., Butcher, R.J., Jayabalakrishnan, C. *Spectrochim. Acta, Part A*, 2012, **94**, 210.
22. Grazul, M., Budzisz, E. *Coord. Chem. Rev.*, 2009, **253**, 2588.
23. Srivastava, A., Gupta, D.C. *IJAER Journal*, **1**, 2010, 222.
24. Lee, W. *Mikrochim. Acta*, 1997, **127**, 19.
25. Sathiyaraj, S., Butcher, R.J., Jayabalakrishnan, C. *J. Coord. Chem.*, 2013, **66**, 580.
26. Lee, D.N., Park, H.J., Kim, D.H., Lee, S.W., Park, S.J., Kim, B.H., Lee, W. *Bull. Korean. Chem. Soc*, 2002, **23**, 13.
27. Sukanya, D., Pabhakaran, R., Natarajan, K. *Polyhedron*, 2006, **25**, 2223.
28. Balasubramanian, K.P., Karvembu, R., Prabhakaran, R., Chinnusamy, V., Natarajan, K. *Spectrochim. Acta, Part A*, 2007, **68**, 50.
29. Spillane, C.B., Fletcher, N.C., Rountree, S.M., Van Der Berg, H., Chanduloy, S., Morgan, J.L., Keene, F.R. *J. Biol. Inorg. Chem.*, 2007, **12**, 797.
30. Maji, M., Sengupta, P., Kumar, S., Schwalbe, C.H., Ghosh, S. *J. Coord. Chem.*, 2001, **54**, 13.
31. Sahu, R., Thakur, D.S., Kashyap, P. *IJPSN Journal*, 2012, **5**, 1757.
32. McCracken, R.O., Lipkowitz, K.B. *J. Parasitol.*, 1990, **76**, 853.
33. Rudrapal, M., De, P. *IRJPA Journal*, 2013, **3**, 232.
34. Sainsbury, M. *Heterocyclic Chemistry*, 8th ed, Royal Society of Chemistry, 2001, Chapter 1.
35. Jimonet, P., Audiau, F., Barreau, M., Blanchard, J., Boireau, A., Bour, Y., Cole'no, M., Doble, A., Doerflinger, G., Do Huu, C., Donat, M., Duchesne, J.M., Ganil, P., Gue're'my, C., Honore', E., Just, B., Kerphirique, R., Gontier, S., Hubert, P., Laduron, P.M., Le Blevec, J., Meunier, M., Miquet, J., Nemecek, C., Pasquet, M., Piot, O., Pratt, J., Rataud, J., Reibaud, M., Stutzmann, J., Mignani, S. *J. Med. Chem.*, 1999, **42**, 2828.
36. Abram, U., Alberto, R.J. *J. Braz. Chem. Soc.*, 2006, **17**, 1486.
37. Karpinska, M.M., Matysiak, J., Niewiadomy, A. *Arch. Pharm Res.*, 2011, **34**, 1639.

38. Adenyini, A.A., Ajibade, P.A. *Molecules*, 2013, **18**, 10829.
39. Mounika, K., Anupama, B., Pragathi, J., Gyanakumari, C. *J. Sci. Res*, 2010, **2**, 513.
40. Zhou, Q., Yang, P. *Inorg. Chim. Acta.*, 2006, **359**, 1200.
41. Aldrich-Wright, J. *MetalloIntercalators-synthesis and techniques to probe their interactions with biomolecules*, SpringerWienNewYork, 2011, 18-21.
42. Sadler, P.J., Guo, Z. *Pure Appl. Chem.*, 1998, **70**, 863.
43. Sessler, J.L., Doctrow, S.R., McMurry, T.J., Lippard, S.J. *Medicinal Inorganic Chemistry*, American Chemical Society, 2005, 80.
44. Brabec, V., Novakova, O. *Drug Resist. Updat.*, 2006, **9**, 111.
45. Rademaker-Lakhai, J.M., van den Bongard, D., Pluim, D. *Clin. Cancer Res.*, 2004, **10**, 3717.
46. Clarke, M.J. *Coord. Chem. Rev.*, 2003, **236**, 209.
47. Allardyce, C.S., Dyson, P.J. *Platinum Metal Rev*, 2001, **45**, 62.
48. Fandzloch, M., Wojtczak, A., Sitkowski, J., Lakomska, I. *Polyhedron*, 2014, **67**, 410.
49. Zhang, C.X., Lippard, S.J. *Curr. Opin. Chem. Biol.*, 203, **7**, 481.
50. Bicek, A., Turel, I., Kanduser, M., Miklavcic, D. *Bioelectrochemistry*, 2007, 113.
51. Heffeter, P., Bock, K., Atil, B., Hoda, M.A.R., Korner, W., Bartel, C., Jungwirth, U., Keppler, B.K., Micksche, M., Berger, W., Koellensperger, G. *J. Biol. Inorg. Chem.*, 2010, **15**, 737.
52. Wang, Z., Qian, H., Yiu, S., Sun, J., Zhu, G. *J. Inorg. Biochem.*, 2014, **131**, 47.
53. Chakraborty, S., Munshi, P., Lahiri, G.K. *Polyhedron*, 1999, **18**, 1437.
54. Tiba, F., Jaganyi, D., Mambanda, A. *J. Coord. Chem.*, 2010, **63**, 2542.
55. Aikawa, M., Yoshino, Y. *Inorg. Chim. Acta.*, 1998, **282**, 38.
56. Booysen, I.N., Abimbola, A., Munro, O.Q., Xulu, B. *Polyhedron*, 2014, <http://dx.doi.org/10.1016/j.poly.2014.02.009>.
57. Levina, A., Mitra, A., Lay, P.A., *Metallomics*, 2009, **1**, 458.
58. Chatterjee, D., Mitra, A. *Platinum Met. Rev.*, 2006, **50**, 2.
59. Cotton, F.A., Wilkinson, G. *Advanced Inorganic Chemistry: A Comprehensive Text*, John Wiley & Sons, 1980, 923.

60. Hara, M., Waraska, C.C., Lean, J.T., Lewis, B.A., Mallouk, T.E. *J. Phys. Chem. A.*, 2000, **104**, 5275.
61. Choi, S., Ryu, D., DellaRocca, J.G., Wolf, M.W., Bogart, J.A. *Inorg. Chem.*, 2011, **50**, 6567.
62. Kapovsky, M., Dares, C., Dodsworth, E.S., Begum, R.A., Raco, V., Lever, A.B.P. *Inorg. Chem.*, 2013, **52**, 169.
63. Rudd, D.F., Taube, H. *Inorg. Chem.*, 1971, **10**, 1543.
64. Ljubijankic, N., Zahirovic, A., Turkusic, E., Kahrovic, E. *Croat. Chem. Acta.*, 2013, **86**, 215.
65. Perera, S.D. *OUSL Journal*, 2007, 4, 72.
66. Gaudalupe, H.J., Narayanan, J., Pandiyan, T. *J. Mol. Struct.*, 2011, **989**, 70.
67. Billings, S.B., Mock, M.T., Wiacek, K., Turner, M.B., Kassel, W.S., Takeuchi, K.J., Rhenigolf, A.L., Boyko, W.J., Bessel, C.A. *Inorg. Chim. Acta.*, 2003, **355**, 103.
68. Thompson, A.M.W.C., Batten, S.R., Jeffery, J.C., Rees, L.H., Ward, M.D. *Aust. J. Chem.*, 1997, **50**, 109.
69. De Sousa Moreira, I., de Lima, J.B., Franco, D.W. *Coord. Chem. Rev.*, 2000, **196**, 197.
70. Halbach, D.P., Hamaker, C.G. *J. Organomet. Chem.*, 2006, **691**, 3349.
71. Nagaraju, J., Pal, S. *Inorg. Chim. Acta.*, 2014, **413**, 102.
72. Ravera, M., Gabano, E., Baracco, S., Sardi, M., Osella, D. *Inorg. Chim. Acta*, 2008, **361**, 2879.
73. Venkatachalam, G., Ramesh, R. *Spectrochim. Acta, Part A.*, 2005, **61**, 2081.
74. Venkatachalam, G., Ramesh, R. *Inorg. Chim. Acta*, 2013, **394**, 171.
75. Venkatachalam, G., Ramesh, R. *Inorg. Chem. Commun.*, 2005, **8**, 1009.
76. Raveendran, R., Pal, S. *Polyhedron*, 2008, **27**, 655.
77. Sun, W., Yu, B., Kuhn, F.E. *Tetrahedron Lett.*, 2006, **47**, 1993.

Chapter 2

Experimental

2.1 Handling of Ruthenium

Ruthenium compounds are considered environmentally hazardous, carcinogenic and highly toxic. These compounds can potentially form the poisonous and volatile ruthenium tetroxide when heated in air that can seriously damage the respiratory system and eyes [1]. Therefore, several special precautions were taken into account during the handling of all ruthenium compounds including the wearing of latex gloves and a dust mask at all times as well as the use of a fume cupboard in which all the coordination reactions were performed.

2.2 Materials

2.2.1 Metal precursor

The metal precursor, *trans*-[RuCl₂(PPh₃)₂] (97% purity) was obtained from Sigma-Aldrich and no further purification was conducted on this chemical.

2.2.2 Commercially acquired chemicals

All solvents and common laboratory chemicals were of analytical grade and used without any further purification. The chemicals listed in **Table 2.1** were purchased from Sigma-Aldrich and were also used with no further purification.

Table 2.1: List of chemicals attained from Sigma-Aldrich.

Name	Purity
Salicylaldehyde	98%
Thiophene-2-carbaldehyde	98%
2-(Methylthio)benzaldehyde	90%
5,6-Diamino-1,3-dimethyluracil hydrate (H ₂ ddd)	95%
3-Formylchromone	97%
Pyridine-2-carbaldehyde	99%
2,6-Pyridinedicarboxaldehyde	97%
4-Aminoantipyrine	99%
2-Aminopyridine	99%
2-Hydroxyphenylbenzimidazole (Hobz)	95%
2-Hydroxyphenylbenzothiazole (Hobs)	97%
Piperidine	99%
Ammonium tetrafluoroborate	99%

2.3 Synthetic Procedures of Schiff Base Ligands

2.3.1 *Synthesis of 5-((thiophen-3-yl)methyleneamino)-6-amino-1,3-dimethyluracil (H₂tdp)*
H₂ddd (0.500 g; 2.94 mmol) and thiophene-2-aldehyde (0.399 cm³; 4.41 mmol) were refluxed for 3 hours in methanol (40 cm³). The resulting dark yellow solution was allowed to cool to room temperature, filtered and a bright yellow precipitate was washed with cold anhydrous toluene as well as diethyl ether. Yield = 63%; m.p. 240.7–242.0 °C. IR (ν_{max} /cm⁻¹): $\nu(\text{N-H})$ 3396, 3286, $\nu(\text{C=O})$ 1671, $\nu(\text{C=N})$ 1611, $\nu(\text{thiophene})$ 1506, 1447 and 1380. ¹H NMR (295K/*d*⁶-DMSO/ppm): 9.79 (s, 1H, *H*1), 7.58 (d, 1H, *H*4), 7.41 (d, 1H, *H*2), 7.95 (t, 1H, *H*3), 6.96 (br, s, 2H, *NH*₂), 3.42 (s, 3H, *CH*₃), 3.18 (s, 3H, *CH*₃). UV-Vis (DMF, λ_{max} (ϵ , M⁻¹ cm⁻¹)): 288 nm (1437), 292 nm (2421), sh, 390 nm (1897).

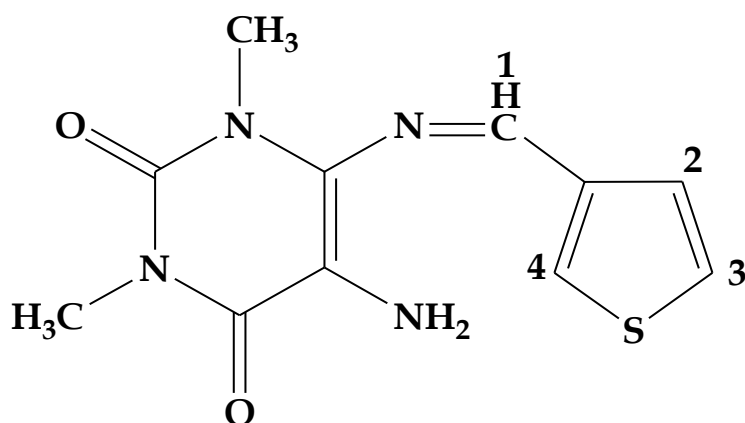


Figure 2.1: Numbering scheme for H_2tdp .

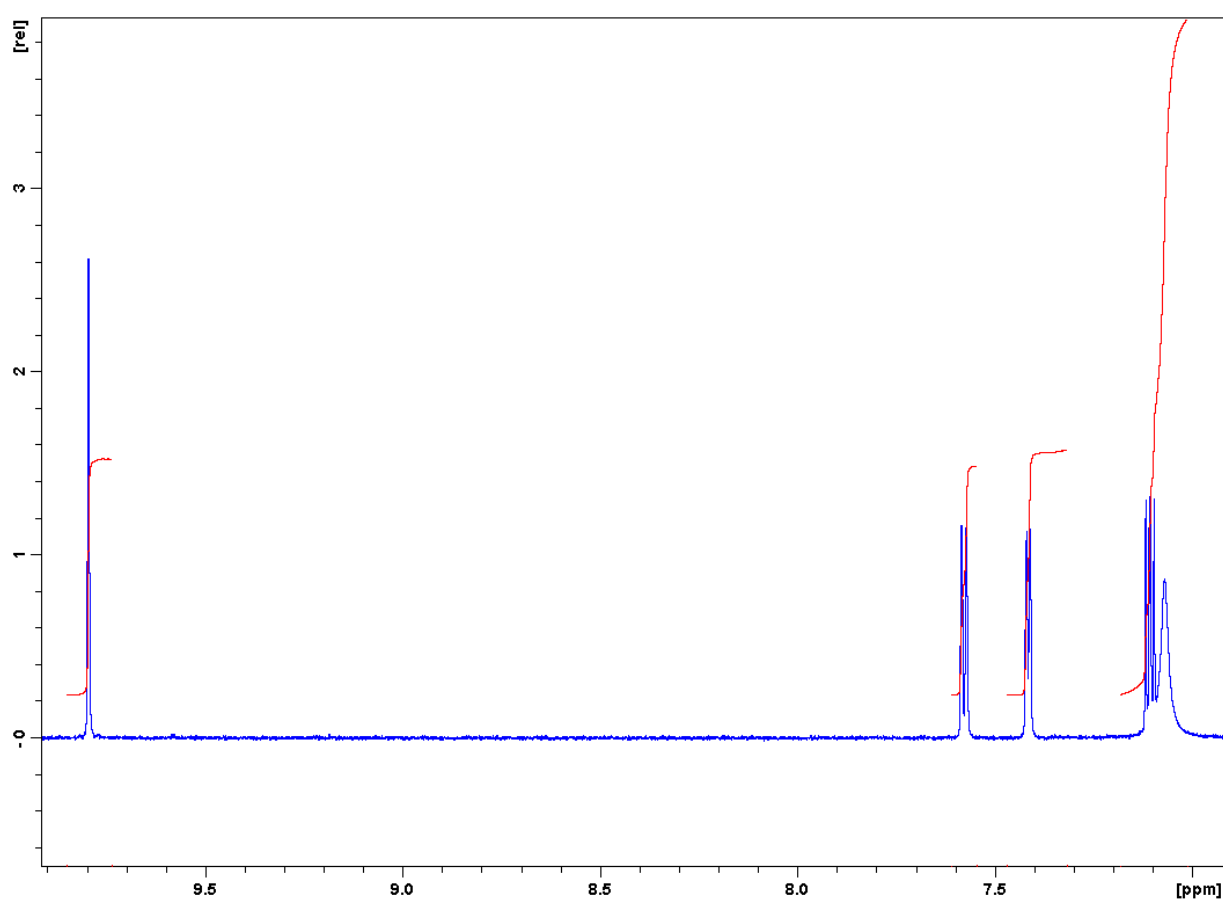


Figure 2.2: 1H NMR of the H_2tdp ligand in the range of 9.90 – 5.90 ppm.

2.3.2 Syntheses of 5-(2-(methylthio)benzylideneamino)-6-amino-1,3-dimethyluracil

(H_2sdp) and 5-(2-hydroxybenzylideneamino)-6-amino-1,3-dimethyluracil (H_3hdp)

The Schiff bases, H_3hdp and H_2sdp were synthesized as previously reported from the condensation reactions of H_2ddd with 2-methylthiobenzaldehyde and salicylaldehyde, respectively [2, 3].

2.3.3 Synthesis of 2,6-Bis-((6-amino-1,3-dimethyluracilimino)methylene)pyridine (H_{4ucp})

A reaction mixture of 5,6-diamino-1,3-dimethyluracil (1.25 g; 7.40 mmol) and pyridine-2,6-dicarbaldehyde (0.503 g; 3.72 mmol) was heated at reflux in methanol (40 cm³) in the presence of a catalyst, piperidine (3 drops). After 3 hours, the bright orange solution was allowed to cool to room temperature and the yellow precipitate which formed was collected (*via* filtration), washed with cold methanol as well as petroleum ether. Yield = 95%, m.p. = 234–237 °C. IR ($\nu_{\max}/\text{cm}^{-1}$): $\nu(\text{C=O})$ 1678 (s), $\nu(\text{C=N})$ 1596 (s); ¹H NMR (295K/ppm, see Fig. S2): 9.70 (s, 2H, H_4 , H_8), 8.33 (d, 2H, H_5 , H_7), 7.78 (t, 1H, H_6), 7.46 (br, s, 4H, $N(1)H_2$, $N(11)H_2$), 3.41 (s, 6H, $C3H_3$, $C9H_3$), 3.19 (s, 6H, $C2H_3$, $C10H_3$). UV-Vis (DMF, λ_{\max} (ϵ , M⁻¹cm⁻¹)): 233 nm (7900), 278 nm (sh, 4900), 285 nm (5000), 368 nm (8800), 451 nm (600), 588 nm (600).

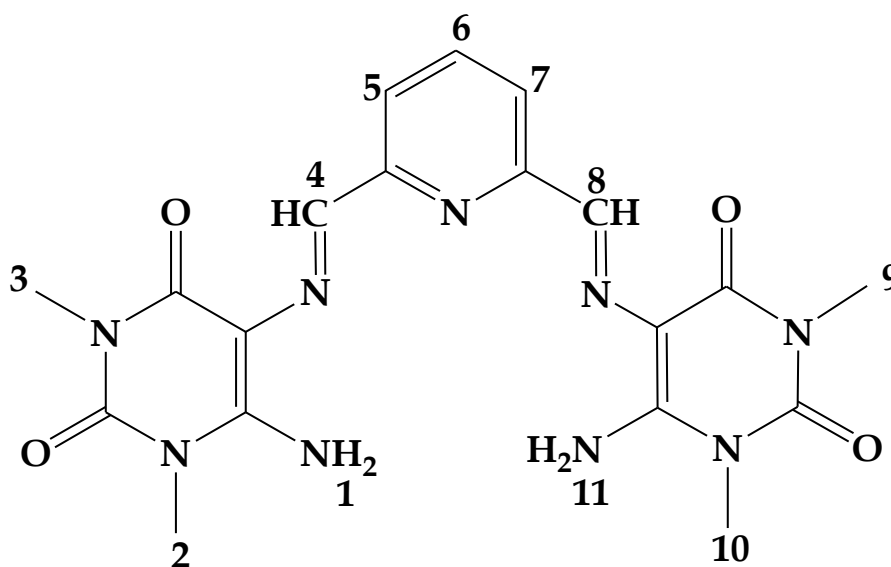


Figure 2.3: Numbering scheme for H_{4ucp} .

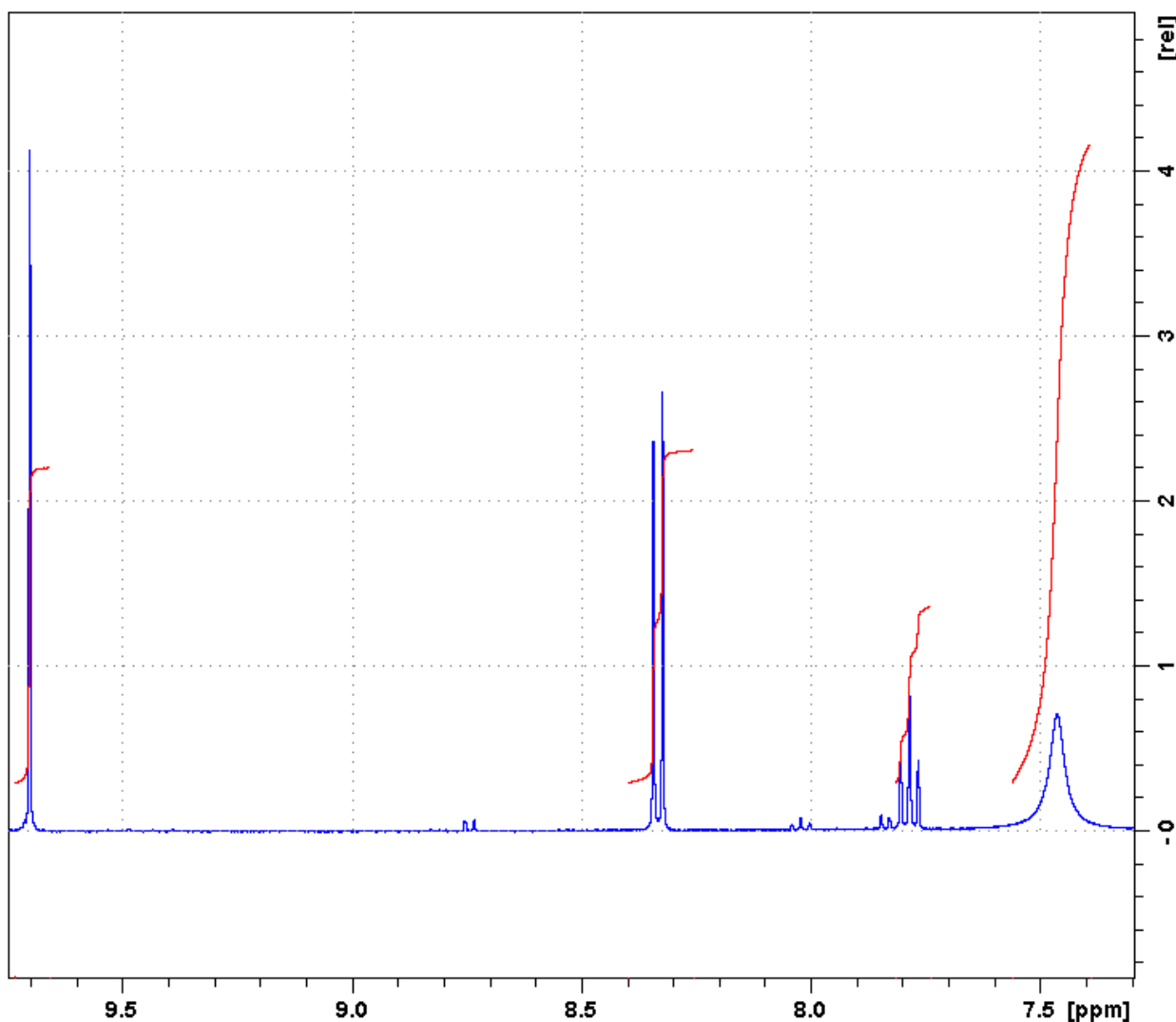


Figure 2.4: ^1H NMR spectrum of H_4ucp in the range of 7.30 - 9.75 ppm.

2.3.4 Synthesis of 4-((pyridine-2ylimino)methylene)-chromone (*pch*)

The condensation reaction of 3-formylchromone (0.925 g; 5.31 mmol) and pyridin-2-amine (0.510 g; 5.42 mmol) was conducted in methanol (30 cm^3) under reflux (for 3 hours) in the presence of three drops of piperidine. The orange solution was allowed to cool to room temperature and a mustard-coloured precipitate was filtered and washed with cold methanol as well as petroleum ether. Yield = 95%, m.p. = 115 - 118 °C. IR ($\nu_{\text{max}}/\text{cm}^{-1}$): $\nu(\text{C}=\text{O})$ 1647 (s), $\nu(\text{C}=\text{N})$ 1611, 1603, 1590 (s), $\nu(\text{C}-\text{O}-\text{C})$ 1557; ^1H NMR (295K/ppm): 11.77 (d, 1H, H_1), 8.40 - 8.34 (m, 4H, H_4 , H_5 , H_6 , H_{10}), 7.89 - 7.70 (m, 2H, H_2 , H_3), 7.59 - 7.51 (m, 2H, H_8 , H_9), 7.36 (d, 1H, H_7). UV-Vis (DMF, λ_{max} (ϵ , $\text{M}^{-1}\text{cm}^{-1}$)): 244 nm (3222); 267 nm (1997); 384 nm (7431).

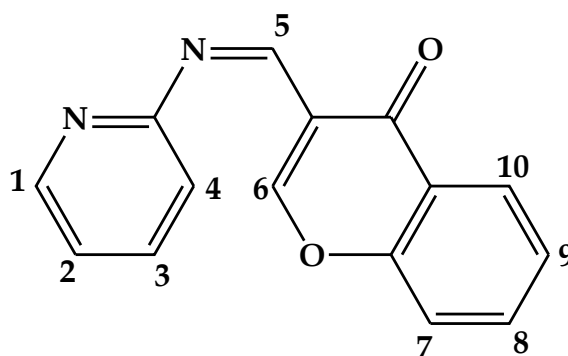


Figure 2.5: Numbering scheme for *pch*.

2.3.5 Synthesis of 2,6-bis-((antipyrine-imino)methylene)pyridine (*bpap*)

The synthetic procedure of the diimine ligand, 2,6-bis-((antipyrine-imino)methylene)pyridine (*bpap*) was adopted from a literature method [4].

2.4 Instrumentation

The infrared spectra were recorded on a Perkin-Elmer Spectrum 100 in the 4000– 650 cm^{-1} range. The ^1H NMR spectra were obtained using Bruker Avance 400 MHz and 500 MHz spectrometers, respectively. The X-band EPR spectra were obtained from Bruker EMX Premium and Ultra X spectrometers. UV/visible spectra were recorded using a Perkin Elmer Lambda 25. The extinction coefficients (ϵ) are given in $\text{dm}^3 \text{mol}^{-1} \text{cm}^{-1}$. Melting points were determined using a Stuart SMP3 melting point apparatus. The conductivity measurements were determined at 295 K on a Radiometer R21M127 CDM 230 conductivity and pH meter. A solution of 0.745 g KCl in 1 L of ultrapure water was used as the standard solution.

Cyclic voltammetry measurements were done using an Autolab potentiostat equipped with a three electrode system: A glassy carbon working electrode (GCWE), a pseudo $\text{Ag}|\text{AgCl}$ reference electrode and an auxiliary Pt counter electrode. The Autolab Nova 1.7 software was utilized for the operation of the potentiostat and data analysis. The ruthenium metal complexes were made up in 2 mM solutions in DCM along with tetrabutylammonium hexafluorophosphate (0.1 M) as a supporting electrolyte. Between each measurement, the GCWE surface was polished with slurry

of ultrapure water and alumina on a Buehler felt pad followed by rinsing with excess ultrapure water and ultra-sonication in absolute ethanol. Ultrapure water was produced from an ElgaPurelab Ultra system.

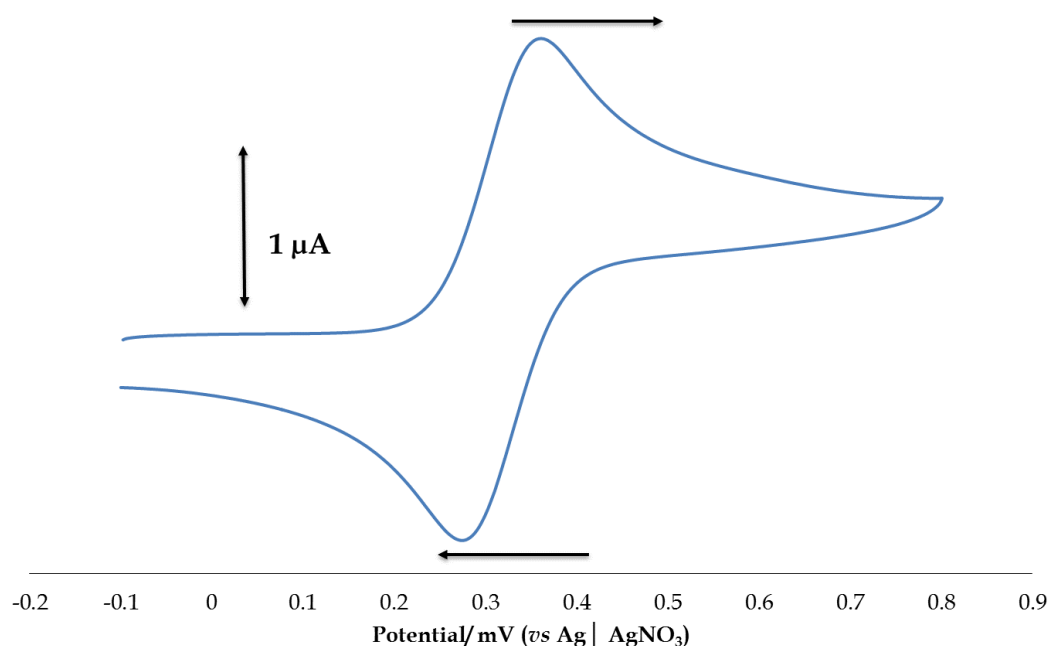


Figure 2.7: Cyclic Voltammogram for the Ferrocene Standard at 100 mV/s with the arrows showing scan direction).

The X-ray data for the metal complexes were recorded on a Bruker Apex Duo and an Oxford Diffraction Xcalibur 2 CCD 4-circle diffractometer equipped with an Oxford Instruments Cryojet operating at 120(2) K and 100(2) K and an Incoatec microsource operating at 30 W power. Data was collected with MoK $_{\alpha}$ ($\lambda = 0.71073 \text{ \AA}$) radiation at a crystal-to-detector distance of 50 mm. The data collection on the Oxford diffractometer was performed using omega scans at $\theta = 29.389^{\circ}$ with exposures taken at 2.00 kW X-ray power and 0.75° frame widths using CrysAlis CCD [5]. The data were reduced with CrysAlis RED Version 170 [5] using outlier rejection, scan speed scaling, as well as standard Lorentz and polarization correction factors. A semi-empirical multi-scan absorption correction [6] was applied to the data. The following conditions were used for the Bruker data collection: omega and phi scans with exposures taken at 30 W X-

ray power and 0.50° frame widths using APEX2 [7]. The data were reduced with the programme SAINT [8] using outlier rejection, scan speed scaling, as well as standard Lorentz and polarisation correction factors. A SADABS semi-empirical multi-scan absorption correction was applied to the data [6]. Direct methods, SHELXS-97 [9] and WinGX [10] were used to solve all structures.

Computational calculations were conducted with Gaussian 09W software [11]. The geometry optimizations of the complexes were accomplished at the Density Functional Theory level using the B3LYP correlation functional, the LANL2DZ and the 6-311G⁺⁺ (*d, p*) basis sets [11-15].

2.5 References:

1. Hemmatzadeh, R., Mohammadi, A. *J. Theor. Appl. Phys.*, 2013, **7**, 57.
2. Booysen, I.N., Ismail, M., Gerber, T.I.A., Akerman, M., van Brecht, B. *S. Afr. J. Chem.*, 2012, **65**, 174.
3. Booysen, I., Muhammed, I., Soares, A., Gerber, T., Hosten, E., Betz, R. *Acta Cryst.*, 2011, **E67**, 1592.
4. Potgieter, K.C. *PhD Thesis*, Nelson Mandela Metropolitan University, 2012.
5. Oxford Diffraction. *CrysAlis CCD and CrysAlis RED*, Oxford Diffraction, Yarnton (2008).
6. Blessing, R.H., *Acta Cryst.*, 1995, **A51**, 33.
7. Johnson, N.P., Lock, C.J.L., Wilkinson, G. *Inorg. Synth.*, 1967, **145**, 9.
8. Bruker APEX2, SAINT and SADABS. Bruker AXS Inc. (2010) Madison, Wisconsin, USA.
9. Sheldrick, G.M. *Acta. Cryst.*, 2008, **A64**, 112.
10. Farrugia, L.J. *J. Appl. Cryst.*, 2012, **45**, 849.
11. Frisch, M.J., Trucks, G.W., Schlegel, H.B., Scuseria, G.E., Robb, M.A., Cheeseman, J.R., Scalmani, G., Barone, V., Mennucci, B., Petersson, G.A., Nakatsuji, H., Caricato, M., Li, X. Hratchian, H.P., Izmaylov, A.F., Bloino, J., Zheng, G., Sonnenberg, J.L., Hada, M., Ehara, M., Toyota, K., Fukuda, R.,

Hasegawa, J., Ishida, M., Nakajima, T., Honda, Y., Kitao, O., Nakai, H., Vreven, T., Montgomery, Jr., J.A., Peralta, J.E., Ogliaro, F., Bearpark, M., Heyd, J.J., Brothers, E., Kudin, K.N., Staroverov, V.N., Kobayashi, R., Normand, J., Raghavachari, K., Rendell, A., Burant, J.C., Iyengar, S.S., Tomasi, J., Cossi, M., Rega, N., Millam, J.M., Klene, M., Knox, J.E., Cross, J.B., Bakken, V., Adamo, C., Jaramillo, J., Gomperts, R., Stratmann, R.E., Yazyev, O., Austin, A.J., Cammi, R., Pomelli, C., Ochterski, J.W., Martin, R.L., Morokuma, K., Zakrzewski, V.G., Voth, G.A., Salvador, P., Dannenberg, J.J., Dapprich, S., Daniels, A.D., Farkas, Ö., Foresman, J.B., Ortiz, J.V., Cioslowski, J., Fox, D.J. *Gaussian 09 (Revision A.01)*, 2009, Gaussian Inc., Wallingford CT.

12. Becke, A.D. *J. Chem. Phys.*, 1993, **98**, 5648-52.
13. Dunning, T.H., Jr., Hay, P.J. *Modern Theoretical Chemistry*, H.F. Schaefer, ed., Vol. 3, Plenum Press, New York, 2003, 1-28.
14. Mei, W., Liu, Y. *Trans. Met. Chem.*, 2005, **30**, 82.
15. Ogweno, A.O., Ojwach, S.O., Akerman, M.P. *Dalton Trans.*, 2014, **43**, 1228.

Chapter 3

Ruthenium(II) and (IV) Complexes with potentially Tridentate Schiff Base Chelates containing the Uracil Moiety

3.1 Introduction

Pyrimidines are known to have a wide variety of biological activities and some are endowed with antitumour, antiviral and antifungal properties [1]. Of particular interest to us is 5,6-diamino-1,3-dimethyl uracil (H_2ddd), see **Figure 3.1**, which is an analogue of the established chemotherapeutic drug, uracil mustard [2]. It has previously been shown that Schiff base derivatives of H_2ddd have diverse coordination modes toward other transition metals, such as ruthenium, in both high and low oxidation states [3, 4].

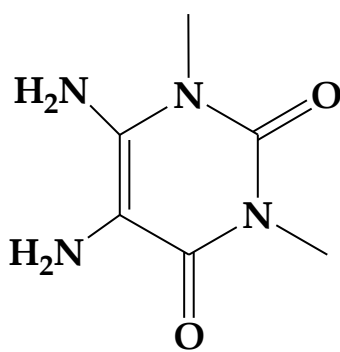


Figure 3.1: Structure of 5,6-diamino-1,3-dimethyl uracil (H_2ddd).

Ruthenium compounds with derivatives of uracil and other nucleotide bases are known, *e.g.* the ruthenium(III) compounds, $[RuCl_4(DMSO)[H-L^A]]$ $\{L^A = N^6$ -pentyladenine, N^6 -hexyladenine or N^6,N^6 -dibutyladenine $\}$ [5, 6, 7]. The study of transition metals with nucleotide bases are important as it aids in the understanding of the mechanisms of these metals towards the metabolism of nucleic acids. The coordination of ruthenium with various nucleotides have revealed that the metal

interacts with the N(7) of the purines, the N(3) of the pyrimidines and could possibly metabolize DNA in a similar manner to that of platinum metal, which is used in the successful drug Cisplatin [8].

In this chapter, the coordination behaviour of various Schiff bases synthesized from a derivative of the biologically relevant moiety, uracil [*viz.* 5,6-diamino-1,3-dimethyluracil (H_2ddd)], towards ruthenium(II) were explored (see **Figure 3.2**). The ruthenium complexes *trans*-[Ru^{II}Cl(PPh₃)₂(Htdp)] (**1**), *trans*-[Ru^{II}Cl(PPh₃)₂(Hsdp)] (**2**) and [Ru^{II}Cl(PPh₃)(H₃ucp)] (**3**) were isolated from reactions with the Schiff bases 5-((thiophen-3-yl)methyleneamino)-6-amino-1,3-dimethyluracil (H_2tdp), 5-(2-(methylthio)benzylideneamino)-6-amino-1,3-dimethyluracil (H_2sdp) and 2,6-bis-((6-amino-1,3-dimethyluracilimino)methylene)pyridine (H_4ucp), respectively. Schiff base hydrolysis occurs upon reacting 5-(2-hydroxybenzylideneamino)-6-amino-1,3-dimethyluracil (H_3hdp) which led to a paramagnetic ruthenium(IV) complex, *trans-P, cis-Cl*-[Ru^{IV}Cl₂(PPh₃)₂(ddd)] (**4**).

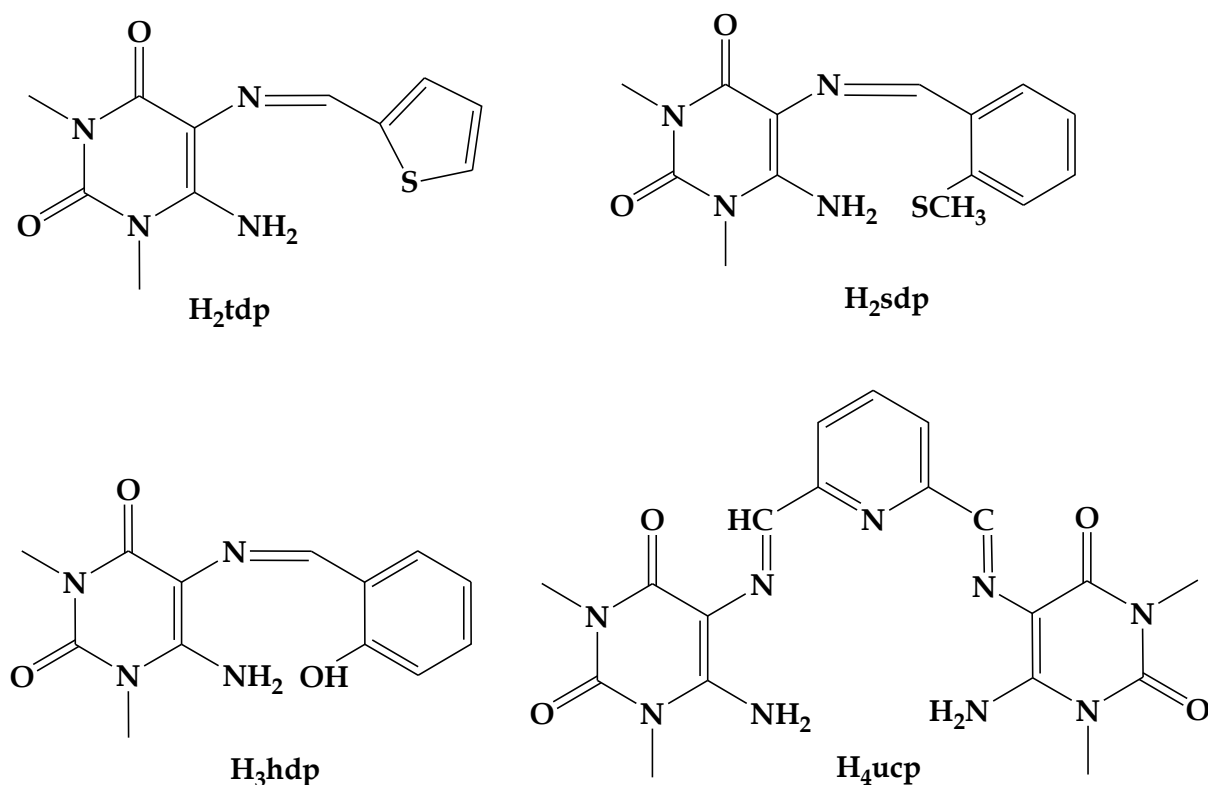


Figure 3.2: Structures and abbreviations of the Schiff bases containing the uracil moiety.

3.2 Experimental

3.2.1 Synthesis of *trans*-[RuCl(PPh₃)₂(Htdp)] (1)

H₂tdp (0.0276 g; 0.104 mmol) and *trans*-[RuCl₂(PPh₃)₃] (0.100 g; 0.104 mmol) were refluxed for 3 hours in methanol (20 cm³). While the brick-red solution was allowed to cool to room temperature, red crystals grew in the mother liquor, and were filtered and washed with anhydrous diethyl ether. These crystals were dissolved in dichloromethane and layered with hexane. The slow diffusion of hexane into the DCM solution afforded cubic-shaped crystals which were suitable for X-ray analysis. Yield = 52% based on Ru; m.p. 240.7–242.4 °C. Molar conductivity (DCM, 10⁻³ M) = 3.003 ohm⁻¹ cm² mol⁻¹. IR (ν_{\max} cm⁻¹): ν (N-H) br, 3182, ν (C=O) 1711, ν (C=N) 1665, ν (C=C) 1576, ν (thiophene) 1456, 1436 and 1368, ν (Ru-[PPh₃)₂) 746 and 696. ¹H NMR (295 K/ *d*³-CD₃CN/ ppm): 12.72 (s, 1H, NH), 7.71–7.62 (m, 4H, H1, H2, H3, H5), 7.51–7.29 (m, 30H, 2x PPh₃), 3.03 (s, 3H, CH₃), 2.78 (s, 3H, CH₃). ³¹P NMR (295 K/ *d*³-CD₃CN ppm): 15.28. UV-Vis (DCM, λ_{\max} (ϵ , M⁻¹ cm⁻¹)): 284 nm (32864), 406 nm (2265), 507 nm (9385).

3.2.2 Synthesis of *trans*-[RuCl(PPh₃)₂(Hsdp)] (2)

Equimolar amounts of H₂sdp (0.0318 g; 0.104 mmol) and *trans*-[RuCl₂(PPh₃)₃] (0.100 g; 0.104 mmol) were refluxed for 3 hours in methanol (20 cm³). The resultant cherry-red solution was allowed to cool to room temperature, and the red crystals were filtered by gravity. These crystals were recrystallized *via* slow diffusion in a chloroform and hexane (1:1) v:v solution. Yield = 61% based on Ru; m.p. 208.4–210.2 °C. Molar conductivity (DCM, 10⁻³ M) = 10.31 ohm⁻¹ cm² mol⁻¹. IR (ν_{\max} cm⁻¹): ν (N-H) br, 3398, ν (S-CH₃) 3066 ν (C=O) sh, 1705, ν (C=N) 1671, ν (C=C) 1577, ν (Ru-[PPh₃)₂) 743 and 695. ¹H NMR (295 K/ *d*³-CD₃CN/ ppm): 12.67 (s, 1H, NH), 8.01 (br, s, 1H, H1), 7.75–7.52 (m, 4H, H2, H3, H4, H5), 7.51–7.16 (m, 30H, 2x PPh₃), 6.90 (br, s, 3H, SCH₃), 3.04 (s, 3H, CH₃), 2.77 (s, 3H, CH₃). ³¹P NMR (295 K/ *d*³-CD₃CN/ ppm): 24.61. UV-Vis (DCM, (λ_{\max} ϵ , M⁻¹ cm⁻¹)): 283 nm (7649), 393 nm (1066), 509 nm (1520).

3.2.3 Synthesis of $[RuCl(PPh_3)(H_3ucp)]$ (3)

A mixture of H_4ucp (0.0458 g; 0.104 mmol) and *trans*- $[RuCl_2(PPh_3)_3]$ (0.100 g; 0.104 mmol) in methanol (20 cm³) was heated under reflux for 3 hours. A maroon precipitate was filtered by gravity, dissolved in dichloromethane and the resultant solution was layered with hexane. After several days of slow diffusion red cubic crystals, which were ideal for X-ray analysis, were attained. Yield = 73% based on Ru; m.p. 271-274 °C. Molar conductivity (DMF, 10⁻³ M): 11.17 ohm⁻¹ cm² mol⁻¹. IR (ν_{max}/cm^{-1}): $\nu(N-H)$ 3320, 3161, $\nu(C=O)$ 1686 (s), $\nu(C=N)$ 1618 (s), $\nu(Ru-PPh_3)$ 696 (m); ¹H NMR (295K/ *d*⁶-CD₆SO/ ppm): 8.59 (s, 1H, *H*7), 8.31 (s, 1H, *H*13), 7.85 (br, s, 2H, *N*3*H*₂), 7.46 – 7.21 (m, 15H, *PPh*₃), 7.17 (d, 1H, *H*9), 7.03 (d, 1H, *H*11), 6.83 (t, 1H, *H*10), 5.77 (s, 1H, *N*7*H*) 3.55 (s, 3H, *C*3*H*₃), 3.03 (s, 6H, *C*1*H*₃, *C*16*H*₃), 2.79 (s, 3H, *C*18*H*₃); ³¹P NMR (295K/ *d*⁶-CD₆SO/ppm): 36.89. UV-Vis (DMF, λ_{max} (ϵ , M⁻¹cm⁻¹)): 267 nm (sh, 20531); 387 nm (7136); 419 nm (sh, 6777); 474 (sh, 4769); 556 nm (sh, 3789).

3.2.4 Synthesis of *cis*-Cl, *trans*-P- $[RuCl_2(PPh_3)_2(ddd)]$ (4)

A 1:1 molar reaction of H_3hdp (0.029 g; 0.104 mmol) and *trans*- $[RuCl_2(PPh_3)_3]$ (0.100 g; 0.104 mmol) were refluxed for 3 hours in methanol (20 cm³). The dark maroon solution was allowed to cool to room temperature; dark red crystals were filtered and washed with anhydrous diethyl ether. These crystals were dissolved in dichloromethane and layered with hexane and the resultant solution was allowed to stand for several days. From slow diffusion of hexane into the DCM solution, XRD quality red crystalline parallelograms were afforded. Yield = 62% based on Ru; m.p. 207.9–209.0 °C. Conductivity (DCM, 10⁻³ M) = 9.433 ohm⁻¹ cm² mol⁻¹. IR (ν_{max} cm⁻¹): $\nu(N-H)$ 3052, 3148, $\nu(C=O)$ 1712, $\nu(C=C)$ 1579, $\nu(Ru-[PPh_3]_2)$ 743 and 697. UV-Vis (DCM, (λ_{max} (ϵ , M⁻¹ cm⁻¹)): 281 nm (2800), 336 nm (776), 354 nm (619), 372 nm (549), 406 nm (332), 515 nm (690).

3.3 X-Ray Crystallography

The X-ray diffraction data for **1** was recorded on an Oxford Diffraction Xcalibur 2 CCD 4-circle diffractometer equipped with an Oxford Instruments Cryojet operating at 120(2) K. The X-ray data for **3** and **4** were collected on a Bruker Apex Duo equipped with an Oxford Instruments Cryojet and an Incoatec microsource operating at 30 W power which were operated at 100(2) K. The data was reduced with CrysAlis RED Version 170 [9] and SAINT [10] and the structures were solved using SHELXS-97 [11] as well as WinGX [12]. All non-hydrogen atoms were located in the difference density map and refined anisotropically with SHELXL-97 [11]. All hydrogens of the ruthenium complexes **1** and **3** were included as idealized contributors in the least-squares process. Their positions were calculated using a standard riding model with C-H_{aromatic} distances of 0.93 Å and $U_{\text{iso}} = 1.2 U_{\text{eq}}$ and the solvent C-H bonds were located in the difference density map and refined isotropically. For **4**, OLEX 2 was utilized where the hydrogens were treated by a mixture of independent and constrained refinement [13]. The crystal structure refinement data are given in **Table 3.2** while the selected bond lengths and angles are shown in **Tables 3.3** and **3.4**.

3.4 Computational Details

Computational calculations were conducted using the Gaussian 09W software [14]. Geometry optimization of the ruthenium complex **3** was achieved through DFT calculations using the B3LYP functional, with an accompanying hybrid basis set *viz.* the 6-311G⁺⁺ (*d, p*) basis set was applied to all the C, H, N, O, Cl and P atoms and the LANL2DZ basis set applied to the metal centres [15]. Prior to the calculation, the solvent molecule of recrystallization was removed from the crystal structure and the resultant structure was used as the starting conformer. Good agreement was found between the optimized and geometrical parameters (refer to **Table 3.4**) with the minor deviations due to the fact that gas phase optimized structures does not account for non-classical hydrogen bonding interactions or any short distance contacts. Using the

optimized structure of the metal complexes, frequency calculations confirmed that the structure is at global minima on the potential energy surfaces [16].

3.5 Results and Discussion

3.5.1 Synthesis and Spectral Characterization

Equimolar reactions between *trans*-[Ru^{II}Cl₂(PPh₃)₂] with H₂tdp, H₂sdp, H₄ucp and H₃hdp led to variable valence ruthenium(II/IV) complexes, *trans*-[Ru^{II}Cl(PPh₃)₂(Htdp)] (**1**), *trans*-[Ru^{II}Cl(PPh₃)₂(Hsdp)] (**2**), [RuCl(PPh₃)(H₃ucp)] (**3**) and *trans*-*P, cis*-Cl-[Ru^{IV}Cl₂(PPh₃)₂(ddd)] (**4**), in moderate yields, respectively. In **1** and **2**, the Schiff base chelators (*i.e.* Htdp for **1** and Hsdp for **2**) coordinate as monoanionic tridentate chelators whereas in **3**, the H₃ucp ligand coordinates as a monoanionic tetradentate chelator. In the case of **4** the initial Schiff base (H₃hdp) hydrolyzed to afford the ddd chelator which is a bidentate dianionic moiety. In the preparation of **4**, no precaution was taken to ensure that the reaction was performed with a dry solvent and in an inert atmosphere which led to the hydrolysis of H₃dhdp to form ddd. The resulting ddd ligand induced oxidation of the metal centre upon coordination.

For **1** and **2**, the equatorial plane is occupied by the NNS donors of the Htdp and Hsdp ligands respectively; leaving one remaining position for the chloride (see **Figure 3.3**). For **4**, the ddd moiety affords a five-membered chelate ring through its NN-donor set *trans* to the *cis* chlorides (see **Figure 3.3**). The bulky PPh₃ ligands are *trans*-axial thereby minimizing steric repulsion. This orientation is typical for ruthenium Schiff base complexes containing the *trans*-[Ru(PPh₃)₂] core, *e.g.* *trans*-[Ru(Rcb)CO(Cl)(PPh₃)₂] {HRcb = *N*-[(dialkyl/aryl)carbamothioyl]benzamide} [17]. In an attempt to isolate octahedral saturated ruthenium complexes (*i.e.* “3 + 3” coordination modes), by utilizing higher molar ratios of the respective ligands with respect to the metal precursor, the same metal complexes (*i.e.* **1**, **2** and **4**) were isolated. Recently, the “3 + 3” ruthenium(III) compounds, [Ru(Ln)₂]ClO₄{(HLn = 4-R-2-((2-(pyridin-2-yl)hydrazono)methyl)phenol, R = H, Cl, Br, Me, and OMe)}, have been reported [18,

19]. In contrast, for **3**, the tetradentate H₃ucp ligand displaces all the equatorial co-ligands of the metal precursor by coordinating through the bridging nitrogen pyridyl nitrogen, the imino nitrogens and the singly deprotonated amido nitrogen.

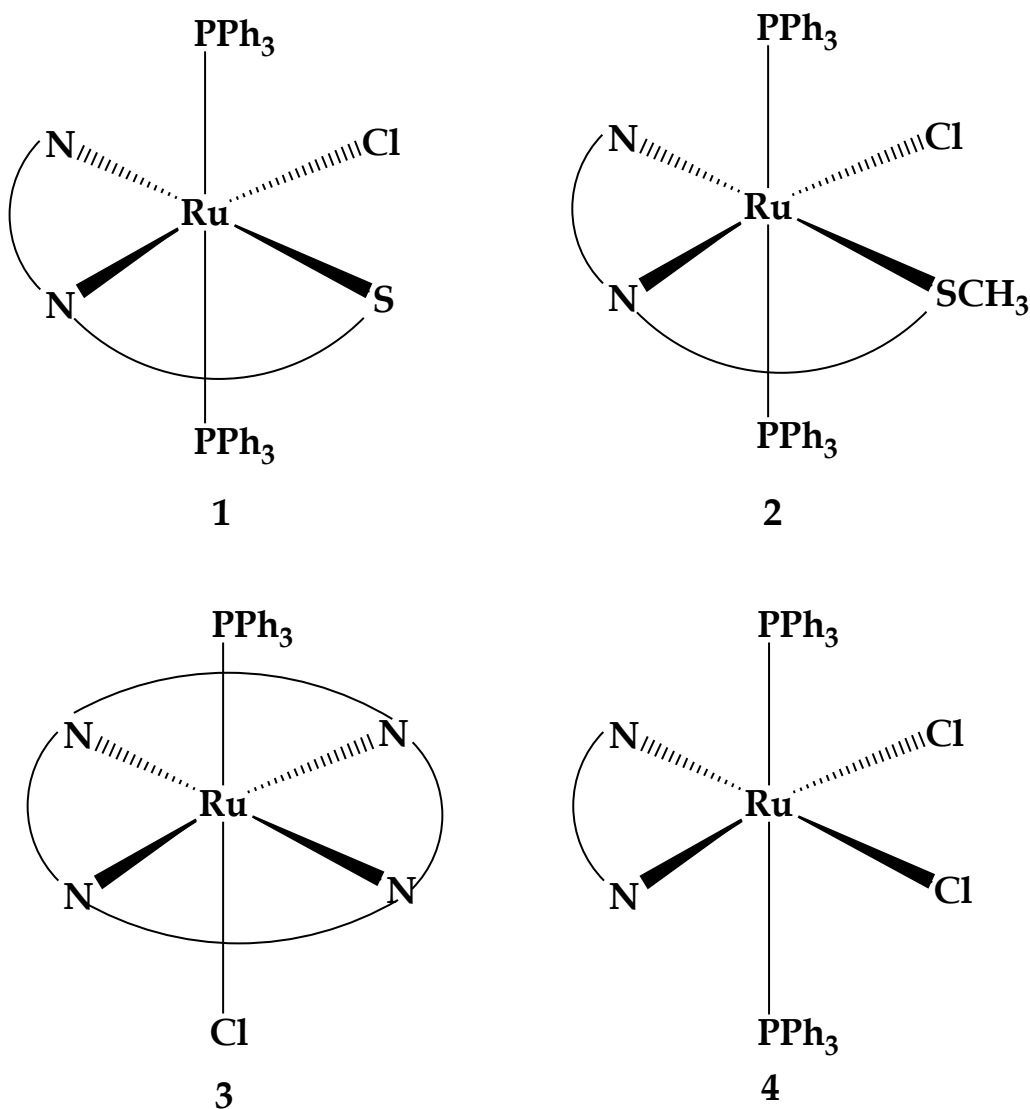


Figure 3.3: Coordination modes of the Schiff base chelates.

The Schiff bases were only soluble in DMF and DMSO, but complexes **1**, **2** and **4** exhibit good solubility in most polar solvents and are non-electrolytes in DCM. Complex **3** dissolves readily in chlorinated solvents but exhibit partial solubility in other polar solvents such as methanol, ethanol and acetonitrile and displays a high

molar conductivity value typical of a **1:1** complex salt [20]. NMR spectroscopy for the ligands (in d^6 -DMSO) and complexes (d^3 -CD₃CN) was done in different deuterated solvents, since no interpretable NMR spectra could be obtained in deuterated DMSO for **1** and **2**. Diamagnetism for **1**, **2** and **3** can be clearly seen from their respective well-resolved signals, whereas the paramagnetic **4** showed broadened signals with low intensity.

The ¹H NMR spectra for the diamagnetic complexes were dominated by multiplets (7.51–7.29 ppm for **1**, 7.51–7.16 ppm for **2** and 7.46–7.21 ppm for **3**) due to the triphenylphosphine co-ligands which are upfield relative to the multiplets of the aromatic signals for the Schiff base chelators (see **Figures 3.4** and **3.5**). Confirmation of coordination is clearly observed by the disappearance of the broad uracil-amino group singlets (6.96 ppm for H₂tdp, 3.19 ppm for H₂sdp and 7.46 ppm for H₄ucp) and the appearance of sharp singlets (12.72 ppm for **1** and 12.67 ppm for **2**) downfield due to the deprotonated form of the uracil-amino group as well as the emergence of two singlets (in **3**) which is assigned to the amino (at 7.85 ppm) and amido (at 5.77 ppm) protons. Further evidence arises from the imino singlets which are at lower frequencies (for **1** the signal is part of a 7.71–7.62 multiplet and for **2** at 8.01 ppm), in comparison to the free Schiff bases (for H₂tdp at 9.79 ppm and for H₂sdp at 10.08 ppm). The splitting of the imino protons signal for the H₃ucp chelator is a reflection of the asymmetry within the coordination sphere of **3**. Similarly, the up-field shifts of the aromatic signals of **3** relative to those of the free-ligand affirm coordination of the H₃ucp tetradentate chelator. ³¹P NMR spectroscopy confirmed the presence of the phosphorous atoms in **3** and magnetic equivalence was observed for the *trans*-axial triphenylphosphine co-ligands from the ³¹P NMR spectra of **1** and **2** since only a single peak was found for both complexes.

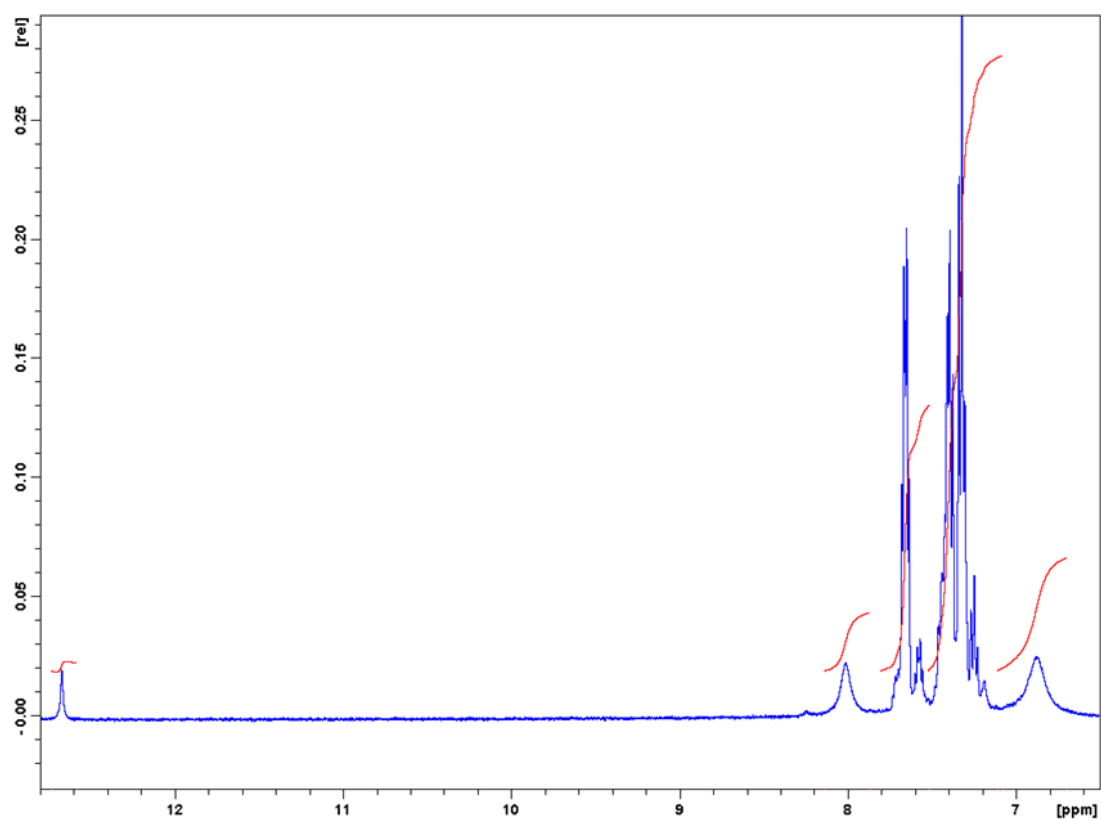


Figure 3.4: ^1H NMR spectrum of complex 2, in the range of 13.0 – 6.0 ppm.

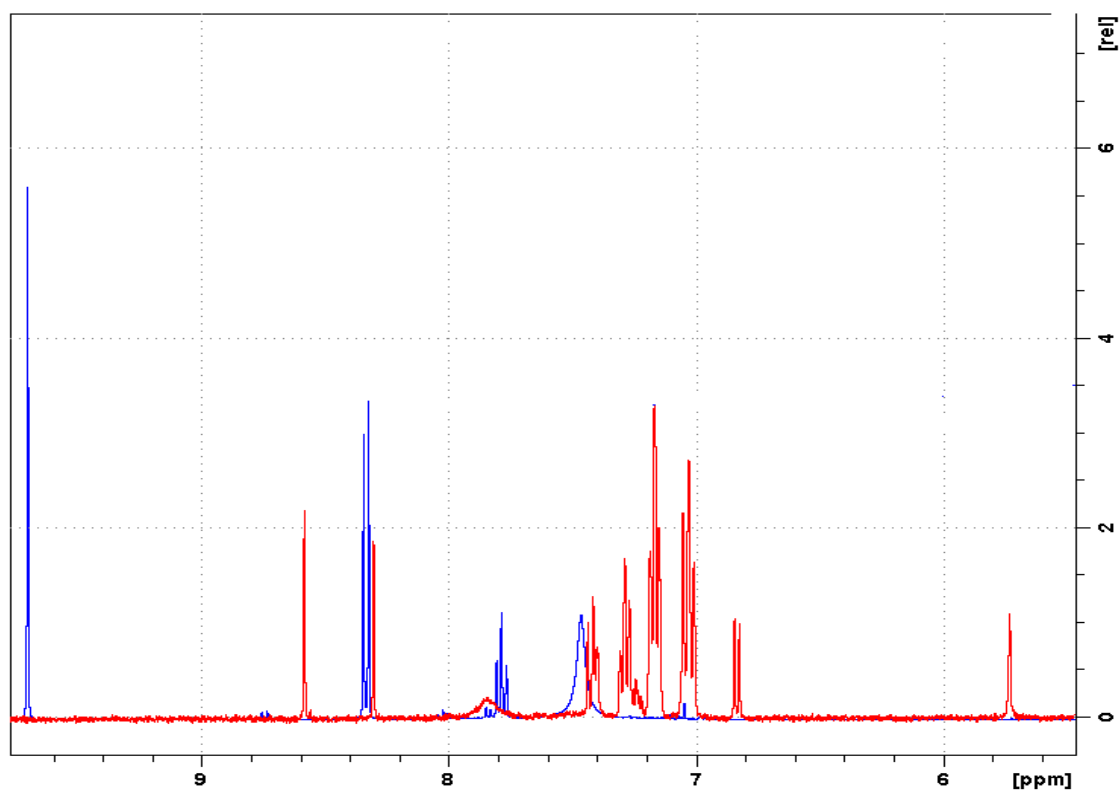


Figure 3.5: Overlay ^1H NMR spectra of H_4ucp (blue) and complex 3 (red).

IR spectra of all the complexes show the intense peaks of the *trans*-[Ru(PPh₃)₂] unit found nearly at the same positions between 750 and 695 cm⁻¹ [21]. Consistent with the ¹H NMR spectral analysis, coordination is also affirmed based upon shifts observed in IR spectra of **1** and **2** (see **Figures 3.6** and **3.7**) relative to their free Schiff bases. The imino stretching bands shift to higher frequencies (*e.g.* from 1611 cm⁻¹ in H₂tdp to 1665 cm⁻¹ in **1**) upon coordination. In addition, shifts were also observed for the intense bands of the tdp chelator in **1**, the $\nu(\text{S-CH}_3)$ in **2** and the $\nu(\text{C=O})$ in **3** (see **Figure 3.8**) relative to their respective free ligands. For **4** (see **Figure 3.9**) the disappearance of the Schiff base moiety (for H₃hdp at 1608 cm⁻¹) supports the fact that hydrolysis occurred. Furthermore, only one broad $\nu(\text{N-H})$ stretching band was found for the diamagnetic complexes **1** and **2**, opposed to the two $\nu(\text{N-H})$ stretching bands for complexes **3** and **4**.

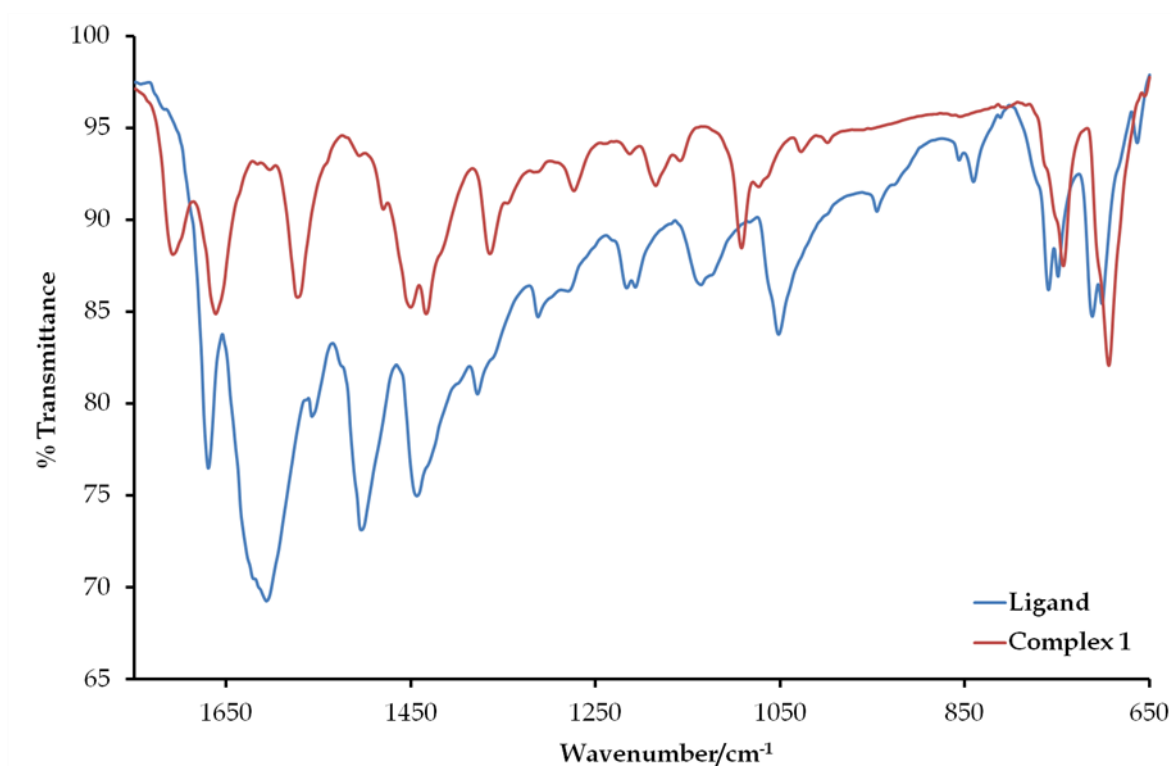


Figure 3.6: Overlay IR spectra of the free-ligand, H₂tdp and complex **1** between 1750 and 650 cm⁻¹.

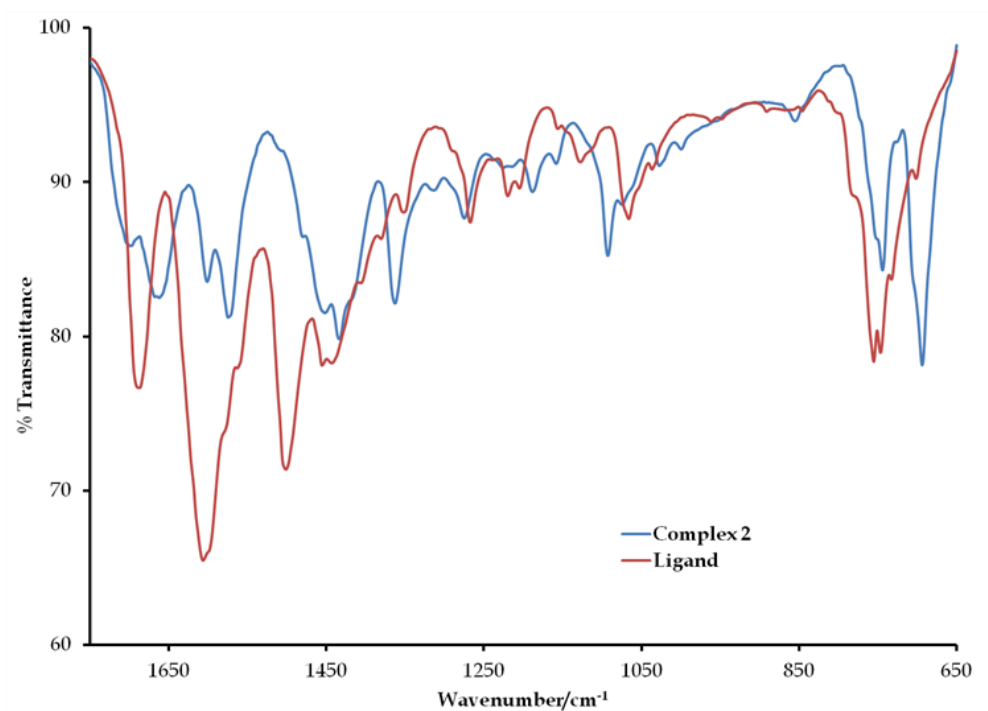


Figure 3.7: Overlay IR spectra of the free-ligand, H_2sdp and complex 2 between 1750 and 650 cm^{-1} .

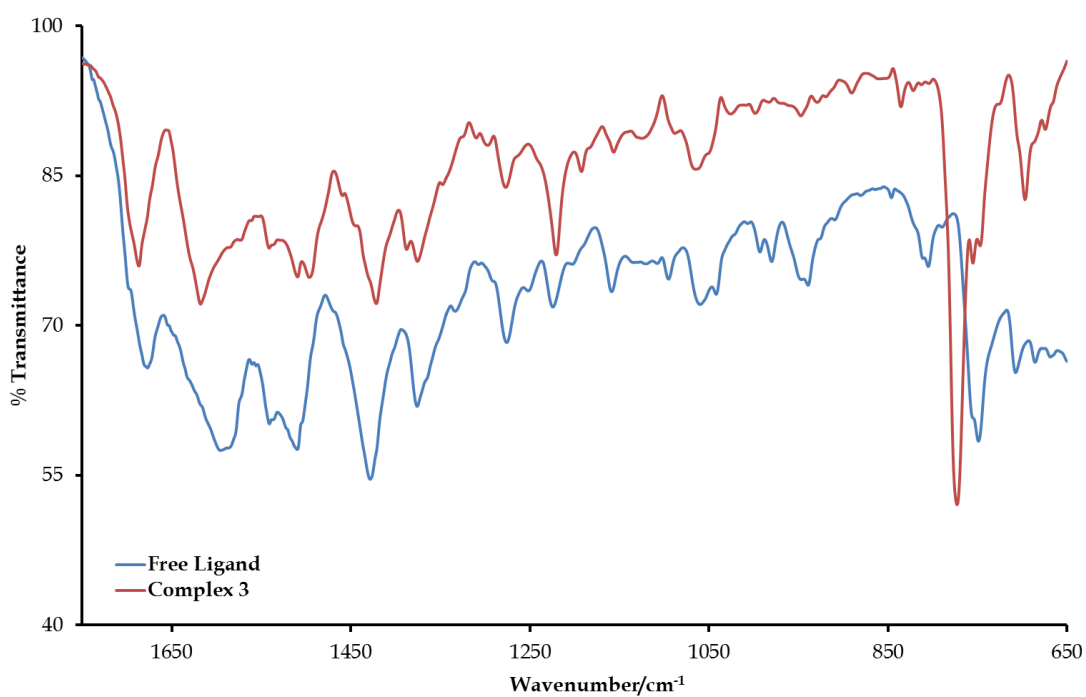


Figure 3.8: Overlay IR spectra of the free-ligand, H_4ucp and complex 3 between 1750 and 650 cm^{-1} .

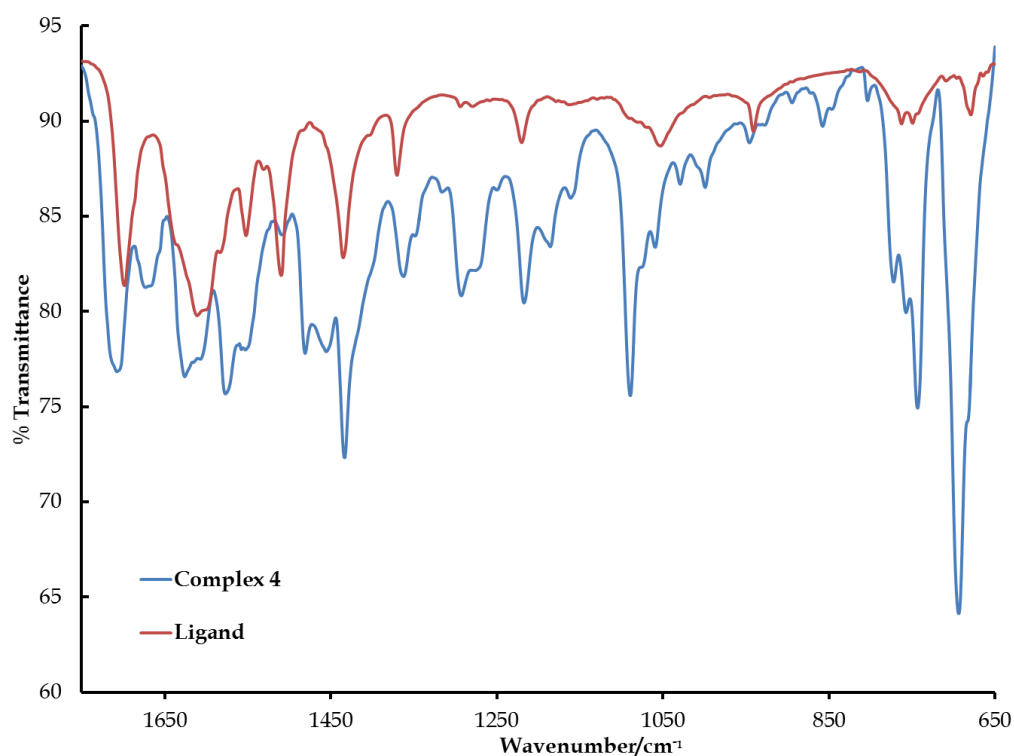


Figure 3.9: Overlay IR spectra of the free-ligand, H_2hdp and complex **4** between 1750 and 650 cm^{-1} .

The highly delocalized Schiff base chelators afford similarities between the UV/Vis spectra of the free Schiff bases and their metal complexes (see **Figures 3.10-3.13**). A series of common intra-ligand electronic transitions were observed for complexes **1**, **2** and **4** between 280 and 410 nm while the spectrum of **3** is dominated by only ligand-based electronic transitions. Broad Metal-to-Ligand Charge Transfer (MLCT) bands are found for complexes **1**, **2** and **4** at 507, 509 (for the d^6 metal complexes **1** and **2** respectively), and 515 nm for the d^4 metal complex **4**. These MLCT bands are typical of octahedral Ru(II/IV) complexes with aromatic chelating moieties [22, 23]. No d-d transitions are found for the diamagnetic complexes, which is due to their low-spin d^6 electron configurations. The same trend was observed with the paramagnetic d^4 complex, which is most likely due to a larger energy band gap which does not favour electronic transitions.

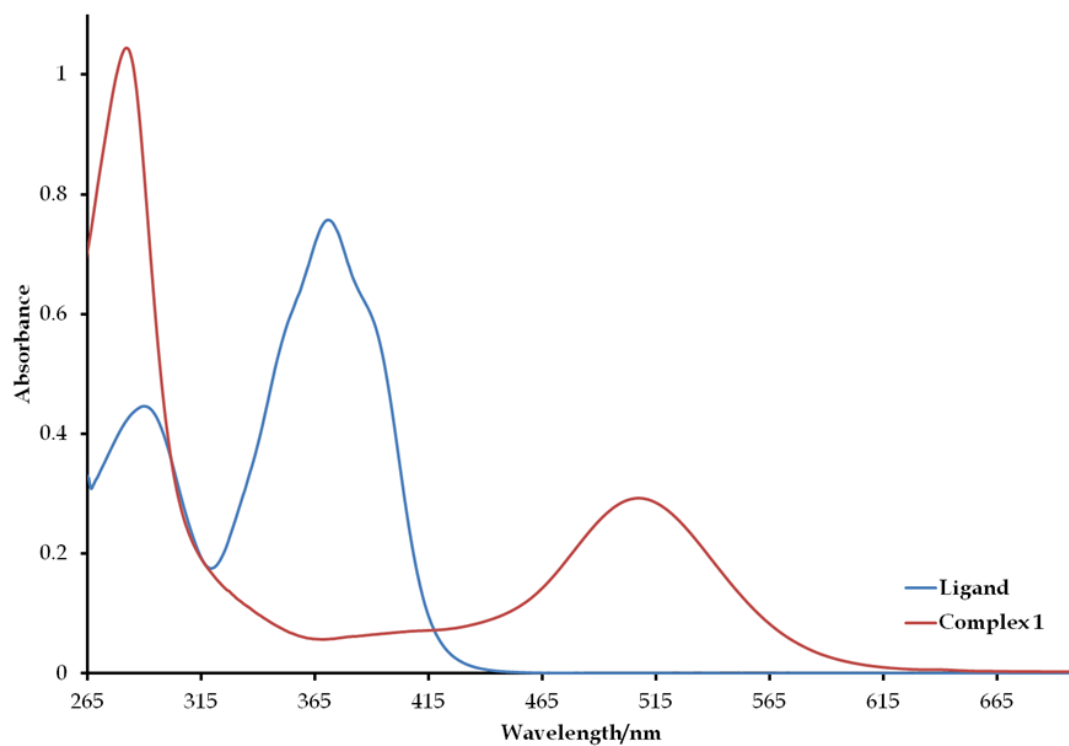


Figure 3.10: Overlay UV/Vis spectra of complex 1 and its ligand, H_2tdp .

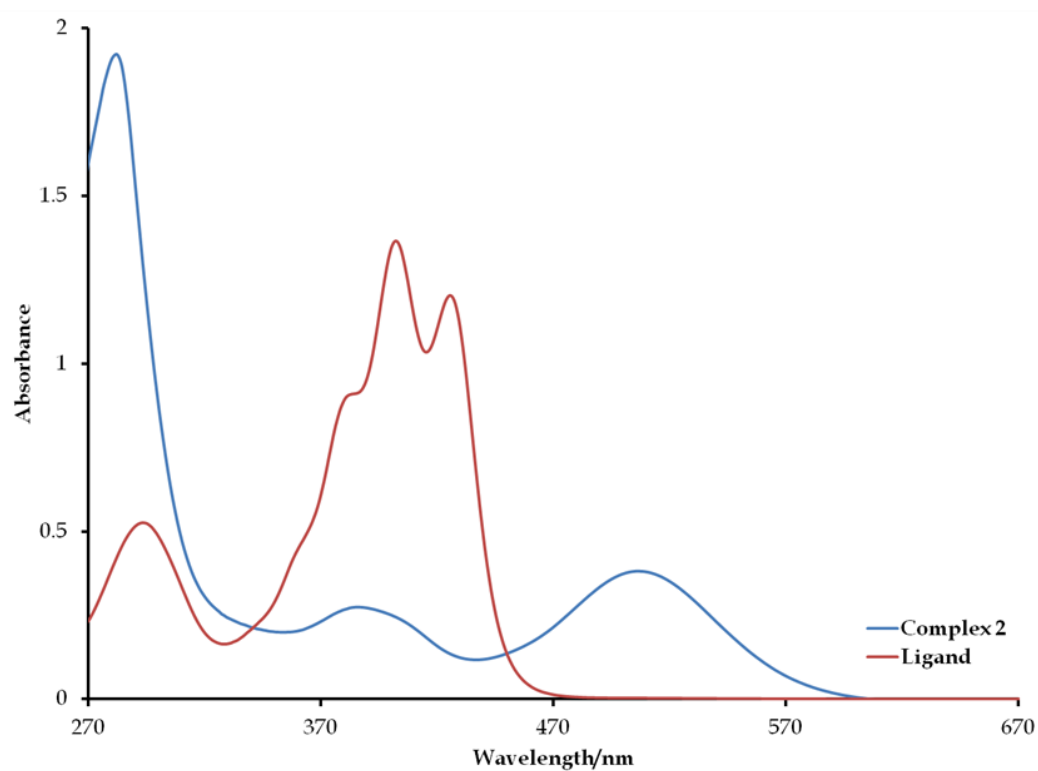


Figure 3.11: Overlay UV/Vis spectra of complex 2 and its ligand, H_2sdp .

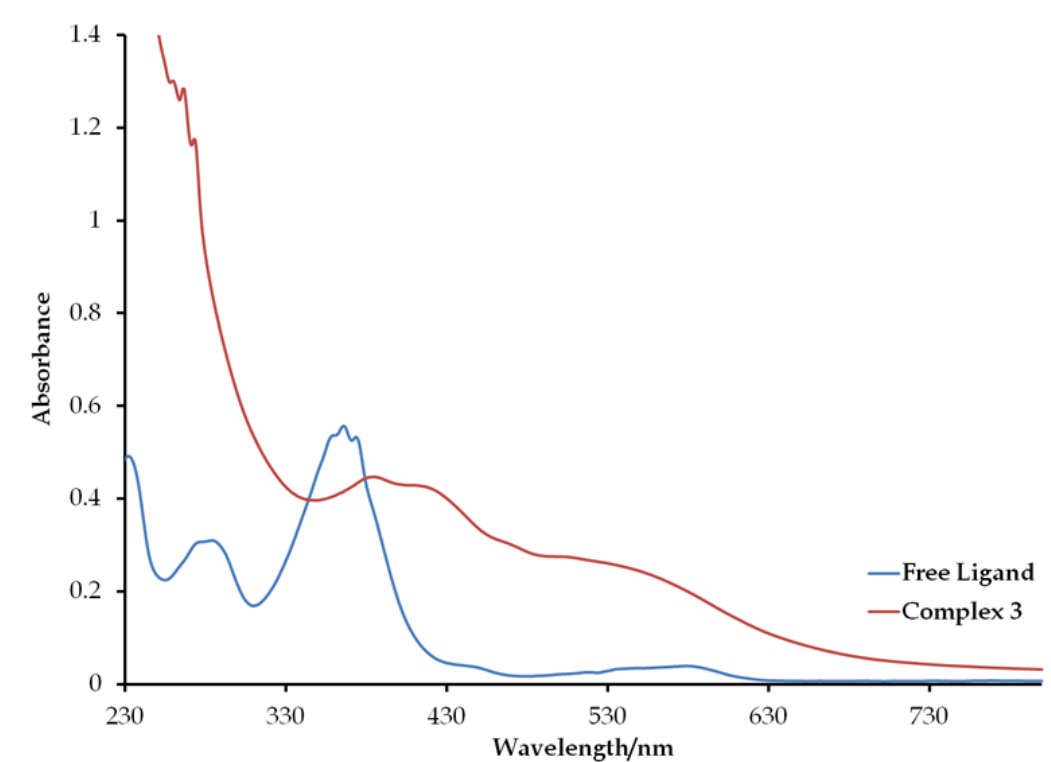


Figure 3.12: Overlay UV/Vis spectra of complex **3** and its ligand, H_4ucp .

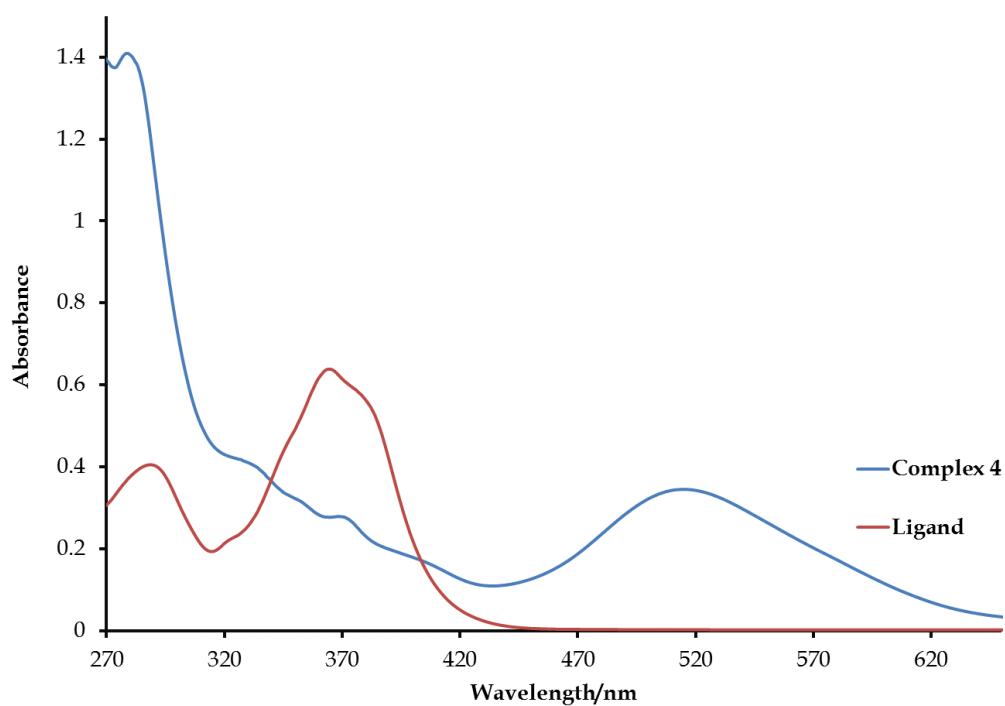


Figure 3.13: Overlay UV/Vis spectra of complex **4** and its ligand, H_2hdp .

As expected, ruthenium(II) complexes (**1**, **2** and **3**) exhibit ESR silent diamagnetic behaviour due to their non-variable spin states ($S = 0$), but ruthenium(IV) complexes can exhibit both diamagnetic ($S = 0$) and paramagnetic ($S = 1$) spin states depending on the nature of the ligand. A broad singlet (g_{iso} -value = 2.0757) observed in the X-band spectrum of **4** (see **Figure 3.14**) unequivocally confirms the presence of the paramagnetic Ru(IV) center. Similar to **4**, the one-electron electrochemically oxidized species (at 295 K) of $[Ru^{III}Q_3]$ $\{Q = 3,5\text{-di-}tert\text{-butyl-}o\text{-quinone}\}$ and $[Ru^{III}(Q_x)]$ $\{Q_x = 4,6\text{-ditert-butyl-}N\text{-phenyl-}o\text{-iminobenzoquinone}\}$ afforded isotropic singlets with $g_{iso} = 1.991$ and 2.001 , respectively [24].

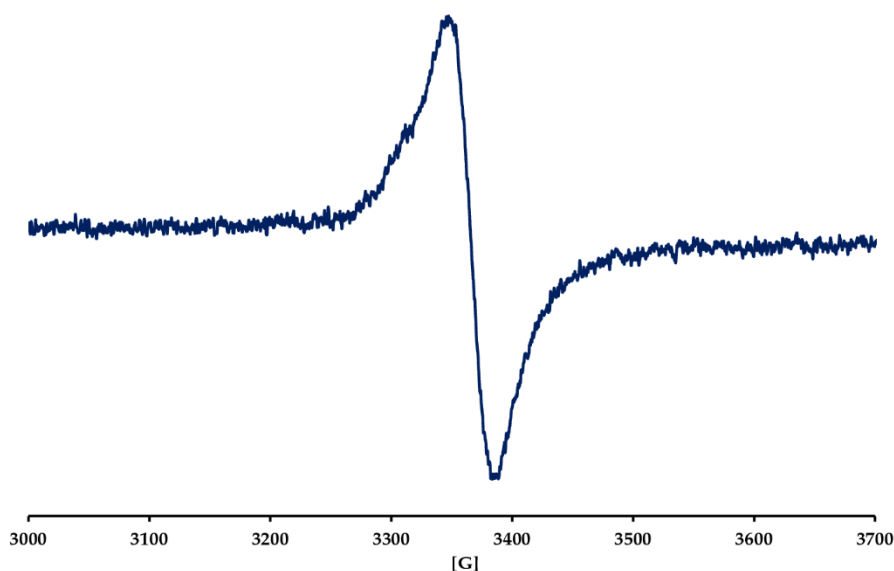


Figure 3.14: X-band EPR spectrum of **4** at 298 K. Instrument settings: microwave bridge frequency, 9.8 GHz; microwave bridge attenuator, 20 dB; modulation frequency, 100 kHz; modulation amplitude, 5 G; center field, 3500 G.

3.5.2 Electrochemistry

Each complex showed a single redox couple which exhibited diffusion controlled behaviour at increasing scan rates. For example, see **Figures 3.15** and **3.16** for the overlay cyclic voltammograms of **3** and **4** with scan rates ranging from 100 to 300

mV/s, at increments of 25 mV. Peak current ratios approaching one were observed for all complexes, implying that the redox couples are for one-electron redox processes. More interestingly, it is observed that **1** and **3** have smaller peak to peak separations ($\Delta E = 80$ mV for **1** and $\Delta E = 50$ mV for **3**, refer to **Table 3.1**) than ferrocene ($\Delta E = 90$ mV), which indicates faster electron transfer kinetics. However, slow electron transfer kinetics were observed for **2** and **4** which indicate quasi-irreversibility with peak to peak separations of 110 and 100 mV, respectively (see **Figure 3.17**).

Table 3.1: Selected CV Parameters (at 100 mV/s) for **1**, **2**, **3** and **4**.

	$E_{1/2}/V$	$\Delta E/mV$
Ferrocene	0.495	90
1	0.70	80
2	0.725	110
3	0.37	50
4	0.68	100

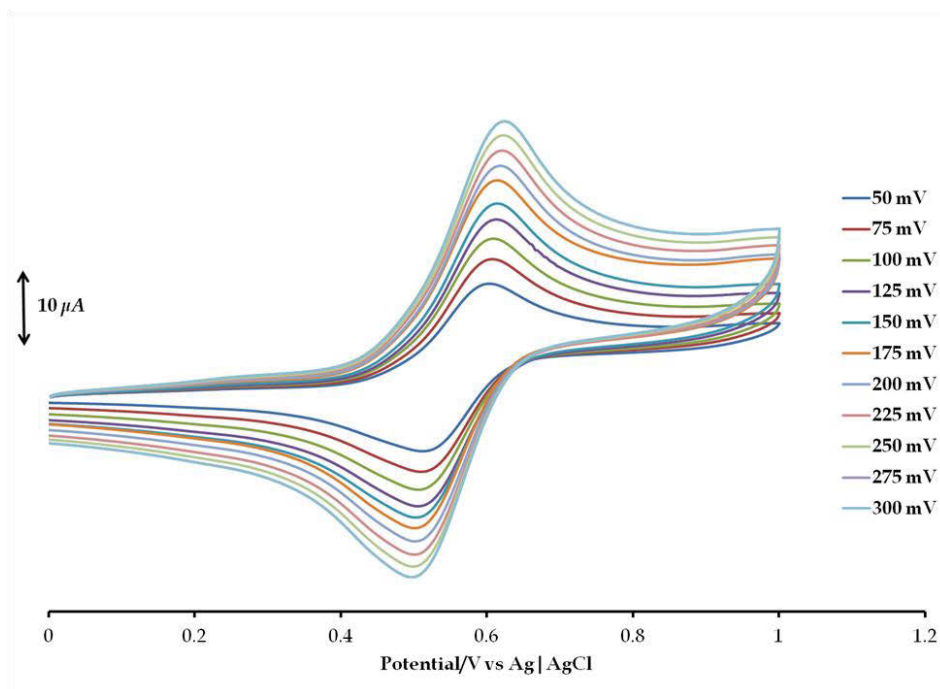


Figure 3.15: Overlay CVs of complex **3** at incrementing scan rates.

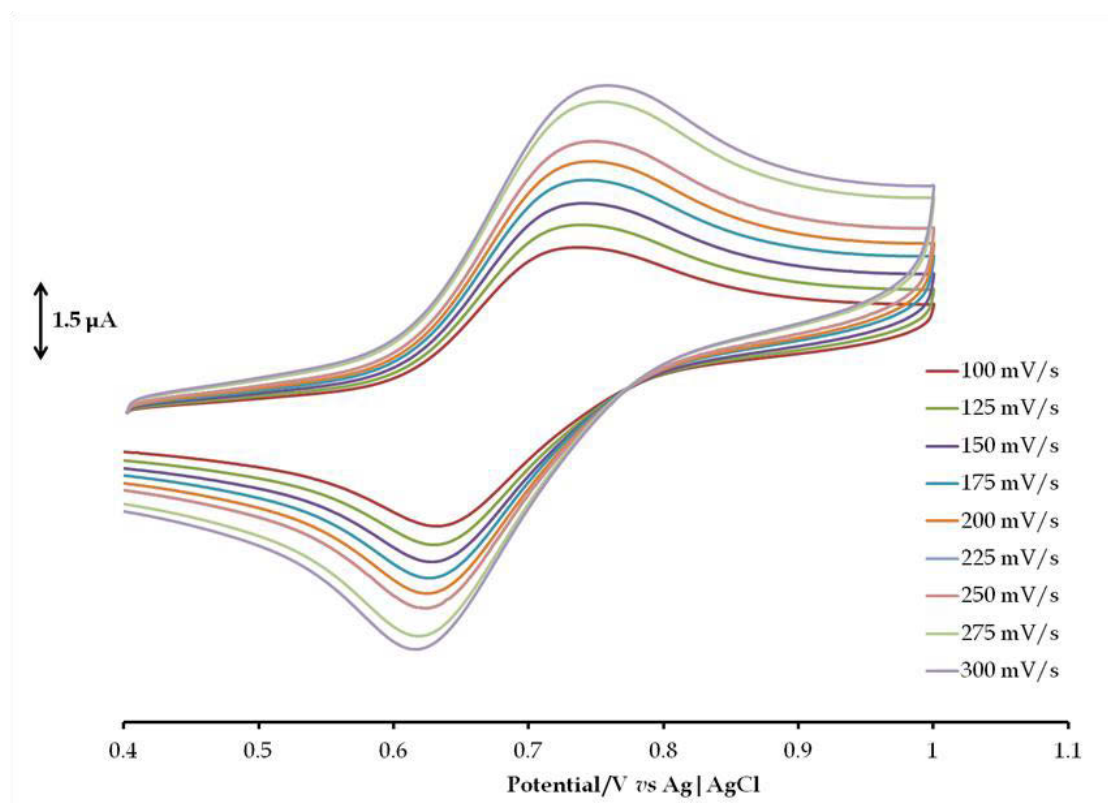


Figure 3.16: Overlay CVs of complex **4** at incrementing scan rates.

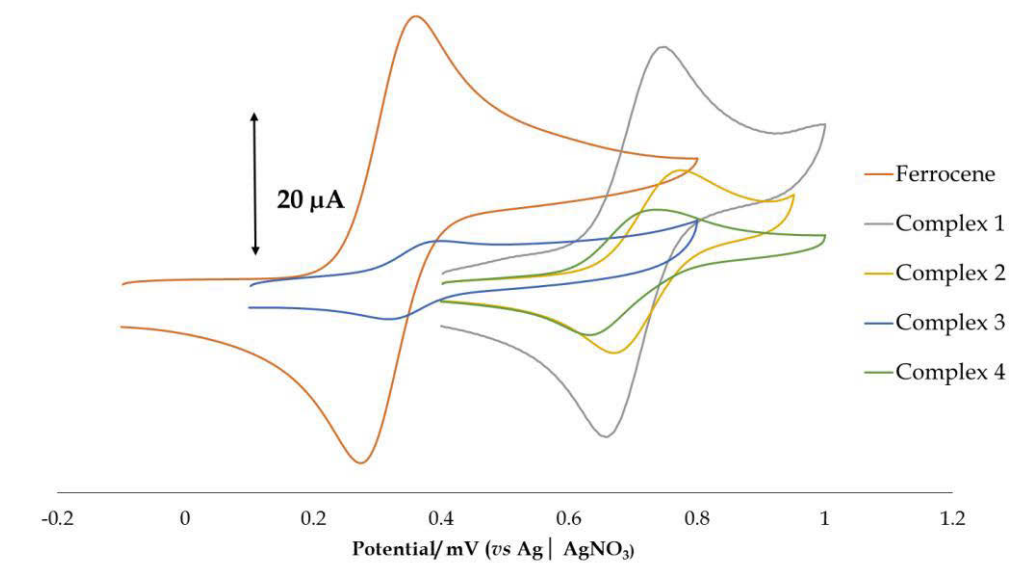


Figure 3.17: Overlay Cyclic Voltammograms of **1**, **2**, **3** and **4** as well as for the ferrocene standard. All experiments were done at a scan rate of 100 mV s^{-1} .

The redox couples of the complexes are ascribed to metal-based processes as they had similar half-wave potentials to other ruthenium complexes with Schiff base chelates. These literature trends show that for **1**, **2** and **3** the redox couple Ru(II/III) is observed, whereas for **4** it had similar half-wave potentials to ruthenium(III) compounds ascribed to the Ru(III/IV) redox couple. For example, in the case for the complexes, *trans*-[Ru^{II}(^RL)(PPh₃)₂(CO)Cl] {H^RL = (2-benzylimino-methyl)-4-*R*-phenol, R = H, Cl, Br or OMe}, which displays quasi-reversible metal centred processes in DCM between 0.62 and 1.16 V (*E*_{1/2} versus Ag | AgCl). The variable half-wave potentials are accounted to diverse electronic properties of R. When R had electron withdrawing character, a higher oxidation potential was induced and a reverse trend was found for electron donating R [25]. Paramagnetic ruthenium(III) compounds *trans*-[Ru^{III}(L)(PPh₃)₂Cl] in DCM showed comparable Ru(III/IV) redox couples (versus Ag | AgCl) [26].

3.5.3 Crystal Structures

(a) Crystal Structure of **1**

The metal is at the centre of a distorted octahedron with the basal plane defined by four donors, ClSN1N2, while the axial plane constitutes the *trans* triphenylphosphines (see **Figure 3.18**). The distortion is enforced by the Htdp tridentate chelator (within the basal plane), which affords two constrained five-membered chelate rings [S-Ru-N2 = 80.9(7)° and N1-Ru-N2 = 78.8(1)°]. As a result, the equatorial bond angles [Cl-Ru-N2 = 167.66(7)° and S-Ru-N1 = 159.14(8)°] deviate considerably from linearity. Inevitably, the N1-Ru-N2 bite angle induces a wider C6-N2-C6 [123.5(3)°] bond angle than the ideal 120° for a bridging *sp*² hybridized nitrogen. However, the C(5)=N(2) bond distance of 1.313(4) Å is indicative of a Schiff base coordinated to ruthenium(II) [18, 24]. The metal amido [Ru-N1 = 2.036(3) Å] bond is shorter than the metal imino [Ru-N2 = 2.053(2) Å] bond as expected, with the latter comparable to ruthenium(II) complexes with Schiff base chelates [18, 24]. For example, a Ru-N_{imino} bond of 2.084(3) Å was observed for [Ru^{II}(L₃)(CO)(PPh₃)] [27]. The nearly equidistance Ru-P bonds of **1** [Ru-P1 = 2.395(1) Å and Ru-P2 = 2.372(1) Å] forms a P1-Ru-P2 angle of 175.28(3)°.

Thiophene ligands exhibit diverse coordination modes ranging from $\eta^1(\text{S})$, $\eta^1(\text{C})$, $\eta^2(\text{C}_2)$, $\eta^4(\text{C}_4)$, and $\eta^5(\text{C}_4\text{S})$. A bond distance of 2.362(1) Å for the Ru-S bond is typical of $\eta^1(\text{S})$ coordination. The Ru-*S_{thienyl}* bond was similar to [Ru(bpy)₂-Y-P,S](PF₆)₂, where for Y = PT₃ (3-(diphenylphosphino)-2,2-terthiophene) or Y = PMe₂T₃ (5,5-dimethyl-3-(diphenylphosphino)-2,2:52-terthiophene) the bond distances were 2.346(1) and 2.362(2) Å, respectively [28]. The *sp*³ hybridized sulfur induces longer C-S [C1-S = 1.725(3) and C4-S = 1.749(3) Å] bond lengths within the thiophene ring, in comparison to delocalized C-S bonds found for uncoordinated thiophene rings. This implies that delocalization only occurs through the thiophene ring carbons, which is evident from the respective bond distances [C1-C2 = 1.353(4), C2-C3 = 1.426(4) and C3-C4 = 1.362(5) Å]. This was also observed for [Ru^{II}(bpy)₂(dppe-terth-P,S)](PF₆)₂ {bpy = 2,2-bipyridyl, dppe-terth = 3-(diphenylphosphino)-2,2:5'2-terthiophene} which had longer interthiophene ring C-S [1.744(3) and 1.751(3) Å] bond distances than its analogous compound, [Ru^{II}(bpy)₂(dppeterth-P,C)](PF₆)₂, with C-S bond distances of 1.720(6) and 1.735(1) Å [29]. The thiophene moiety of **1** lies out of the basal plane by 31.14°, which could be induced either by the break in delocalization between the bridging C-S-C within the ring system or the *pi*-stacking [interplanar spacing = 3.696 Å] between the thiophene ring and the C12-C17 phenyl ring of the triphenylphosphine co-ligand.

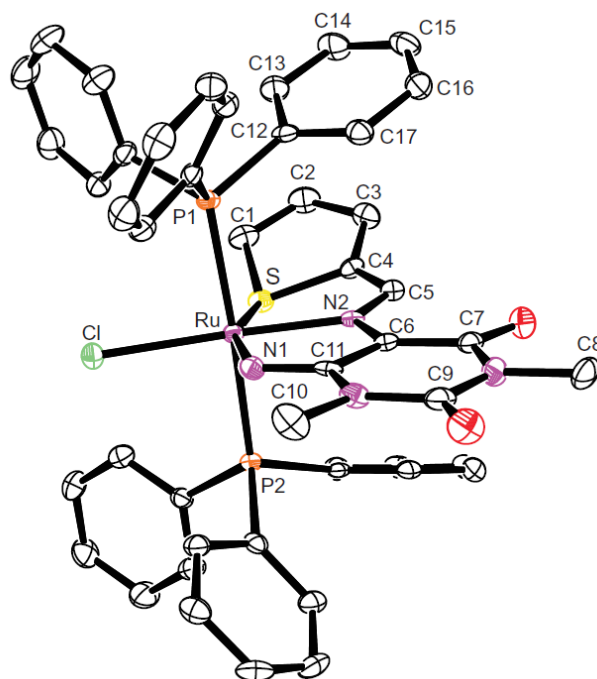


Figure 3.18: An ORTEP view of **1** showing 50% probability displacement ellipsoids and the atom labeling. Hydrogens were omitted for clarity.

(b) Crystal Structure of **3** ·CH₂Cl₂

The octahedron of **3** is defined by the N4-donor set of the monoanionic H3ucp chelator occupying the equatorial plane while the axial plane is defined by the ClRuP atoms. The octahedron of **3** is severely distorted as a result of the combined effect of the three five-membered chelate rings which results in the formation of three constrained bite angles [N4-Ru-N5 = 76.4(1)^o, N5-Ru-N6 = 81.2(1)^o and N6-Ru-N7 = 79.1(1)^o] which induces non-linear N4-Ru-N6 [157.4(1)^o] and N5-Ru-N7 [159.9(1)^o] bond angles (see **Figure 3.19**).

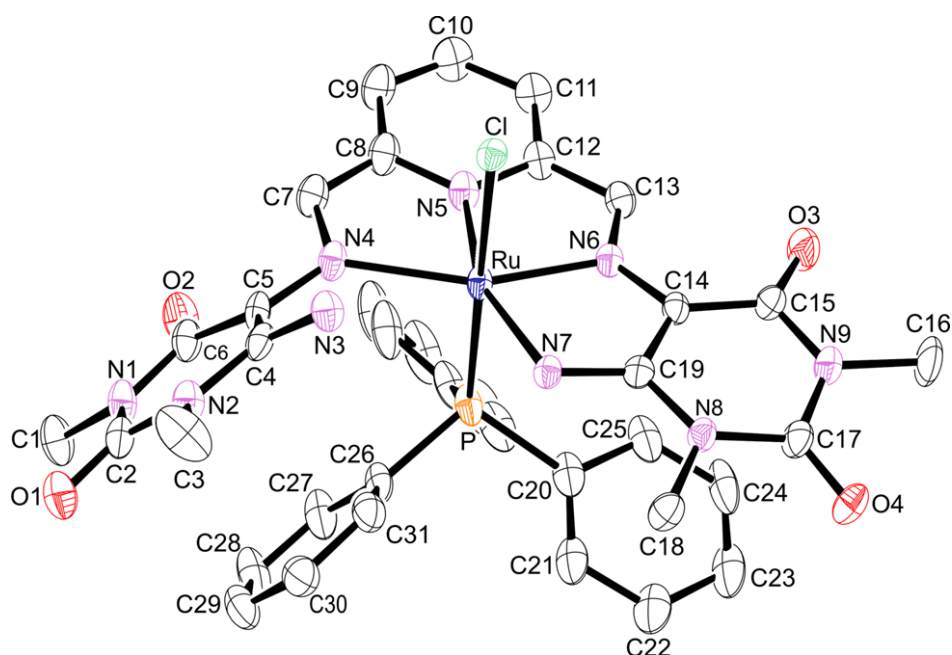


Figure 3.19: An ORTEP view of complex **3** showing 50 % probability displacement ellipsoids and the atom labelling. The hydrogen atoms were omitted for clarity.

The axial Cl-Ru-P [$172.96(3)^\circ$] bond angle is influenced by classical π - π stacking between the uracil rings and selected phenyl groups of the PPh_3 co-ligand given by the interplanar spacings of 3.431 Å (**I**) and 3.430 Å (**II**), see **Figure 3.20**. Furthermore, the intramolecular interactions cause the uracil moiety to lie substantially out of the N4-equatorial plane (at 42.64°). The bridging pyridyl nitrogen to ruthenium [1.957(5) Å] and Ru-Cl [2.4507(15) Å] bonds of *trans*-[Ru(Cl)(btrpy)(PPh_3) $_2$] PF_6 (btrpy = 4,4',4'-*tri-t*-butyl-2,2':6',2''-terpyridine) are similar to the Ru-N5 [1.954(4) Å] and the Ru-Cl [2.476(3) Å] bond distances of **3** [30]. The metal-amido bond distance of **3** [Ru-N7 = 2.143(4) Å] is within the range of 2.036(3)-2.292(9) Å found for other amido ruthenium(II) complexes [31, 32]. Interestingly, a large difference in the metal-imino bond distances [Ru-N4 = 2.189(3) Å and Ru-N6 = 2.001(3) Å] is noted and this phenomena extends also into the bond distances of the Schiff base moieties [N4-C7 = 1.314(5) Å and N6-C13 = 1.324(5) Å].

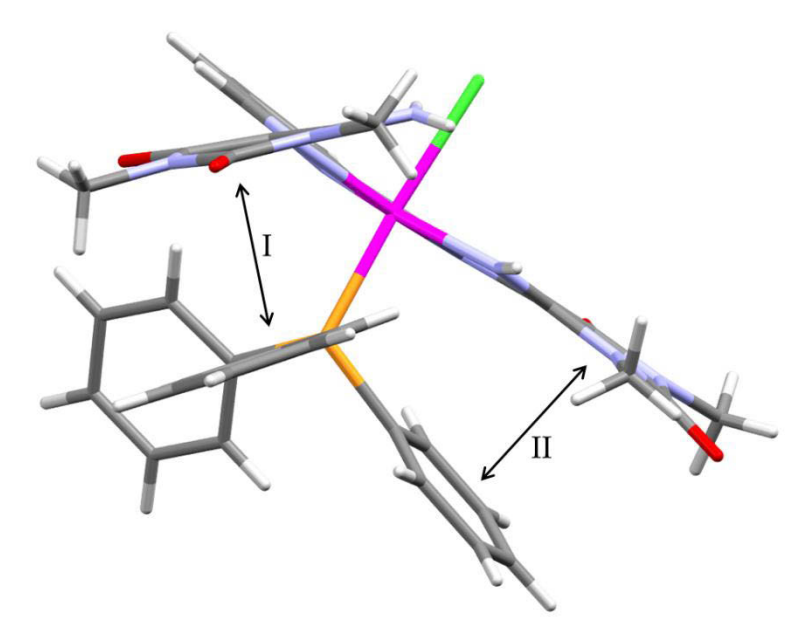


Figure 3.20: Demonstration of the intramolecular interactions occurring in complex **3**; given as **I** = 3.431 Å and **II** = 3.430 Å.

To understand these geometrical discrepancies, the geometry of **3** was optimized at the DFT level. The difference in the theoretical bond distances of Schiff base moieties [N4-C7 = 1.3010 Å and N6-C13 = 1.3225 Å] is also reflected in the optimized structure of **3**. The longer bond distance of the N6-C13 appears to emanate from the C13-N6-C14 delocalized π -system as opposed to localized N4-C7 double bond. This observation is further supported by shorter bond length of N6-C14 [1.3676 Å for optimized structure and 1.388(5) Å for crystal structure] compared to N4-C5 [1.4115 Å for optimized structure and 1.420(5) Å for crystal structure] observed within both the crystal and optimized structures which implies the latter exhibits single bond character. Consequently, the variable Natural Population Analysis (NPA) of the imino nitrogens [N4 = -0.392 and N6 = -0.282] are computed which results in the differences in the optimized [Ru-N4 = 2.3055 Å and Ru-N6 = 2.0196 Å] and experimental [Ru-N4 = 2.189(3) Å and Ru-N6 = 2.001(3) Å] Ru-N_{imino} bond distances. Several ruthenium compounds with derivatives of uracil and other nucleotide bases have been isolated, *e.g.* the arene ruthenium cationic compound, [Ru^{II}(Ur=C=C)(PPh₃)₂(η^5 -C₅H₅)](PF₆) which was formed from the uracil (Ur)-substituted alkyne Ur-C \equiv CH, NH₄PF₆ and [Ru(PPh₃)₂(η^5 -C₅H₅)Cl] [5]. Another example is the paramagnetic ruthenium(III)

compound, *trans*-[RuCl₄(DMSO)(H₂mtpo)].4H₂O which was isolated from the reaction between the adenine derivative, 5-methyl-1,2,4-triazolo[1,5-*a*]pyrimidin-7(4*H*)-one (H₂mtpo) and [H(DMSO)₂][*trans*-Ru(DMSO)₂Cl₄] [33].

(c) *Crystal Structure of 4 · CH₃Cl*

Complex **4** co-crystallizes with a chloroform molecule in a triclinic unit cell (see **Figure 3.21**). Within the N1N2Cl1Cl2 basal plane, the small N1-Ru-N2 [78.0(1)°] bite angle causes the chlorides to be further apart resulting in a Cl1-Ru-Cl2 angle [97.64(2)°] deviating from the ideal 90° angle. This is not surprising as the geometrical parameters of the five-membered chelate ring of **4** were similar to those found in the chelate rings of the ruthenium(II) bipyridine (bpy) complex, *cis*-[Ru(bpy)₂(CO)(OH₂)] [34]. The constrained five-membered chelate ring resulted in a non-ideal octahedron where the basal plane *trans* angles [Cl1-Ru-N1 = 175.29(8)° and Cl2-Ru-N2 = 164.70(7)°] angles deviate from linearity. Although no difference in steric hindrance between **1** and **4** that influences *trans*-axial linearity is observed, a smaller angle was observed for **4** [P1-Ru-P2 = 170.34(2)°] relative to **1** [175.28(3)°]. This larger difference in linearity for **4** could be ascribed to a weak intermolecular interaction between almost co-planar ring systems (centroid to centroid distance = 3.950 Å) of ddd and the C7–C12 phenyl ring of the P2-triphenylphosphine. This might also account for the small differences in bond distances found for the Ru-P bonds [Ru-P1 = 2.3878(7) and Ru-P2 = 2.4006(7) Å] (also observed in **1**).

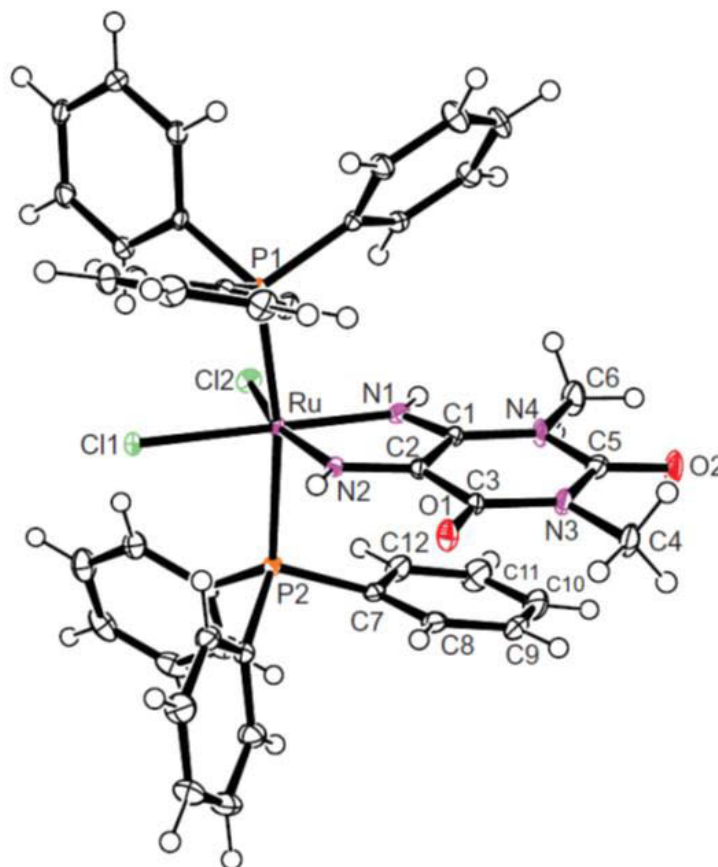


Figure 3.21: An ORTEP view of **4** showing 50% probability displacement ellipsoids and the atom labelling. The solvent of recrystallization has been omitted for clarity.

Noteworthy, the coordination sphere bond distances within the basal plane for **4** are shorter than in **1** due to stronger Lewis acid character of ruthenium(IV). The metal amido bonds [Ru-N1 = 2.017(3) and Ru-N2 = 1.969(3) Å] are not equal, due to the better electron withdrawing group next to N2, which causes a shorter metal amido bond. The *trans*-influence of the amido nitrogens on chlorides is different, with dissimilar metal to chloride bonds [Ru-Cl1 = 2.4218(7) and Ru-Cl2 = 2.4361(8) Å]. Several examples are found in literature of ruthenium(IV) compounds stabilized by amido donor chelates [35, 36]. Among these examples are [Ru^{IV}(bpy)(L-H)₂](PF₆)₂ and [Ru^{IV}(L-H₂)(L-H)₂](ZnCl) {L-H₂ = 2,3-diamino-2,3-dimethylbutane}, where a L-H moiety is a monoanionic bidentate chelator. These compounds were isolated from chemical oxidations *via* liquid bromine using the metal precursor, [Ru^{II}(bpy)(L-H₂)₂](X); X = PF₆ or ZnBr₄ [37].

Table 3.2: *Crystal Data and Structure Refinement Data for Complexes 1, 3 and 4.*

	1	3 ·CH₂Cl₂	4 ·CHCl₃
Chemical formula	C ₄₇ H ₄₁ ClN ₄ P ₂ RuS	C ₃₈ H ₃₇ Cl ₃ N ₉ O ₄ PRu	C ₄₂ H ₃₈ Cl ₂ N ₄ O ₂ P ₂ Ru·CHCl ₃
Formula weight	924.36	922.16	984.1
Temperature(K)	120(2)	100(2)	100(2)
Crystal system	P2 ₁ / <i>n</i>	P-1	P-1
Space group	Monoclinic	Triclinic	Triclinic
Unit cell dimensions (Å, °)	<i>a</i> = 15.0390(50)	<i>a</i> = 12.3357(5)	<i>a</i> = 12.5444(6)
	<i>b</i> = 17.3710(50)	<i>b</i> = 12.7812(7)	<i>b</i> = 12.9786(7)
	<i>c</i> = 16.0210(50)	<i>c</i> = 15.8388(6)	<i>c</i> = 14.9529(8)
	α = 90.000(5)	α = 68.056(2)	α = 71.528(3)
	β = 105.876(5)	β = 75.651(2)	β = 72.450(3)
	γ = 90.000(5)	γ = 79.853(2)	γ = 71.853(2)
Crystal size (mm)	0.20×0.10×0.10	0.20×0.12×0.08	0.4×0.05×0.05
V(Å ³)	4026(2)	2234.32	2137.89(19)
Z	4	2	2
Density (calc.) (Mg/m ³)	1.525	1.368	1.53
Absorption coefficient (mm ⁻¹)	0.634	0.613	0.796
F(000)	1896	936	1000
θ range for data collection (deg)	2.87–26.06	1.41–26.06	1.5–27.0
Index ranges	–18 ≤ <i>h</i> ≤ 17 –21 ≤ <i>k</i> < 20 –19 ≤ <i>l</i> ≤ 19	–15 ≤ <i>h</i> ≤ 15 –15 ≤ <i>k</i> < 10 –19 ≤ <i>l</i> ≤ 19	–15 ≤ <i>h</i> ≤ 15 –16 ≤ <i>k</i> < 16 –16 ≤ <i>l</i> ≤ 18
Reflections measured	29767	21876	25651
Observed reflections [<i>I</i> > 2σ(<i>I</i>)]	5483	8487	6780
Independent reflections	7957	7451	7696
Data/Restraints/parameters	7957/0/529	7451/0/521	7696/2/524
Goodness of fit on <i>F</i> ²	0.862	1.059	1.003
Observed <i>R</i> , <i>wR</i> ²	0.0360, 0.0756	0.0478, 0.1369	0.033, 0.083
<i>R</i> _{int}	0.0697	0.022	0.021

Table 3.3: Selected bond lengths [\AA] and angles [$^\circ$] for **1** and **4**.

1		4 CHCl_3	
Ru-N1	2.036(3)	Ru-N1	2.017(3)
Ru-N2	2.053(2)	Ru-N2	1.969(3)
Ru-Cl	2.4517(9)	Ru-Cl1	2.4218(7)
Ru-P1	2.395(1)	Ru-Cl2	2.4361(8)
Ru-P2	2.372(1)	Ru-P1	2.3878(7)
Ru-S	2.362(1)	Ru-P2	2.4006(7)
C5-N2	1.313(4)	N1-Ru-N2	78.0(1)
C1-S	1.725(3)	Cl1-Ru-Cl2	97.64(2)
C4-S	1.749(3)	Cl1-Ru-N1	175.29(8)
C1-C2	1.353(4)	Cl2-Ru-N2	164.70(7)
C2-C3	1.426(4)	P1-Ru-P2	170.34(2)
C3-C4	1.362(5)	-	-
S-Ru-N2	80.9(7)	-	-
N1-Ru-N2	78.8(1)	-	-
Cl-Ru-N2	167.66(7)	-	-
S-Ru-N1	159.14(8)	-	-
C6-N2-C6	123.5(3)	-	-
P1-Ru-P2	175.28(3)	-	-

Table 3.4: Selected bond lengths [\AA] and bond angles [$^\circ$] for **3**.

	Experimental	Optimized
Ru-N5	1.954(4)	1.9863
Ru-Cl	2.476(3)	2.5027
Ru-N7	2.143(4)	2.1799
Ru-N4	2.189(3)	2.3055
Ru-N6	2.001(3)	2.0196
N4-C7	1.314(5)	1.3010
N6-C13	1.324(5)	1.3225
N4-C5	1.420(5)	1.4115
N6-C14	1.388(5)	1.3676
Ru-P	2.294(1)	2.3683
N4-Ru-N5	76.4(1)	75.30
N5-Ru-N6	81.2(1)	80.88
N6-Ru-N7	79.1(1)	78.54
N4-Ru-N6	157.4(1)	155.50
N5-Ru-N7	159.9(1)	159.05
Cl-Ru-P	172.96(3)	173.55

3.6 References:

1. Gulcan, M., Sonmez, M., Berber, I. *Turk. J. Chem.*, 2012, **36**, 189.
2. Khan, G.S., Shah, A., Rehman, Z., Barker, D. *J. Photochem. Photobiol.*, 2012, **115**, 105.
3. Booysen, I.N., Ismail, B., Gerber, T.I.A., Akerman, M., van Brecht, B. *S. Afr. J. Chem.*, 2012, **65**, 174.
4. Potgieter, K., Mayer, P., Gerber, T., Yumata, N., Hosten, E., Booysen, I., Betz, R., Ismail, M., van Brecht, B. *Polyhedron*, 2012, **49**, 67.
5. Hamidov, H., Jeffery, J.C., Lynam, J.M. *Chem. Commun.*, 2004, 1364.
6. Fiol, J.J., García-Raso, A., Albertí, F.M., Tasada, A., Barceló-Oliver, M., Terrón, A., Prieto, M.J., Moreno, V., Molins, E. *Polyhedron*, 2008, **27**, 2851.
7. Khan, B.T., Annapoorna, K. *Inorg. Chim. Acta.*, 1990, **171**, 157.
8. Tselepi-Kalouli, E., Katsros, N. *Trans. Met. Chem.*, 1987, **12**, 467.
9. Oxford Diffraction. *CrysAlis CCD and CrysAlis RED*, Oxford Diffraction, Yarnton (2008).
10. Bruker APEX2, SAINT and SADABS. Bruker AXS Inc. (2010) Madison, Wisconsin, USA.
11. Sheldrick, G.M. *Acta Cryst.*, 2008, **A64**, 112.
12. Farrugia, L.J. *J. Appl. Cryst.*, 2012, **45**, 849.
13. Dolomanov, O.V., Bourhis, L.J., Gildea, R.J., Howard, J.A.K., Puschmann, H. *J. Appl. Cryst.*, 2009, **42**, 339.
14. Frisch, M.J., Trucks, G.W., Schlegel, H.B., Scuseria, G.E., Robb, M.A., Cheeseman, J.R., Scalmani, G., Barone, V., Mennucci, B., Petersson, G.A., Nakatsuji, H., Caricato, M., Li, X., Hratchian, H.P., Izmaylov, A.F., Bloino, J., Zheng, G., Sonnenberg, J.L., Hada, M., Ehara, M., Toyota, K., Fukuda, R., Hasegawa, J., Ishida, M., Nakajima, T., Honda, Y., Kitao, O., Nakai, H., Vreven, T., Montgomery, Jr., J.A., Peralta, J.E., Ogliaro, F., Bearpark, M., Heyd, J.J., Brothers, E., Kudin, K.N., Staroverov, V.N., Kobayashi, R., Normand, J., Raghavachari, K., Rendell, A., Burant, J.C., Iyengar, S.S., Tomasi, J., Cossi, M., Rega, N., Millam, J.M., Klene, M., Knox, J.E., Cross, J.B., Bakken, V., Adamo, C.,

- Jaramillo, J., Gomperts, R., Stratmann, R.E., Yazyev, O., Austin, A.J., Cammi, R., Pomelli, C., Ochterski, J.W., Martin, R.L., Morokuma, K., Zakrzewski, V.G., Voth, G.A., Salvador, P., Dannenberg, J.J., Dapprich, S., Daniels, A.D., Farkas, Ö., Foresman, J.B., Ortiz, J.V., Cioslowski, J., Fox, D.J. *Gaussian 09 (Revision A.01)*, 2009, Gaussian Inc., Wallingford CT.
15. Ogwenio, A.O., Ojwach, S.O., Akerman, M.P. *Dalton Trans.*, 2014, **43**, 1228.
 16. Al-Noaimi, M., El-Baighouthi, M.I., Abdel-Rahman, O.S., Haddad, S.F. *Polyhedron*, 2011, **30**, 1884.
 17. Gunasekaran, N., Remya, N., Radhakrishnan, S., Karvembu. R. *J. Coord. Chem.*, 2011, **64**, 491.
 18. Seth, D.K., Gupta, P. *Polyhedron*, 2012, **31**, 167.
 19. Nagaraju, K., Raveendran, R., Pal, S., Pal, S. *Polyhedron*, 2012, **33**, 52.
 20. Rodrigues, C., Batista, A.A., Ellena, J., Castellano, E.E., Benítez, D., Cerecetto, H., González, M., Teixeira, L.R., Beraldo, H. *Eur. J. Med. Chem.*, 2010, **45**, 2847.
 21. Wilton-Ely, J.D.E.T., Wang, M., Honarkhah, S.J., Tocher, D.A. *Inorg. Chim. Acta.*, 2005, **358**, 3218.
 22. Govindaswamy, P., Mozharivskyj, Y.A., Kollipara, M.R. *Polyhedron*, 2004, **23**, 1567.
 23. Ho, C., Che, C., Lau, T. *J. Chem. Soc., Dalton Trans.*, 1990, 967.
 24. Das, A.K., Hübner, R., Sarkar, B., Fiedler, J., Zális, S., Lahiric, G.K., Kaim, W. *Dalton Trans.*, 2012, 8913.
 25. Raveendran, R., Pal, S. *J. Organomet. Chem.*, 2010, **695**, 630.
 26. Raveendran, R., Pal, S. *J. Organomet. Chem.*, 2007, **692**, 824.
 27. Mandal, S., Mandal, S., Seth, D.K., Mukhopadhyay, B., Gupta, P. *Inorg. Chim. Acta.*, 2013, **398**, 83.
 28. Moorlag, C., Clot, O., Wolf, M.O., Patrick, B.O. *Chem. Commun.*, 2002, 3028.
 29. Moorlag, C., Wolf, M.O., Bohne, C., Patrick, B.O. *J. Am. Chem. Soc.*, 2005, **127**, 6382.
 30. Billings, S.B., Mock, M.T., Wiacek, K., Turner, M.B., Kassel, W.S., Takeuchi, K.J., Rheingold, A.L., Boyko, W.J., Bessel, C.A. *Inorg. Chim. Acta.*, 2003, **355**, 103.
 31. Boncella, J.M., Eve, T.M., Rickman, B., Abboud, K.A. *Polyhedron*, 1998, **17**, 725.

32. Hartwig, J.F., Anderson, R.A., Bergman, R.G. *Organometallics.*, 1991, **10**, 1875.
33. Fandzloch, M., Wojtczak, A., Sitkowski, J., Łakomska, I. *Polyhedron*, 2014, **67**, 410.
34. Oyama, D., Suzuki, K., Yamanaka, T., Takase, T. *J. Coord. Chem.*, 2012, **65**, 78.
35. Gonzalez, E., Brothers, P.J., Ghosh, A. *J. Phys. Chem.*, 2010, B, **114**, 15380.
36. Che, C., Cheng, W., Leung, W., Mak, T.C.W. *J. Chem. Soc., Chem. Commun.*, 1987, 418.
37. Chiu, W., Peng, S., Che, C. *Inorg. Chem.*, 1996, **35**, 3369.

Chapter 4

Novel Ruthenium(II) and (III) Compounds with Multidentate Schiff Base Chelates bearing the Chromone or 4-Aminoantipyrine Moieties

4.1 Introduction

There is no doubt that the chromone or antipyrine moieties have been receiving increasing attention for the design of novel organic and inorganic-based pharmaceuticals [1 - 5], see **Figure 4.1**. Their abundant biological activities originates from the structural similarities of the pyrazolone derivative and antipyrine with natural imidazole containing constituents which often results in inherent biological activities while chromone is a secondary metabolite. In addition, numerous examples in literature have shown that the inclusion of these biologically significant moieties promoted DNA intercalation. For example, DNA binding activities were observed for both the metal complexes, $[\text{NiO}_3(\text{L})]$ (L = 6-hydroxychromone-3-carbaldehyde thiosemicarbazone) and $[\text{CuL}^1]$ (L^1 = hydroxy-benzylidene-4-aminoantipyrine) and their respective free ligands [6, 7].

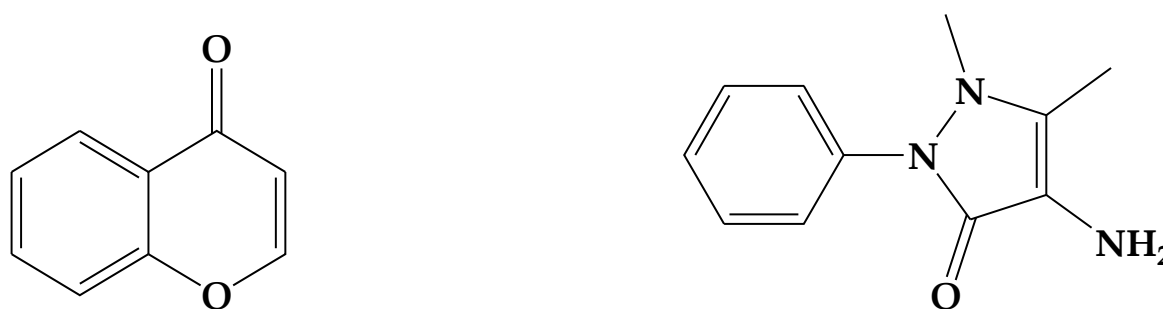


Figure 4.1: Molecular structures of chromone and antipyrine.

Many ruthenium complexes, containing Schiff bases derived from 4-aminoantipyrine and chromone, display a vast biological properties. Examples of these are the

organometallic ruthenium complexes, $[\text{RuCl}_2(\text{DMSO})_2(4\text{-aminoantipyrine})]$, which contains the O, N chelate of the 4-aminoantipyrine ligand, which has shown optimal DNA binding activity towards herrings sperm DNA [8, 9] and $[\text{Ru}(\text{phen})_2(\text{MCMIP})]^{2+}$ (phen = 1, 10-phenanthroline; MCMIP = 2-(6-methyl-3-chromonyl)imidazo[4,5-*f*](1,10-phenanthroline) which was reported to bind to DNA and cause cleavage [10, 11]. Another common observation for transition metal complexes containing these moieties is the coordination *via* the $\text{N}_{\text{Schiff base}}\text{O}_{\text{Keto}}$ donor atoms [3, 6].

In this chapter, we report the formation of ruthenium(II) and (III) compounds with multidentate Schiff bases containing the 4-aminoantipyrine and chromone moieties. The ruthenium compounds, *trans-P*, *cis-Cl*- $[\text{Ru}^{\text{III}}(\text{pch})\text{Cl}_2(\text{PPh}_3)_2]$ (**1**) and *cis*- $[\text{RuCl}_2(\text{bpap})(\text{PPh}_3)]$ (**2**) were isolated from the coordination reactions of *trans*- $[\text{RuCl}_2(\text{PPh}_3)_3]$ with the Schiff bases: 4-((pyridine-2ylimino)methylene)-chromone (pch) and 2,6-*bis*-((antipyrine-imino)methylene)pyridine (bpap) ligands, respectively.

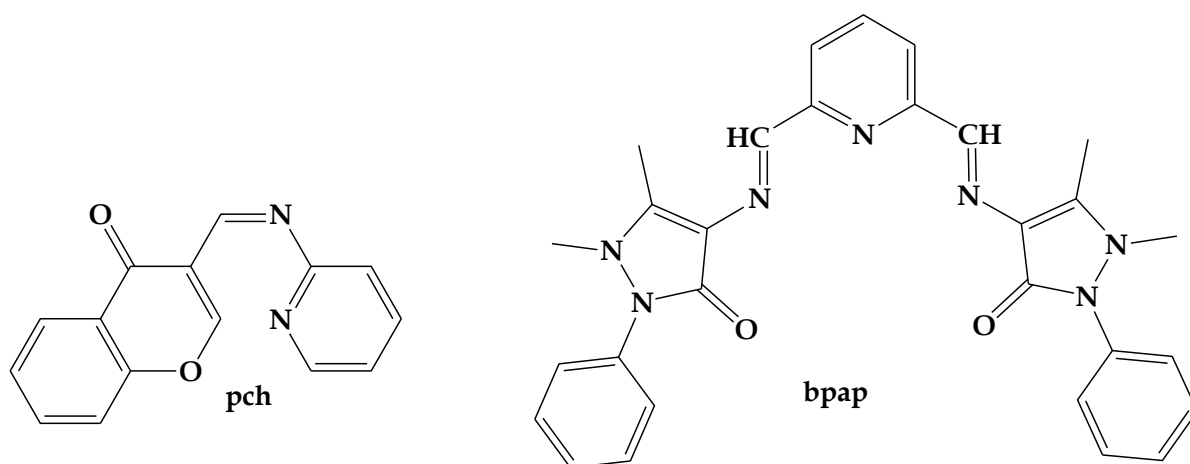


Figure 4.2: Structures and abbreviations of the Schiff bases.

4.2 Experimental

4.2.1 Synthesis of *trans-P*, *cis-Cl*- $[\text{Ru}(\text{pch})\text{Cl}_2(\text{PPh}_3)_2]$ (**1**)

A 1:1 molar reaction between pch (0.0261 g; 0.104 mmol) and *trans*- $[\text{RuCl}_2(\text{PPh}_3)_3]$ (0.100 g, 0.104 mmol) was heated at reflux in ethanol (30 cm³) for 3 hours. A blue precipitate was collected by filtration and washed with anhydrous di-ethyl ether. This

precipitate was dissolved in chloroform and layered with hexane and after several days, XRD quality blue parallelograms were attained using the slow diffusion method. Yield = 74% based on Ru, m.p. = 248 - 251°C. IR ($\nu_{\max}/\text{cm}^{-1}$): $\nu(\text{C}=\text{O})$ 1639 (m), $\nu(\text{C}=\text{N})$ 1613 (m), $\nu(\text{C}-\text{O}-\text{C})$ 1508 (s), $\nu[\text{Ru}-(\text{PPh}_3)_2]$ 693 (s). UV-Vis (DMF, λ_{\max} (ϵ , $\text{M}^{-1}\text{cm}^{-1}$)): 271 nm (9925); 322 nm (4897); 386 nm (3758); 478 nm (sh, 792); 636 (349). Conductivity (DCM, 10^{-3} M): $78.74 \text{ ohm}^{-1} \text{ cm}^{-2} \text{ mol}^{-1}$.

4.2.2 Synthesis of *cis*-[RuCl₂(bpap)(PPh₃)] (2)

The title compound was formed from the 1:1 molar ratio reaction of bpap (0.0527 g; 0.104 mmol) and *trans*-[RuCl₂(PPh₃)₃] (0.100 g, 0.104 mmol) in (20 cm³) toluene after 6 hours of reflux. A dark brown precipitate was filtered and recrystallized *via* the slow diffusion of a dichloromethane and *n*-hexane [1:1 (*v:v*)] solution which resulted in the formation of brown XRD quality parallelograms. Yield = 63% based on Ru, m.p. = 323 - 327°C. IR ($\nu_{\max}/\text{cm}^{-1}$): $\nu(\text{C}=\text{O})$ 1667, 1655, 1638 (s), $\nu(\text{C}=\text{N})$ 1591 (s), $\nu(\text{Ru}-\text{PPh}_3)$ 695 (vs); ¹H NMR (295K/ *d*⁶-CD₆SO/ ppm): 8.21 - 8.02 (m, 5H, *H*₁₂, *H*₁₄, *H*₁₅, *H*₁₆, *H*₁₈), 7.60 - 6.62 (m, 25H, *PPh*₃, *H*₂, *H*₃, *H*₄, *H*₅, *H*₆, *H*₂₅, *H*₂₆, *H*₂₇, *H*₂₈, *H*₂₉), 3.21 (s, 6H, *C*₇*H*₃, *C*₉*H*₃), 2.92 (s, 6H, *C*₂₁*H*₃, *C*₂₂*H*₃); ³¹P NMR (295K/ *d*⁶-CD₆SO/ ppm): 31.22. UV-Vis (DMF, λ_{\max} (ϵ , $\text{M}^{-1}\text{cm}^{-1}$)): 244 nm (sh, 26422); 279 nm (16393); 418 nm (4997); 498 nm (sh, 2754); 599 nm (sh, 1352). Conductivity (DMF, 10^{-3} M): $15.39 \text{ ohm}^{-1} \text{ cm}^{-2} \text{ mol}^{-1}$.

4.3 X-Ray Crystallography

The X-ray data for the metal complexes were recorded on a Bruker Apex Duo equipped with an Oxford Instruments Cryojet operating at 100(2) K and an Incoatec microsource operating at 30 W power. The data was reduced with the programme SAINT [12] and solved by direct methods using the SHELXS-97 [13] and WINGX [14] programmes. All non-hydrogen atoms were located in the difference density map and refined anisotropically with SHELXL-97 [13]. All hydrogen atoms were included as idealised contributors in the least squares process. Their positions were calculated using a standard riding model with C-H_{aromatic} distances of 0.93 Å and $U_{\text{iso}} = 1.2 U_{\text{eq}}$. The amido N-H bond of **1** as well as the solvents' C-H bonds of both complexes were

located in the difference density map and refined isotropically. Crystal and structure refinement data for the metal complexes **1** and **2** are given in **Table 4.1**. Selected bond lengths and angles are given in **Tables 4.2** and **4.3**.

4.4 Results and Discussion

4.4.1 Synthesis and Spectral Characterization

The novel ruthenium compounds **1** and **2** were isolated from the equimolar coordination reactions of *trans*-[RuCl₂(PPh₃)₃] with pch and bpap, respectively. The bpap ligand acts as neutral tridentate chelator which coordinates through its (N_{imino})₂N_{py} (in **2**) donor set (see **Figure 4.3 (2)**). Interestingly for **1**, the monoanionic pch chelator affords a constrained five-membered chelate ring through its formation of the ruthenium-carbene and the ruthenium-imino coordination bonds (see **Figure 4.3 (1)**). Thus, in contrast to compound **2**, which illustrates typical coordination affinity for pyridyl atoms, no pyridyl coordination bonding occurred for **1**.

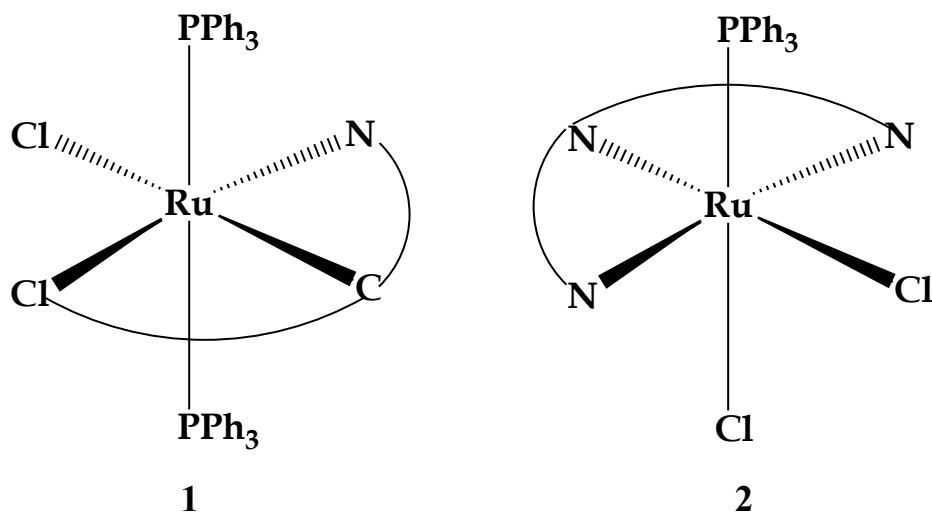


Figure 4.3: Coordination modes of the pch (**1**) and bpap (**2**) ligands.

The metal complexes dissolve readily in chlorinated solvents but exhibit partial solubility in other polar solvents such as methanol, ethanol and acetonitrile. Both complexes are non-electrolytes in dichloromethane. These conductivity measurements correspond well with other Ru(II) Schiff base complexes found in

literature ($13.5 - 18.4 \text{ ohm}^{-1}\text{cm}^2\text{mol}^{-1}$ for Ru(II) and $42 - 202 \text{ ohm}^{-1}\text{cm}^2\text{mol}^{-1}$ for Ru(III)) [15, 16]. The ^1H NMR spectrum of **2** show two multiplets accounting for the bridging imino and pyridyl protons (between 8.21 and 8.02 ppm) and the phenyl protons (between 7.60 and 6.62 ppm) of the aminoantipyrine moieties (see **Figures 4.4** and **4.5**). The presence of the phosphorous atom in **2** were confirmed by a single peak observed at 31.22 ppm in the ^{31}P NMR spectrum. This value is close to those found in literature for Ru(II) Schiff base compounds which contain two PPh_3 co-ligands *trans* to each other [17].

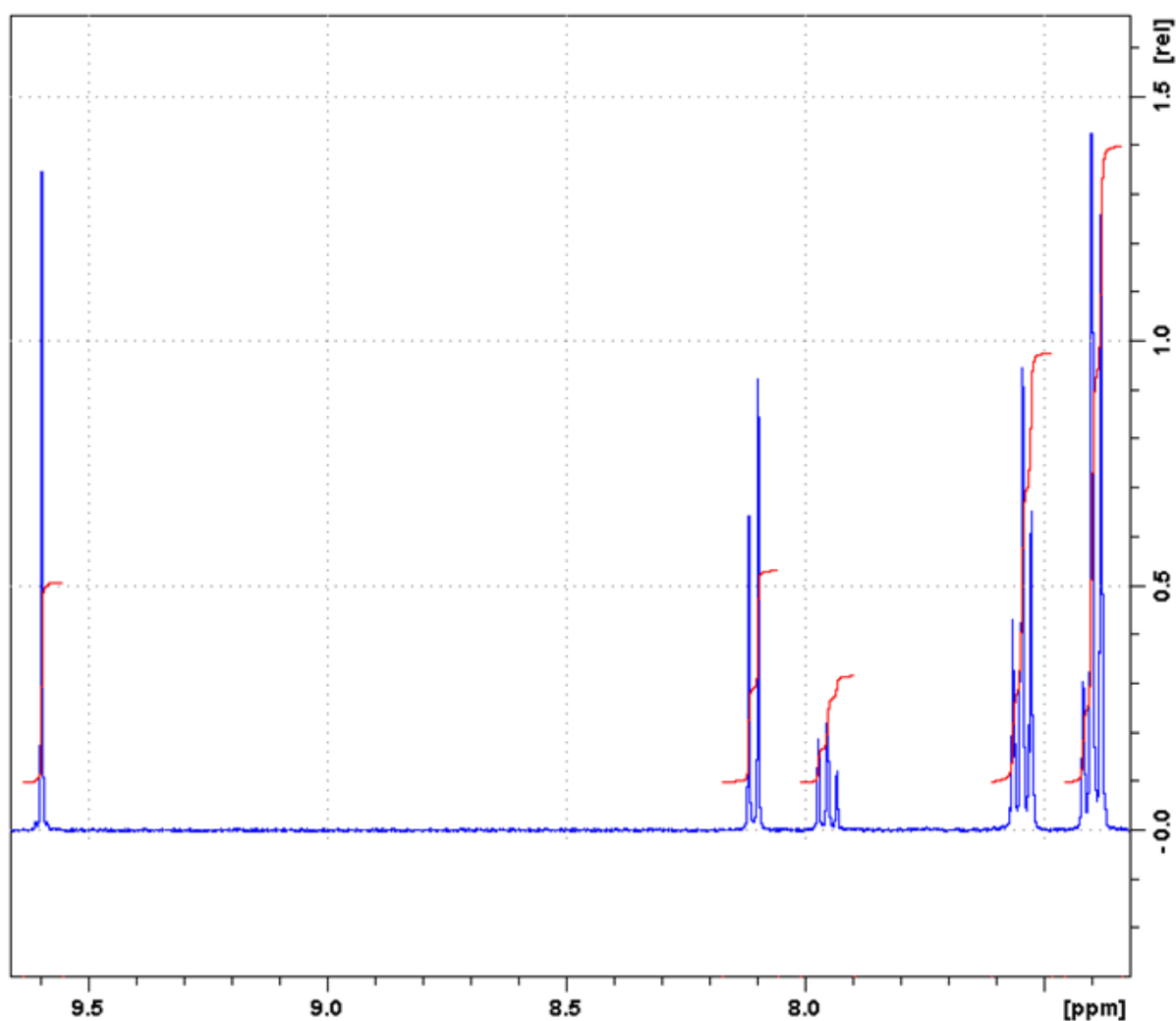


Figure 4.4: ^1H NMR spectrum of bpap, in the range 7.31 - 9.74 ppm.

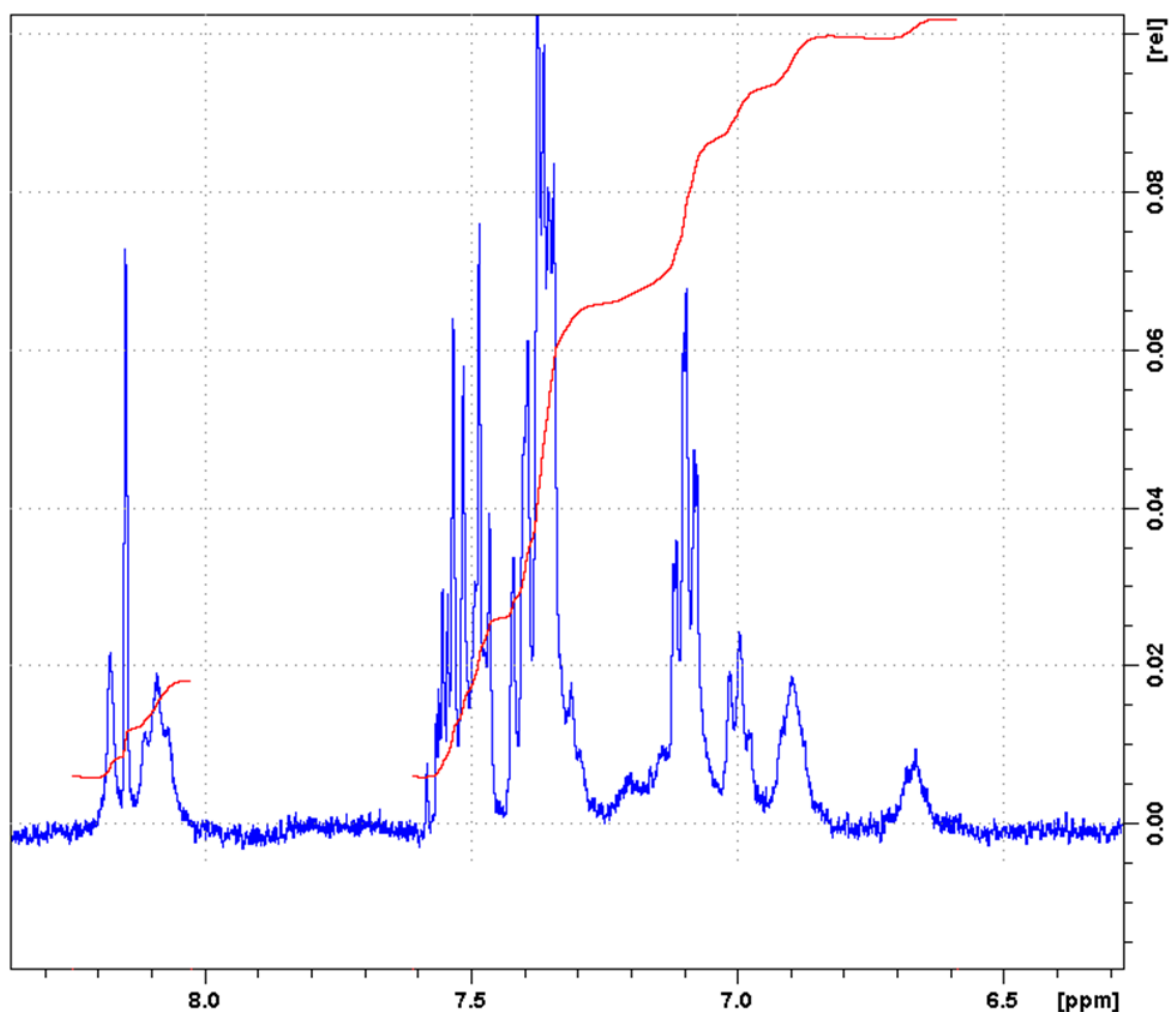


Figure 4.5: ^1H NMR spectrum of complex **2**, in the range 6.31 - 8.66 ppm.

No significant differences are observed between the IR spectra of the bpap ligand and its corresponding metal complex **2** as it contains neutral chelators (see **Figure 4.7**). In contrast for **1**, the ketonic and ether bonds [$\nu(\text{C}=\text{O})$ 1639 cm^{-1} and $\nu(\text{C}-\text{O}-\text{C})$ 1508 cm^{-1}] vibrates at higher frequencies compared to those of the free-ligand, pch [$\nu(\text{C}=\text{O})$ 1647 cm^{-1} and $\nu(\text{C}-\text{O}-\text{C})$ 1557 cm^{-1}] due to the difference in the stereoelectronic properties between the monoanionic coordinated (in **1**) and neutral uncoordinated chromone moieties (in the free ligand, pch), see **Figure 4.6**. In addition, the three strong imino bond vibrations (1611 , 1603 and 1590 cm^{-1}) of the free pch ligand coalesce into one medium-intensity vibration (at 1613 cm^{-1} for **2**) upon coordination. The characteristic Ru-PPh₃ stretches of compounds **1** and **2** were observed at 693 and 695 cm^{-1} respectively [18].

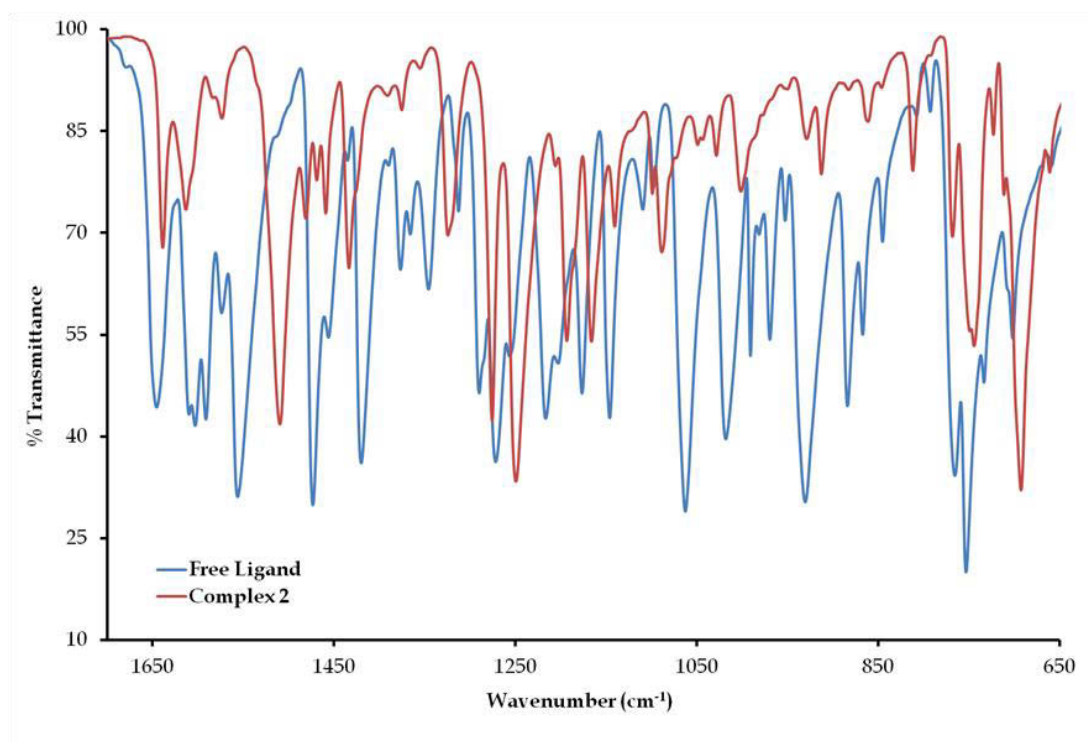


Figure 4.6: Overlay IR spectra of the free-ligand, *pch* and complex **1** between 1750 and 650 cm^{-1} .

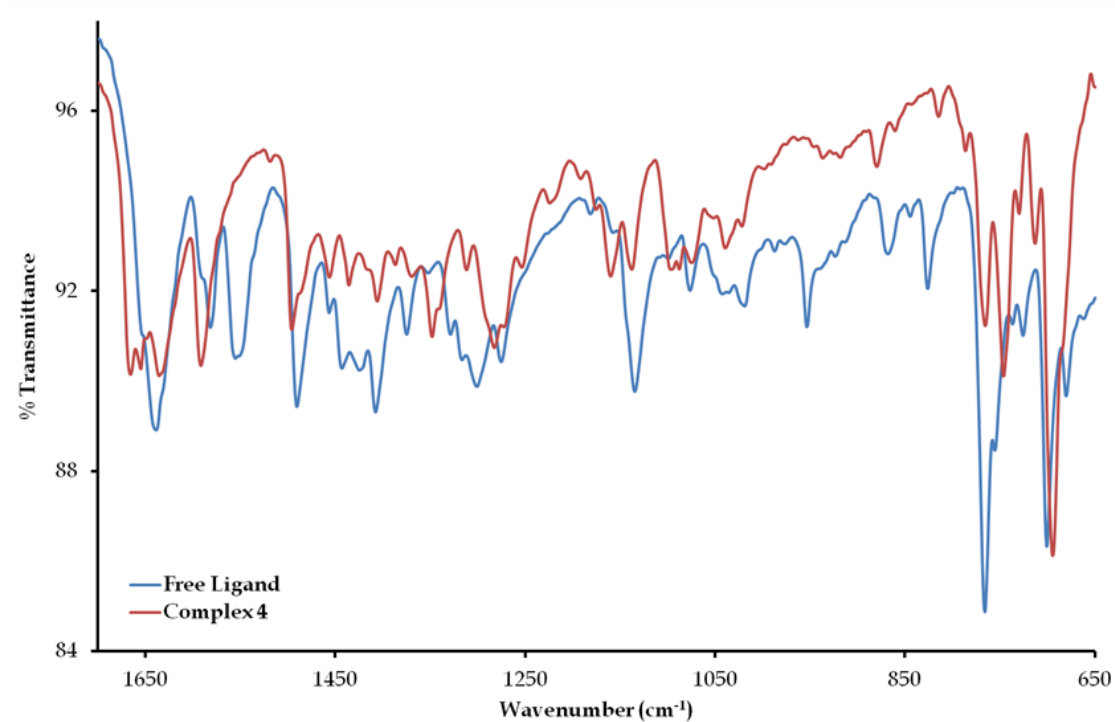


Figure 4.7: Overlay IR spectra of the free-ligand *bpap* and complex **2** between 1750 and 650 cm^{-1} .

The highly delocalized nature of the Schiff base chelators of the complexes are emphasized by the several common intraligand $\pi\text{-}\pi^*$ electronic transitions observed within the overlay UV/Vis spectra of the free-ligands and their respective metal complexes, see **Figures 4.8** and **4.9**. These electronic transitions are found below 400 nm. At more red-shifted wavelengths, metal-to-ligand charge transfer transitions were observed at 478 nm for **1** and 418, 498 and 599 nm for **2**. As expected, a $d\text{-}d$ electronic transition was observed for the paramagnetic ruthenium(III) complex **1** at 636 nm in comparison to none observed for the low-spin d^6 ruthenium(II) compound **2**.

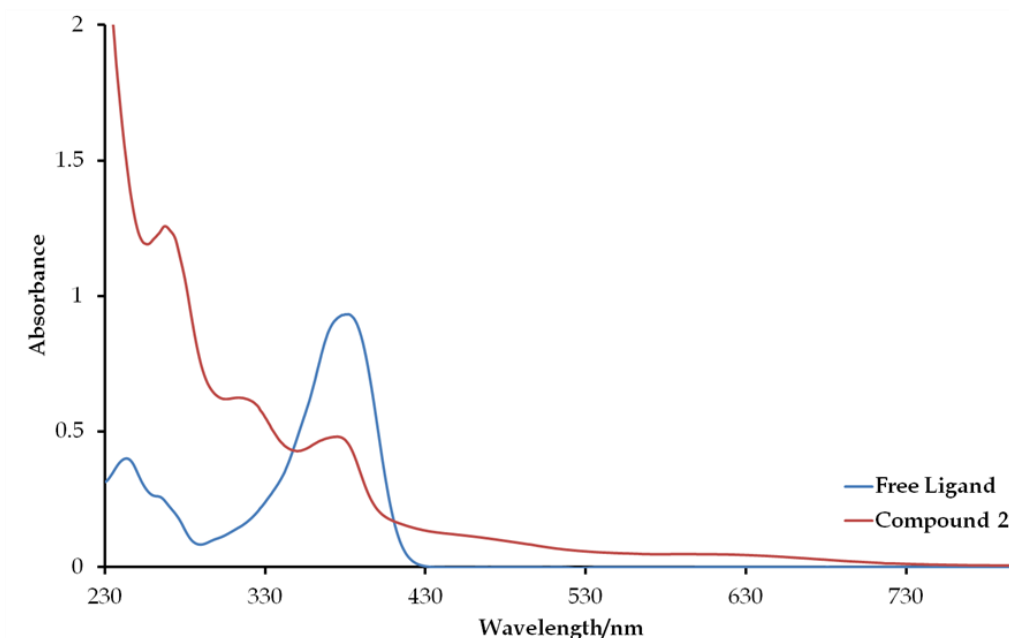


Figure 4.8: Overlay UV/Vis spectra of complex **1** and its ligand, *pch*.

The presence of the paramagnetic ruthenium(III) centre in complex **1** was confirmed *via* room temperature solution (in DCM) ESR spectroscopy, see **Figure 4.10**. The deviation (between 3300 and 4000 G) from the typical rhombic ESR spectrum reflects distortion of the octahedral geometry of **1** [19, 20]. In fact, the g -value (2.0951) for **1** is similar to that attained in the poorly resolved solution ESR spectrum of the ruthenium(III) complex, *trans*-[RuCl(bzp)(PPh₃)₂] (Hbzp = *N*-(2-hydroxybenzylidene)-benzimidazole) with a g -value of 2.1101 [20].

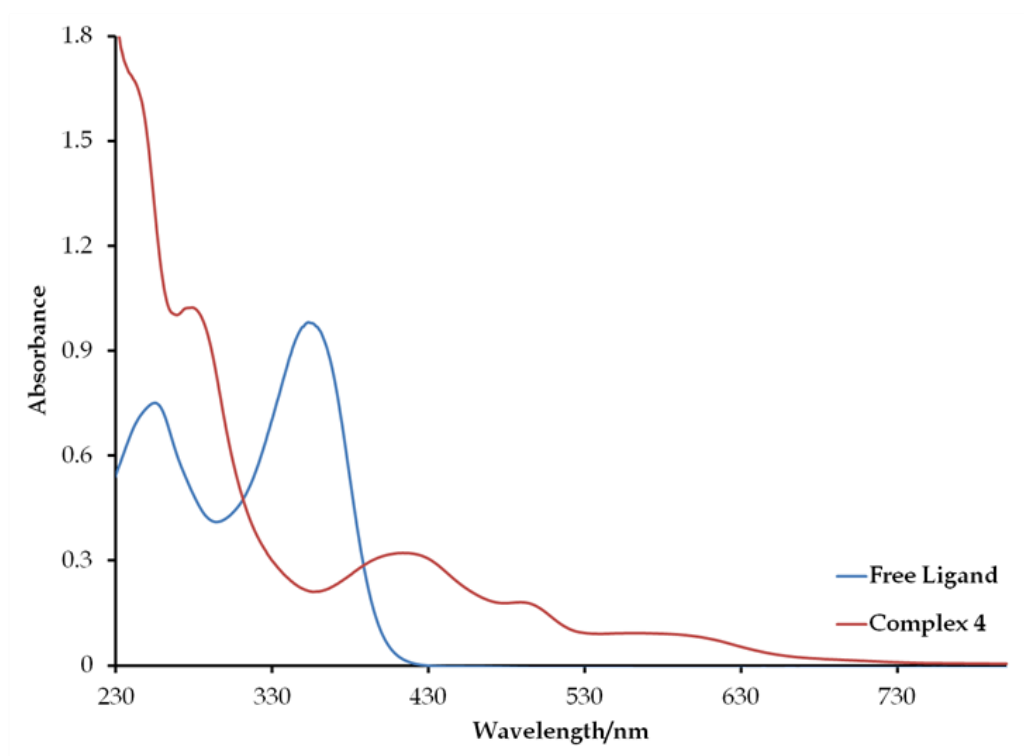


Figure 4.9: Overlay UV/Vis spectra of complex **2** and its ligand, *bpap*.

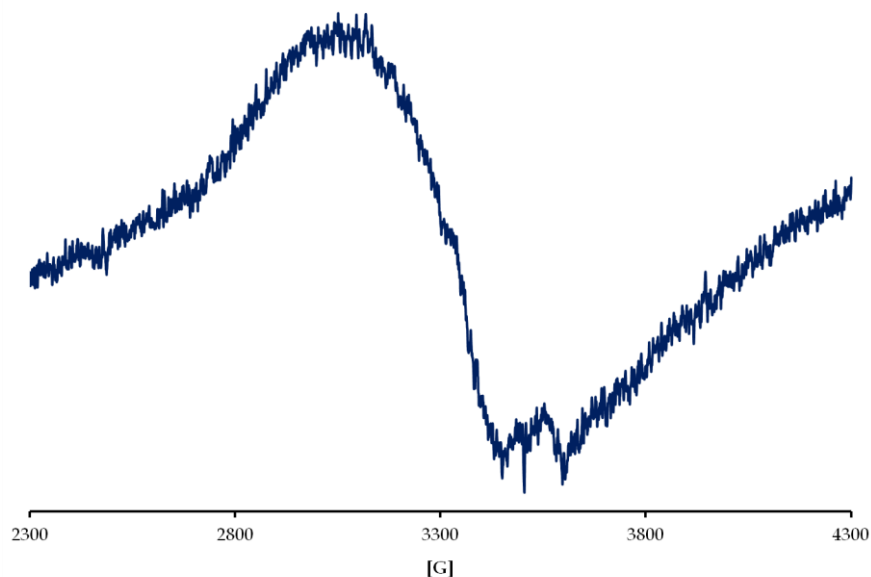


Figure 4.10: X-band EPR spectrum of **1** at 298 K. Instrument settings: microwave bridge frequency, 9.8 GHz; microwave bridge attenuator, 20 dB; modulation frequency, 100 kHz; modulation amplitude, 5 G; centre field, 3500 G.

4.4.2 Electrochemistry

The redox properties of the metallic compounds were probed using cyclic voltammetry, refer to **Figures 4.11 - 4.12**. All the attained cyclic voltammograms (CVs) were diffusion controlled at incrementing scan rates, *e.g.* see the overlay CVs of **1** in **Figure 4.11** as an example. These CVs are classified as one-electron redox processes as their peak current ratios approach one. In addition, all the CVs exhibits quasi-reversible behaviour since their respective peak to peak separations [$\Delta E_p = 120$ mV for **1** and 90 mV for **2**] are different from that of the standard, ferrocene [$\Delta E_p = 80$ mV at 100 mV/s].

The different peak to peak separations of the two complexes are due to the more delocalized diimine chelator of **2** which promotes faster electron transfer kinetics in comparison to the mono-imine chelator of **1**. This phenomenon is further supported by the fact that **2** [$E_{1/2} = 0.32$ V *vs* Ag | AgCl] has a smaller halfwave-potential ($E_{1/2}$) compared to **1** [$E_{1/2} = 0.56$ V *vs* Ag | AgCl].

The redox processes as found in the respective CVs are ascribed to the Ru(II)/Ru(III) redox couples since they have similar half-wave potentials ($E_{1/2}$) as the ruthenium(II/III) compounds with Schiff base chelates found in literature. For example, nearly equivalent half-wave potentials were observed between the paramagnetic ruthenium(III) compound, **1** [$E_{1/2} = 0.56$ V *vs* Ag | AgCl] and *trans*-[Ru^{III}(nbh)(PPh₃)₂Cl] (H₂nbh = *N*-benzylidene-4-nitrobenzohydrazide) [$E_{1/2} = 0.58$ V *vs* Ag | AgCl] [**21**].

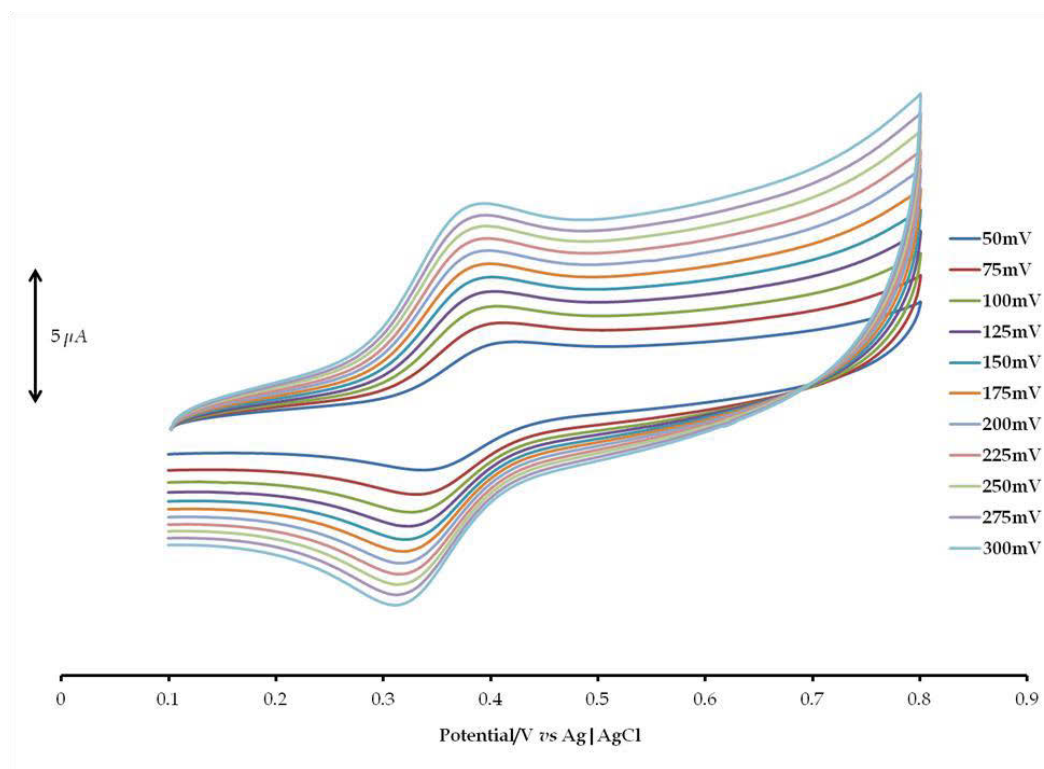


Figure 4.11: *Overlay CVs of complex 1 at incrementing scan rates.*

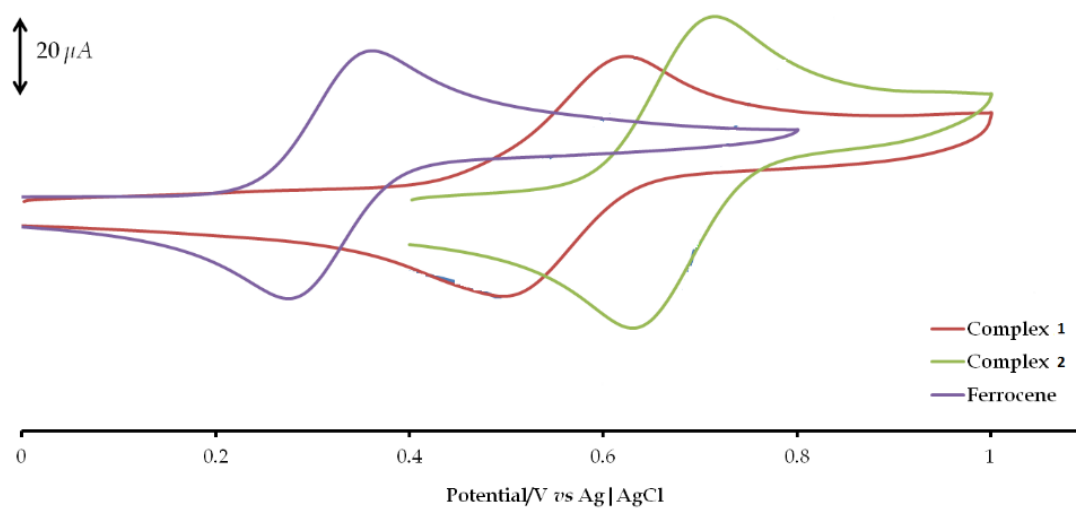


Figure 4.12: *Overlay CVs of compounds 1 (at 300 mV/s), 2 (at 300 mV/s) and ferrocene (at 100 mV/s).*

4.4.3 Crystal Structures

(a) Crystal Structure of **1** · 2CHCl₃

Compound **1** crystallizes in a $P2_1/c$ space-group along with two chloroform molecules of recrystallization, see **Figure 4.13**. The ruthenium metal atom is at the centre of a distorted octahedron which is largely induced by the constrained RuN2C6C7C15 five-membered chelate ring. Consequently the equatorial bite angle, N2-Ru-C15 [78.6(2)°] is considerably smaller than the bond angle formed between *cis*-chloro [Cl1-Ru-Cl2 = 88.55(4)°] co-ligands, which are close to octahedral ideality [*i.e.* 90°]. Furthermore, the nearly linear P1-Ru-P2 bond angle of 176.31(4)° is influenced by intramolecular interactions between the uncoordinated pyridyl moiety of the pch chelator and selected phenyl groups of the triphenylphosphine co-ligands, see **Figure 4.14** [I = 3.729 Å and II = 3.663 Å].

The difference in the bond lengths of the *cis*-chloro co-ligands [Ru-Cl1 = 2.452(1) Å and Ru-Cl2 = 2.575(1) Å] is due to the variable *trans*-influence of the N2 and C15 atoms, respectively. The bond length of the Ru(III)-N_{Schiff base} bond [2.151(4) Å] is similar to the analogous coordination bonds found in other paramagnetic ruthenium(III) compounds, [RuCl(bsp)₂(PPh₃)] [2.119(2) Å and 2.096(2) Å] (Hbsp = *N*-(2-hydroxybenzylidene)-benzothiazole) and *trans*-[RuCl(bzp)(PPh₃)₂] [2.069(4) Å] (Hbzp = *N*-(2-hydroxybenzylidene)-benzimidazole) [18]. In compound **1**, the ruthenium-carbene bond distance [1.933(5) Å] is shorter than the Ru(III)-C_{aromatic} bond distances of *trans*-[Ru(pnbhMe)(PPh₃)₂Cl] [2.048(3) Å] (H₂pnbhMe = 1-pyrenaldehyde-4-methyl-benzoylhydrazone) and *trans*-[RuCl(nabhMe)(PPh₃)₂] [2.040(6) Å] [22, 23]. This is ascribed to the variable stereoelectronic properties of the hydrocarbon rings of the naphthalene and pyrenyl rings in comparison to the chromone moiety. However, the ruthenium-carbene bond distance of **1** is comparable to the organometallic complex, *trans*-[RuCl(bzp)(PPh₃)₂] with a Ru-C_{Schiff base} coordination bond [22].

Evaluating the intraligand bond distances of the pch chelator; the bond orders of the ketonic C8-O2 [1.235(7) Å] and ether C-O [C15-O1 = 1.370(5) Å and C14-O1 = 1.383(6) Å] bonds are readily distinguishable. As a result of the formation of the ruthenium-carbene bond, the C15-C7 bond distance of 1.433(7) Å is not similar to the delocalized C-C double bonds within the phenyl ring [e.g. C16-C17 = 1.377(4) Å] but the C15-C7 bond is still shorter than the C7-C8 [1.455(7) Å] and C8-C9 [1.481(8) Å] single bonds. In contrast to the observation of the C15-C17 double bond, the uncoordinated analogous bond [1.362(4) Å] of *fac*-[Re(CO)₃(bsch)Cl] (bsch = 2-benzothiazole-4*H*-chromen-4-one) were comparable to delocalized C-C double bonds within its corresponding chromone phenyl ring [23]. Ruthenium complexes containing chromone moieties are rare in the literature. Among the few examples are the ruthenium(II) complexes salts, [Ru(bpy)₂(MCMIP)]²⁺ (bpy = bipyridine) and [Ru(phen)₂(MCMIP)]²⁺ (phen = phenanthroline) containing the bidentate neutral chromone chelator, 2-(6-methyl-3-chromonyl)imidazo[4,5-*f*][1,10]-phenanthroline (MCMIP) [24].

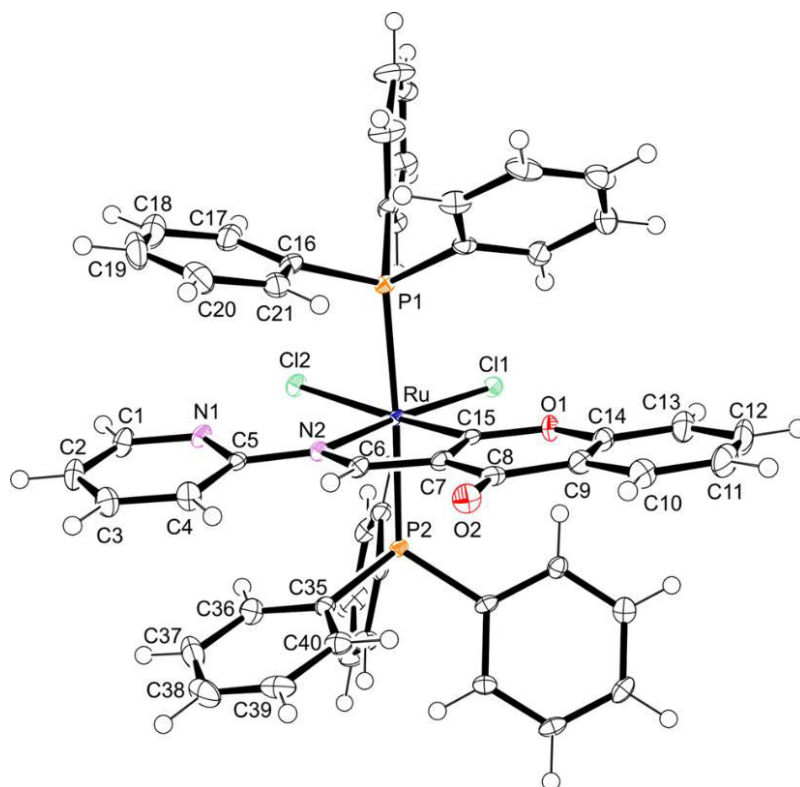


Figure 4.13: An ORTEP view of complex 1 showing 50 % probability displacement ellipsoids and the atom labelling.

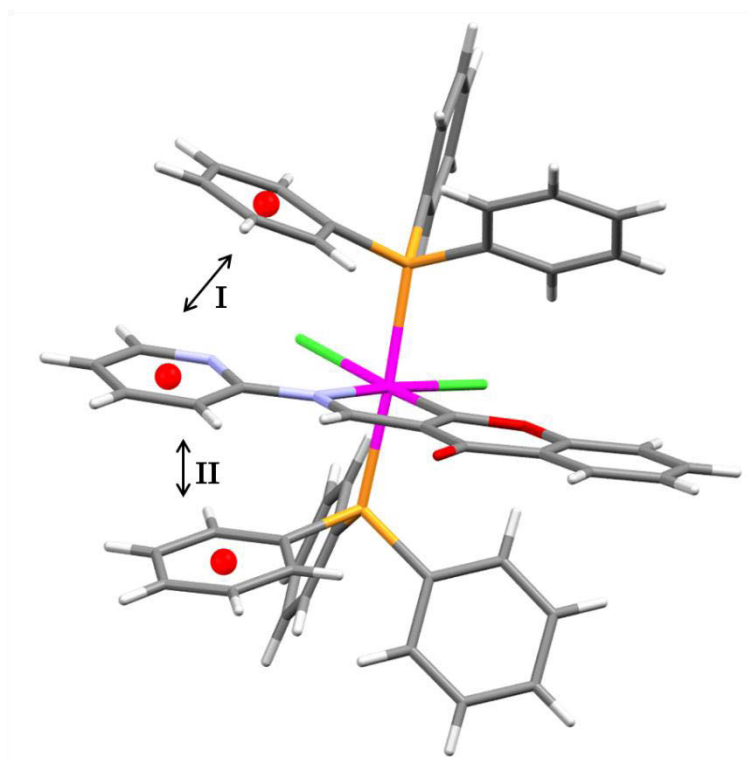


Figure 4.14: Demonstration of the intramolecular interactions occurring in complex **1**; given as **I** = 3.729 Å and **II** = 3.663 Å.

(b) Crystal Structure of **2** · CHCl₃

The triclinic unit cell of **2** contained one molecule of **2** as well as two chloroform molecules of recrystallization, see **Figure 4.15**. The intermolecular interaction (at 3.912 Å) between the bridging pyridyl rings of respective molecules within each triclinic unit-cell allows all the molecules within the crystal lattice to pack in columns parallel to the *[a]*-axis. The crystal lattice of **2** is stabilized by a series of intramolecular interactions between the antipyrine moiety and respective phenyl rings of the triphenylphosphine co-ligand, see **Figure 4.16** {**I** = 4.308 Å, **II** = 3.515 Å and **III** = 3.817 Å}. Noticeably, the intermolecular interactions **I** and **II** differ considerably which could potentially be due to the non-classical interactions between one of the chloroform molecules of recrystallization and the ketonic O1 atom [O1 ... Cl2S = 3.091(3) Å]. In turn, the nature of the aforementioned intermolecular interaction results in the different Ru-N3/N5 [2.125(3) Å/2.105(3) Å] bond distances of **2**.

The other coordination sphere bonds of **2** were as expected with a Ru^{II}-N_{pyridyl} bond length of 1.945(3) Å. As expected, the Ru-P bonds of **2** [2.3155(8) Å] are shorter in comparison to the nearly equidistant *trans*-axial [Ru-P1 = 2.393(1) Å and Ru-P2 = 2.391(1) Å] bonds of **1** due to the increase in the Lewis acidic character of the latter's ruthenium centre. Octahedral distortion is induced by the constrained equatorial N3-Ru-N4 [78.4(1)^o] and N4-Ru-N5 [78.2(1)^o] bite angles of the bpap chelator. This results in the N3-Ru-N5 [156.6(1)^o] and N4-Ru-Cl1 [174.07(9)^o] bond angles deviating from octahedral ideality. The linear deviation of the axial P-Ru-Cl2 [176.99(3)^o] bond angle is due to the influence of the intramolecular interactions **I-III**. The hybridization of the nitrogens (for **2**) is further supported by the Schiff base bond distance [C12-N3 = 1.313(4) Å and C18-N5 = 1.311(5) Å for **4**] which is comparable to other chelating Schiff base moieties coordinated to the ruthenium(II) core [25, 26]. However, the effect of cyclometallation in **2** causes the C-N_{Schiff base}-C angles [C10-N3-C12 = 115.4(3)^o and C18-N5-C19 = 114.8(3)^o] to be inconsistent with respect to the expected 120^o value.

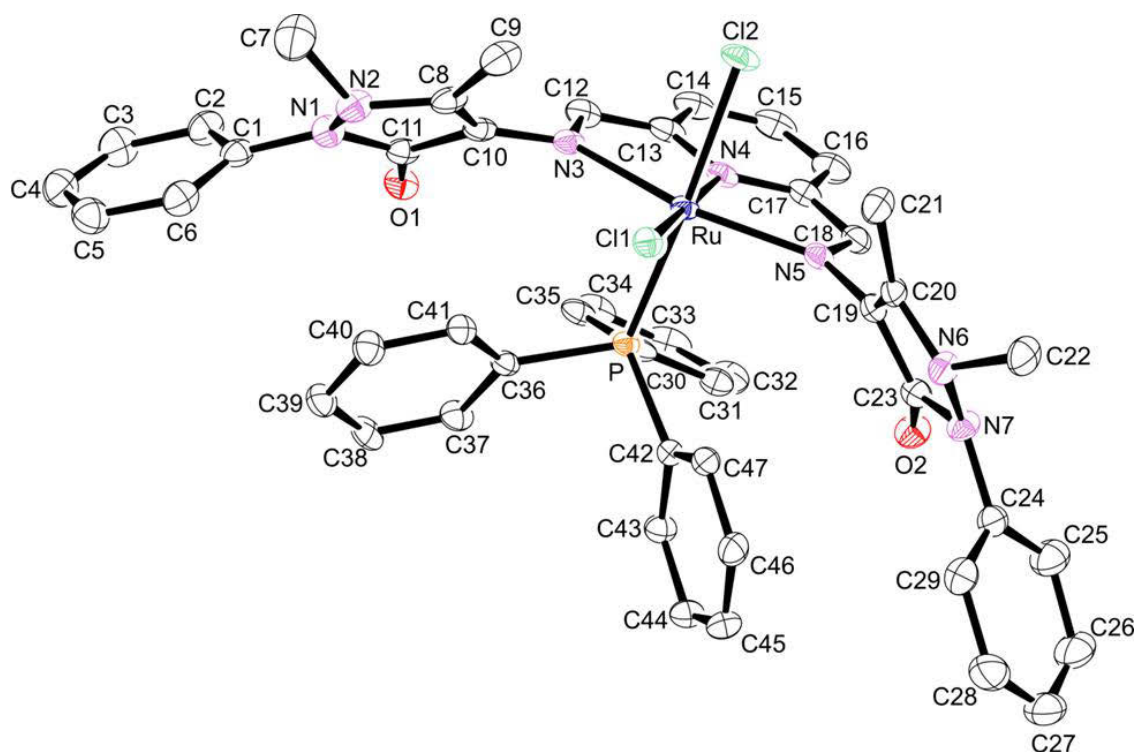


Figure 4.15: An ORTEP view of complex **2** showing 50 % probability displacement ellipsoids and the atom labelling. The hydrogen atoms were omitted for clarity.

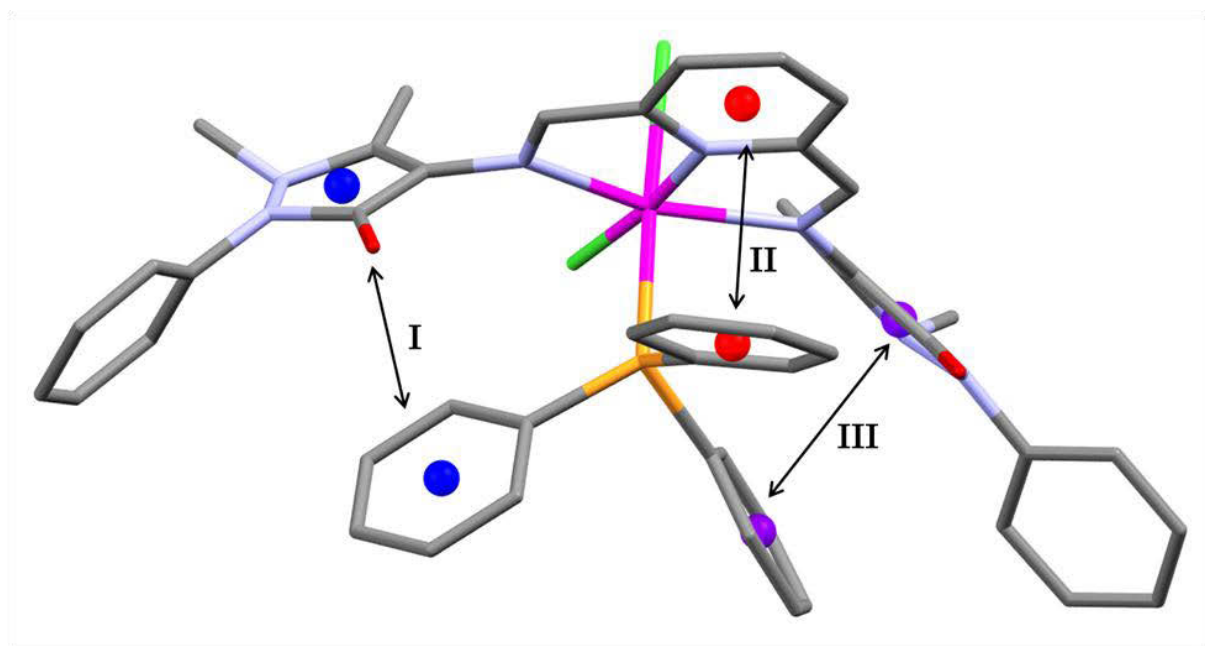


Figure 4.16: *Demonstration of the intramolecular interactions occurring in complex 2; given as **I** = 4.308 Å, **II** = 3.515 Å and **III** = 3.817 Å.*

Table 4.1: *Crystal data and structure refinement data.*

	1 2CHCl ₃	2 CHCl ₃
Chemical formula	C ₅₃ H ₄₁ Cl ₈ N ₂ O ₂ P ₂ Ru	C ₄₉ H ₄₄ Cl ₈ N ₇ O ₂ PRu
Formula weight	1184.49	1178.55
Temperature(K)	100(2)	100(2)
Crystal system	Monoclinic	Triclinic
Space group	P2 ₁ /c	P-1
Unit cell dimensions (Å, °)	$a = 15.4971(10)$	$a = 13.0192(6)$
	$b = 16.9324(12)$	$b = 15.9070(8)$
	$c = 20.7864(13)$	$c = 16.3224(8)$
	$\alpha = 90$	$\alpha = 102.418(2)$
	$\beta = 111.254(2)$	$\beta = 107.355(2)$
	$\gamma = 90$	$\gamma = 104.596(2)$
Crystal size (mm)	0.31 x 0.10 x 0.02	0.28 x 0.15 x 0.10
V(Å ³)	5083.42	2964.18
Z	4	2
Density (calc.) (Mg/m ³)	1.548	1.320
Absorption coefficient (mm ⁻¹)	0.836	0.693
F(000)	2396	1196
θ range for data collection (deg)	1.41; 26.01	1.39; 26.04
Index ranges	$-18 \leq h \leq 19$ $-20 \leq k < 20$ $-25 \leq \ell \leq 12$	$-16 \leq h \leq 15$ $-19 \leq k < 19$ $-20 \leq \ell \leq 20$
Reflections measured	46039	38865
Observed reflections [$I > 2\sigma(I)$]	9818	11388
Independent reflections	7974	9986
Data/Restraints/parameters	7974/0/613	9986/0/617
Goodness of fit on F^2	1.035	1.073
Observed R , wR^2	0.0557; 0.1534	0.0494; 0.1252
R_{int}	0.049	0.025

Table 4.2: Selected bond lengths [\AA] and bond angles [$^\circ$] for **1**.

Ru-Cl1	2.452(1)
Ru-Cl2	2.575(1)
Ru-N2	2.151(4)
Ru-C15	1.933(5)
Ru-P1	2.393(1)
Ru-P2	2.391(1)
N2-C6	1.338(6)
C8-O2	1.235(7)
C15-O1	1.370(5)
C14-O1	1.383(6)
C7-C15	1.433(7)
C7-C8	1.455(7)
C8-C9	1.481(8)
N2-Ru-C15	78.6(2)
Cl1-Ru-Cl2	88.55(4)
P1-Ru-P2	176.31(4)
C6-N2-C5	116.3(4)

Table 4.3: *Selected bond lengths [\AA] and bond angles [$^\circ$] for 2.*

Ru-N3	2.125(3)
Ru-N5	2.105(3)
Ru-Cl1	2.4448(9)
Ru-Cl2	2.4420(8)
Ru-P	2.3155(8)
Ru-N4	1.945(3)
C12-N3	1.313(4)
C18-N5	1.311(5)
C10-N3	1.410(5)
C19-N5	1.409(5)
N3-Ru-N4	78.4(1)
N4-Ru-N5	78.2(1)
N3-Ru-N5	156.6(1)
N4-Ru-Cl1	174.07(9)
P-Ru-Cl2	176.99(3)
C10-N3-C12	115.4(3)
C18-N5-C19	114.8(3)

4.5 References:

1. Mahle, F., da Rosa Guimarães, T., Meira, A.V., Corrêa, R., Cé Bella Cruz, R., Cruz, A.B., Nunes, R.J., Cechinel-Filho, V., de Campos-Buzzi, F. *Eur. J. Med. Chem.*, 2010, **45**, 4761.
2. Parveen, M., Malla, A.M., Yaseen, Z., Ali, A., Alam, M. *Photochem. Photobiol. B, Biol*, 2014, **130**, 179.
3. Rosu, T., Negoiu, M., Pasculescu, S., Pahontu, E., Poirier, D., Gulea, A. *Eur. J. Med. Chem.*, 2010, **45**, 774.
4. Remes, C., Paun, A., Zarafu, I., Tudose, M., Caproiu, M.T., Ionita, P., *Bioorg. Chem.*, 2012, **41 - 42**, 6.
5. Legoabe, L.J., Petzer, A., Petzer, J.P. *Bioorg. Med. Chem. Lett.*, 2012, **22**, 5480.
6. Wang, B., Yang, Z., Lü, M., Hai, J., Wang, Q., Chen, Z. *J. Organomet. Chem.*, 2009, **694**, 4069.
7. Raman, N., Sobha, S. *Spectrochim. Acta. Part A*, 2012, **85**, 223.
8. Mahalingam, V., Chitrapriya, N., Fronczek, F.R., Natarajan, K. *Polyhedron*, 2010, **29**, 3363.
9. Raja, G., Butcher, R.J., Jayabalakrishnan, C. *Spectrochim. Acta, Part A.*, 2012, **94**, 210.
10. Padmaja, M., Pragathi, J., Kumari, C.G. *J. Chem. Pharm. Res.*, 2011, **3**, 602.
11. Liu, Y., Chao, H., Yuan, Y., Yu, H., Ji, L. *Inorg. Chim. Acta.*, 2006, **359**, 3807.
12. Bruker APEX2, SAINT and SADABS. Bruker AXS Inc. (2010) Madison, Wisconsin, USA.
13. Sheldrick, G.M. *Acta Cryst.*, 2008, **A64**, 112.
14. Farrugia, L.J. *J. Appl. Cryst.*, 2012, **45**, 849.
15. Krishna, E.R., Reddy, P.M., Sarangapani, M., Hanmanthu, G., Geeta, B., Rani, K.S., Ravinder, V. *Spectrochim. Acta, Part A.*, 2012, **97**, 189.
16. Khan, M.M.T., Srinivas, D., Kureshy, R.I., Khan, N.H. *Inorg. Chem.*, 1990, **12**, 2320.
17. Balasubramanian, K.P., Karvembu, K., Prabhakaran, R., Chinnusamy, V., Natarajan, K. *Spectrochim. Acta, Part A.*, 2007, **68**, 50.

18. Wilton-Ely, J.D.E.T., Wang, M., Honarkhah, S.J., Tocher, D.A. *Inorg. Chim. Acta*, 2005, **358**, 3218.
19. Matos, C.P., Valente, A., Marques, F., Adão, P., Robalo, M.P., de Almeida, R.F.M., Pessoa, J.C., Santos, I., Garcia, M.H., Tomaz, A.I. *Inorg. Chim. Acta*, 2013, **394**, 616.
20. Booysen, I.N., Abimbola, A., Munro, O.Q., Xulu, B. *Polyhedron*, 2014, <http://dx.doi.org/10.1016/j.poly.2014.02.009>.
21. Raveendran, R., Pal, S. *J. Organomet. Chem.*, 2007, **692**, 824.
22. Nagaraju, K., Pal, S. *J. Organomet. Chem.*, 2013, **737**, 7.
23. Booysen, I., Ismail, M., Akerman, M. *J. Coord. Chem.*, 2013, **66**, 4371.
24. Liu, Y., Chao, H., Yuan, Y., Yu, H., Ji, L. *Inorg. Chim. Acta*, 2006, **359**, 3807.
25. Seth, D.K., Gupta, P. *Polyhedron*, 2012, **31**, 167.
26. Lalrempuia, R., Kollipara, M.R., Carroll, P.J. *Polyhedron*, 2003, **22**, 605.

Chapter 5

Isolation of Ruthenium Compounds from the Analogous Chelating Behaviour of 2-Hydroxyphenylbenz(imidazole/othiazole)

5.1 Introduction

The upsurge in the medicinal inorganic chemistry of ruthenium emanates from the discovery of the potent anti-metastatic cancer activity for NAMI-A, *trans*-[Ru^{III}Cl₄(DMSO)(Im)](ImH) {ImH = imidazole} [1, 2]. Emphasis on using derivatives of imidazole has led to the isolation of new candidates for metallopharmaceuticals, like *trans*-[Ru^{III}(Ind)₂Cl₄][IndH] (KP1019, Ind = indazole) which showed a different biodistribution pattern compared to NAMI-A whereby KP1019 induces apoptosis for the treatment of larger tumors [3]. These startling findings has prompted the use of benz(imidazole/othiazole) analogues due to their diverse biological activities, see **Figure 5.1** [4 - 8].

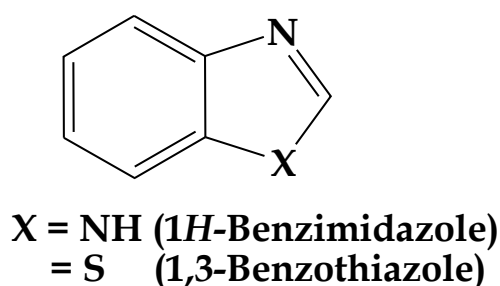


Figure 5.1: Structures of Benzothiazole and Benzimidazole.

For example, among the numerous ruthenium compounds with benz(imidazole/othiazole) moieties is the arene ruthenium(II) complex, [Ru(η^4 -C₈H₁₂)(Hpybz)Cl₂] (Hpybz = 2-pyridylbenzimidazole) which exhibited high antiamoebic activity against the *in-vitro* culture of *Entamoeba histolytica* [9]. In addition,

the organometallic ruthenium(II) complex, $[(\eta^6\text{-arene})\text{Ru}(\text{Hpzbs})\text{Cl}]\text{PF}_6$ (Hpzbs = 2-(1*H*-pyrazol-5-yl)benzothiazole) exhibited high *in vivo* anticancer activity towards Dalton's Lymphoma Ascites tumour cells [10]. These profound and diverse biological activities of this class of ruthenium complexes are largely owed to their diverse coordination environments [11]. Recently, a research study reported the formation of benz(imidazole/othiazole) ruthenium(II/III) compounds with diverse structural features despite the similar structured ligands [12, 13].

In this chapter, the isolation of novel ruthenium compounds from the analogous chelating behaviour of 2-hydroxyphenylbenz(imidazole/othiazole) ligands, 2-hydroxyphenyl-1*H*-benzimidazole (Hobz) and 2-hydroxyphenyl-1*H*-benzothiazole (Hobs), are reported (see **Figure 5.2**). As a result, the diamagnetic ruthenium(II) complex salt, $[\text{RuCl}(\text{Hobz})_2(\text{PPh}_3)]\text{Cl}$ (**1**) and paramagnetic ruthenium complex, $[\text{Ru}^{\text{III}}\text{Cl}(\text{obs})_2(\text{PPh}_3)]$ (**2**) were formed. Although both heterocyclic chelators have similar structures and analogous chelating behaviour (*viz.* N,O bidentate moieties), the Hobz chelators in **1** coordinated as a neutral bidentate N,O moieties while each obs ligand in **2** acted as a monoanionic bidentate N,O moiety resulting in ligand-induced oxidation of the metal centre.

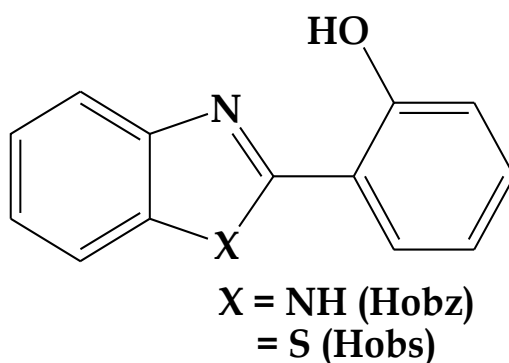


Figure 5.2: Generic structure of the heterocyclic ligands: 2-hydroxyphenyl-1*H*-benzimidazole (Hobz) and 2-hydroxyphenyl-1*H*-benzothiazole (Hobs).

5.2 Experimental

5.2.1 Synthesis of $[RuCl(Hobz)_2(PPh_3)]Cl$ (1)

A two molar ratio of Hobz (0.044 g, 0.208 mmol) was added to a one molar ratio of *trans*- $[RuCl_2(PPh_3)_3]$ (0.100 g, 0.104 mmol) in 20 cm³ ethanol. The resultant reaction mixture was then heated until reflux for 4 hours and then filtered. XRD quality dark green cubic crystals were grown over several days from the slow evaporation of the mother liquor. Yield = 78 % based on Ru, m.p. = 334.5 - 335 °C. IR (ν_{max}/cm^{-1}): $\nu(O-H)$ 3424 (m), $\nu(N-H)$ 3057 (m), $\nu(C=N)$ 1477, 1431 (s), $\nu[Ru-(PPh_3)]$ 692 (vs). ¹H NMR (295K/*d*²-CD₂Cl₂/ ppm): 7.78 (br, s, 1H, N2H; N4H), 7.69 – 7.52 (m, 15H, *PPh*₃), 7.50 – 7.38 (m, 8H, H2, H3, H4, H5, H15, H16, H17, H18), 7.28 – 7.20 (m, 8H, H9, H10, H11, H12, H22, H23, H24, H25), 5.79 (br, s, 2H, O1H, O2H); ³¹P NMR (295K/ *d*²-CD₂Cl₂/ppm): 27.93. UV-Vis (DMF, λ_{max} (ε, M⁻¹cm⁻¹)): 224 nm (2129); 254 nm (17063); 277 nm (sh, 12614); 291 nm (16537); 299 nm (16539); 346 nm (11174); 484 (16706); 709 nm (2129). Conductivity (DCM, 10⁻³ M): 172.89 ohm⁻¹ cm⁻² mol⁻¹.

5.2.2 Synthesis of $[Ru^{III}Cl(obs)_2(PPh_3)]$ (2)

A 1:2 molar ratio reaction between *trans*- $[RuCl_2(PPh_3)_3]$ (0.100 g, 0.104 mmol) and Hobs (0.047 g, 0.208 mmol) conducted in 20 cm³ methanol at reflux temperature for 4 hours. Afterwards, the mother liquor was allowed to cool to room temperature, filtered and after several days of slow evaporation, blue cubic crystals were grown which were suitable for X-ray analysis. Yield = 75 % based on Ru, m.p. = 234.7 – 235.9 °C. IR (ν_{max}/cm^{-1}): $\nu(C=N)$ 1482, 1433 (s), $\nu[Ru-(PPh_3)]$ 692 (vs). UV-Vis (DMF, λ_{max} (ε, M⁻¹cm⁻¹)): 254 nm (9795); 262 nm (10287); 293 nm (20072); 302 nm (sh, 17037); 317 nm (24913); 351 (21778). Conductivity (DCM, 10⁻³ M): 44.05 ohm⁻¹ cm⁻² mol⁻¹.

5.3 X-Ray Crystallography

The X-ray data for both the metal complexes were recorded on a Bruker Apex Duo equipped with an Oxford Instruments Cryojet and an Incoatec microsource operating at 30 W power and 100(2) K. The data was reduced with the programme SAINT [14] and solved by direct methods using the SHELXS-97 [15] and WINGX [16] programmes. All non-hydrogen atoms were located in the difference density map and refined anisotropically with SHELXL-97 [15]. All hydrogen atoms were included as idealised contributors in the least squares process. Their positions were calculated using a standard riding model with C-H_{aromatic} distances of 0.93 Å and $U_{\text{iso}} = 1.2 U_{\text{eq}}$. The benzimidazole N-H bond of the Hobz ligands for compound **1** were located in the difference density map and refined isotropically.

5.4 Computational Details

Computational calculations were conducted with the Gaussian 09W software package [17]. The geometries of **1** and **2** were optimized at the DFT level using the B3LYP functional and the LANL2DZ basis set [18, 19, 20]. Prior to the calculation on compound **1**, the counterion was removed and the resultant structure was used as the starting conformer. Good agreement was found between the optimized and geometrical parameters (refer to **Tables 5.4–5.6**) with the minor deviations due to the fact that gas phase optimized structures does not account for non-classical hydrogen bonding interactions or any short distance contacts.

5.5 Results and Discussion

5.5.1 Synthesis, Spectroscopic Characterization and Computational Studies

The ruthenium compounds, $[\text{RuCl}(\text{Hobz})_2(\text{PPh}_3)]\text{Cl}$ (**1**) and $[\text{Ru}^{\text{III}}\text{Cl}(\text{obs})_2(\text{PPh}_3)]$ (**2**) were isolated from the 1:2 molar reactions of *trans*- $[\text{RuCl}_2(\text{PPh}_3)_2]$ with 2-hydroxyphenylbenzimidazole (Hobz) and 2-hydroxyphenylbenzothiazole (Hobs), respectively. The neutral (for **1**) and monoanionic (for **2**) N,O-donor bidentate moieties coordinates in a '2+2' manner while the remaining coordination sites are occupied by the triphenylphosphine and chloride co-ligands (see **Figure 5.3**). The high isolation yields of metallic compounds in its crystalline form indicate that the major products were isolated. Furthermore, despite the similar skeletal structures of the free heterocyclic ligands, the aforementioned's different stereoelectronic properties are emphasized by the formation of diamagnetic ruthenium(II) and a paramagnetic ruthenium(III) compounds, respectively. The dark green and blue crystals of the complexes are insoluble in alcoholic media but readily dissolve in chlorinated solvents as well as high boiling point aprotic solvents including dimethylformamide and dimethylsulfoxide. The high molar conductivity value of **1** affirms that it is a 1:1 electrolyte in dichloromethane [21].

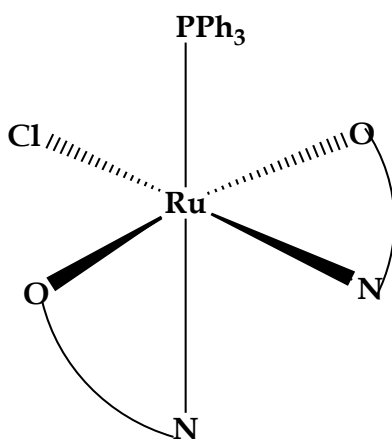


Figure 5.3: Coordination modes of the 2-hydroxyphenylbenz(imidazole/othiazole) ligands.

The ^1H NMR spectral analysis of the diamagnetic complex **1** (see **Figure 5.5**) showed that the aromatic signals proton signals of Hobz chelators coalesced into two multiplets (at 7.50 – 7.38 ppm and 7.28 – 7.20 ppm) which occurred originally as a doublet, two triplets and two multiplets within the proton spectrum of the free-ligand. The broad singlets of the benzimidazole moieties (7.78 ppm) for **1** are found more up-field with respect to its aromatic protons while the phenolic protons resonate more down-field at 5.79 ppm. These signals are also shifted upon coordination as they were originally found at 13.20 ppm and 5.41 ppm within the proton spectrum of the free ligand. ^{31}P NMR spectroscopy confirmed the presence of the phosphorous atoms in **1** (see **Figure 5.6**).

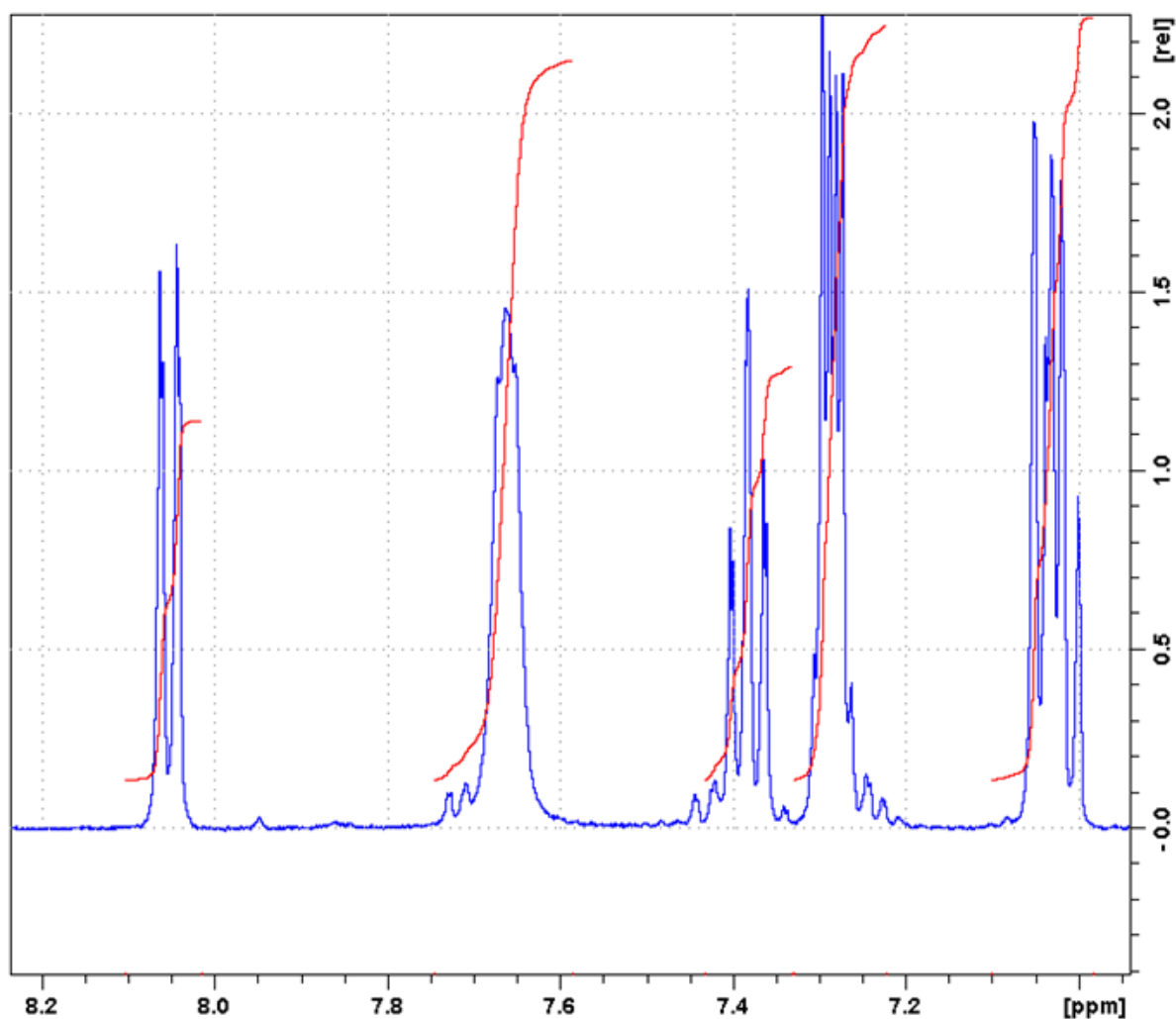


Figure 5.4: ^1H NMR spectrum of the free ligand, Hobz in the range of 7.08 and 8.22 ppm.

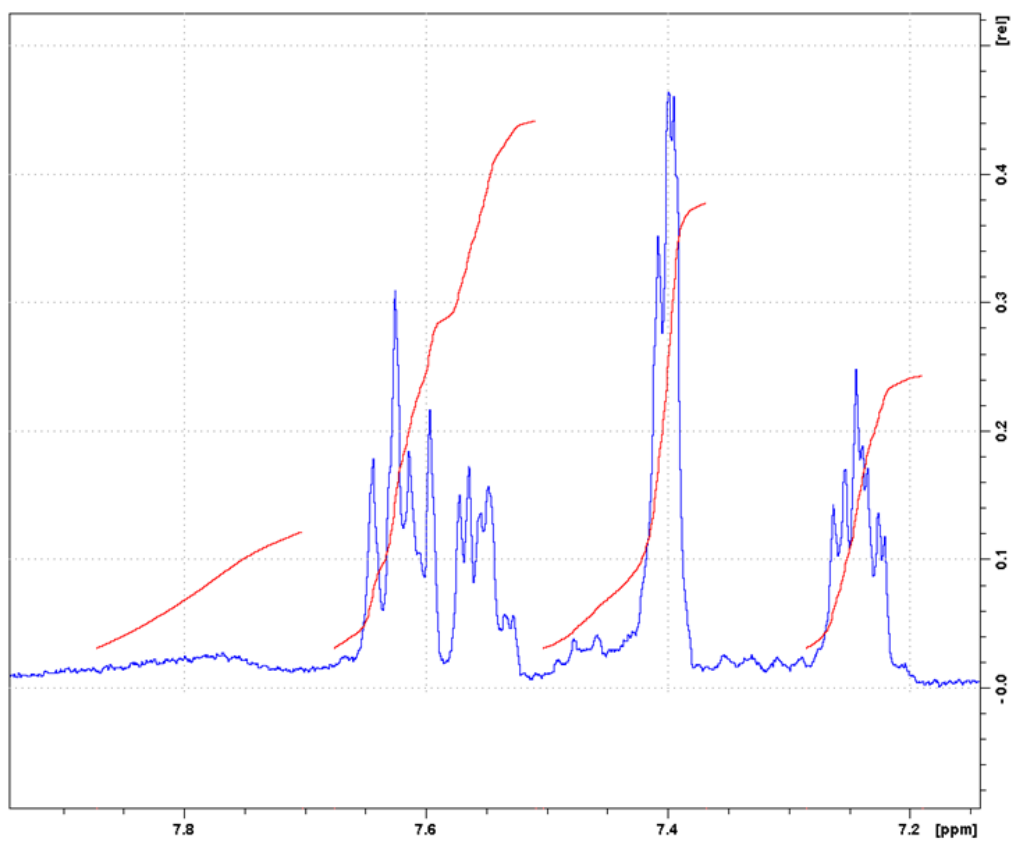


Figure 5.5: ^1H NMR spectrum of compound **1** in the range of 7.18 and 7.86 ppm.

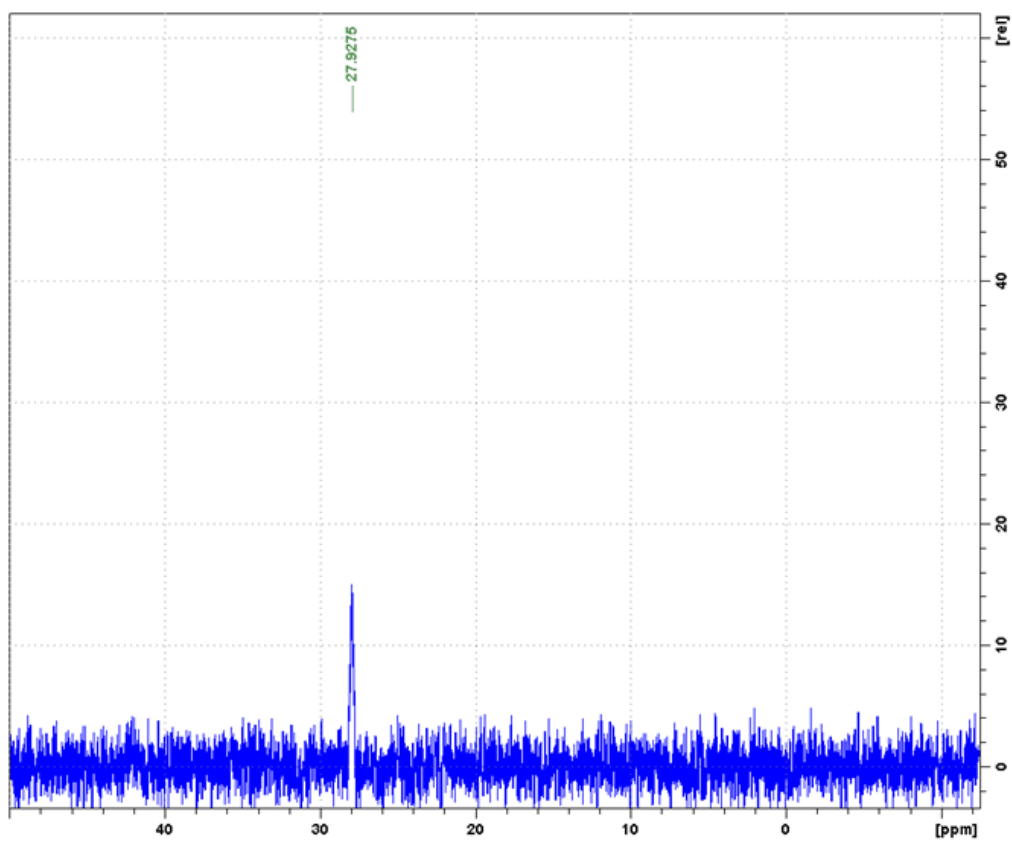


Figure 5.6: ^{31}P NMR spectrum of compound **1**.

Coordination of the heterocyclic chelators is confirmed by the $\nu(\text{C}=\text{N})$ bands (1477 cm^{-1} , 1431 cm^{-1} for **1** and 1482 cm^{-1} , 1433 cm^{-1} for **2**) vibrating at lower frequencies compare to that of the free ligands (1607 cm^{-1} , 1593 cm^{-1} for Hobz and 1620 cm^{-1} , 1584 cm^{-1} for Hobs) (see **Figures 5.7** and **5.8**). This finding is also supported by the absence of the hydroxyl vibrational band in **2** which affirms the obs chelators coordinate as monoanionic moieties. In contrast, the $\nu(\text{O}-\text{H})$ and $\nu(\text{N}-\text{H})$ of the neutral Hobz ligand of **2**, appears as two medium-intensity bands at 3424 cm^{-1} and 3057 cm^{-1} , respectively. Another distinctive feature of the IR spectra for the metallic compounds, is the $\nu[\text{Ru}(\text{PPh}_3)]$ bands which vibrates at 692 cm^{-1} .

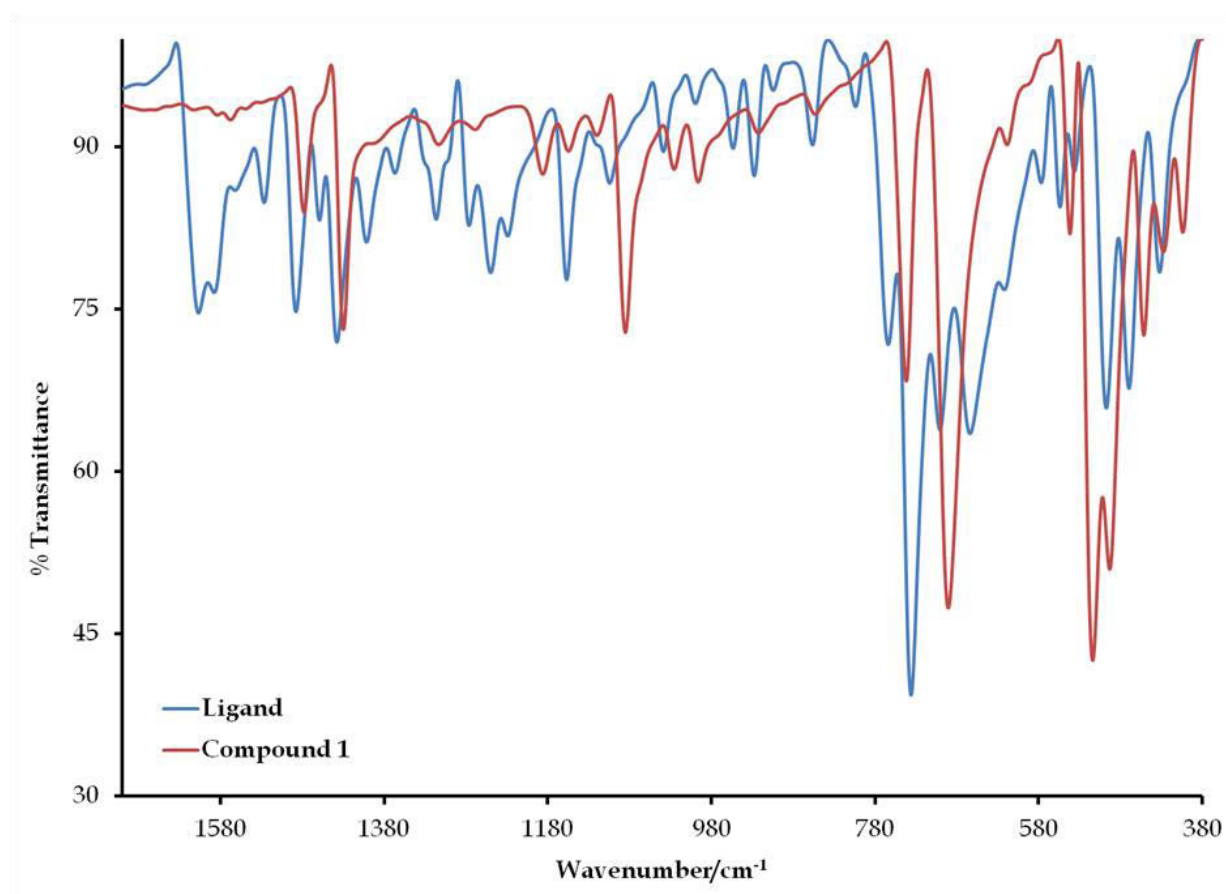


Figure 5.7: Overlay IR spectra of the free-ligand, Hobz and complex **1** between 1750 and 650 cm^{-1} .

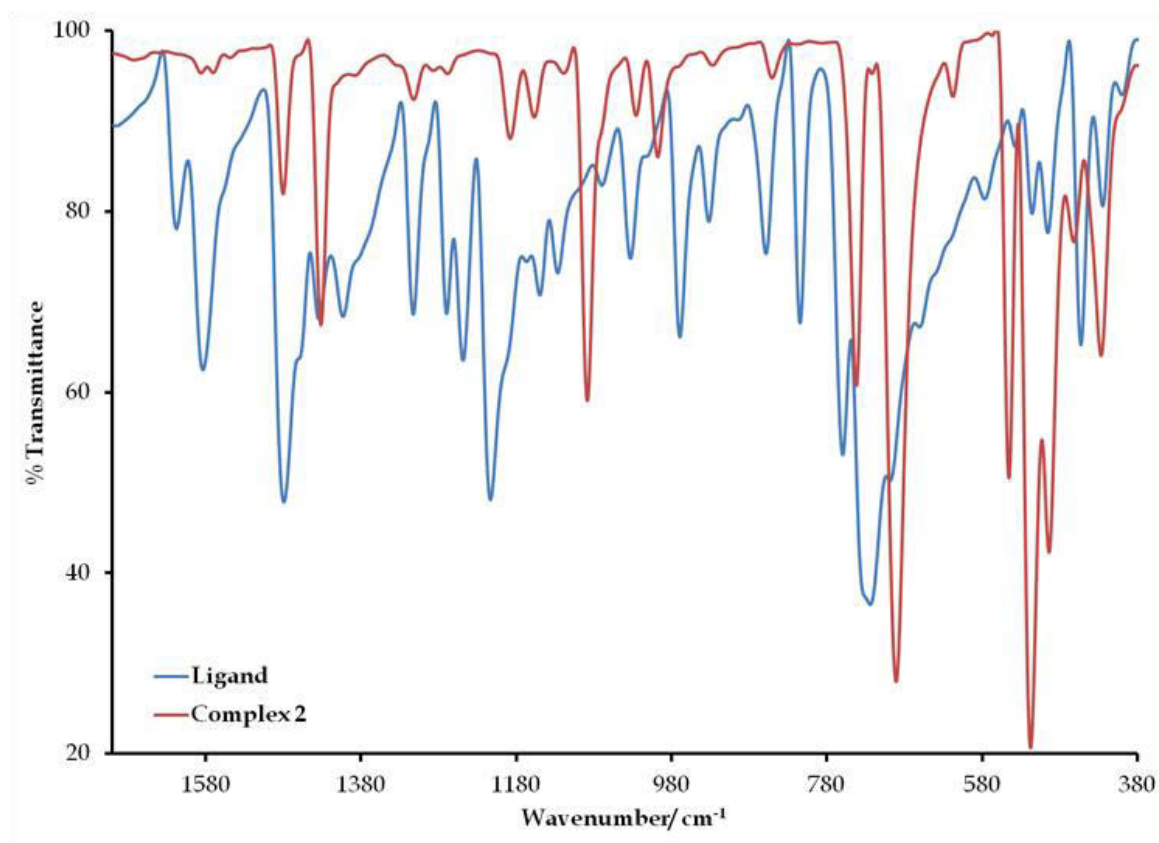


Figure 5.8: Overlay IR spectra of the free-ligand, Hobs and complex **1** between 1750 and 650 cm^{-1} .

Predominately all the intraligand $\pi\text{-}\pi^*$ transitions of the free ligands are consolidated at similar wavelengths in the electronic spectra of **1** (below 400 nm) and **2** (below 330 nm) (see **Figures 5.9** and **5.10**). However in complex **2**, an intraligand $\pi\text{-}\pi^*$ transition at 351 nm is observed at more blue-shifting regions in comparison to the transition band observed at 372 nm within the UV-Vis spectrum of its free-ligand. Furthermore, the UV-Vis spectrum of **1** showed a Metal-to-Ligand-Charge-Transfer (MLCT) band and a metal-based $d\text{-}d$ transition which occurs at 484 nm and 709 nm, respectively with lower extinction coefficients compared to **2**. The absence of the $d\text{-}d$ transition for the paramagnetic d^5 complex **2** can be explained by the higher computed band-gap energy of the latter in comparison to the complex cation **1** since compound **1** showed a metal-based transition (at 709 nm) experimentally although it is low-spin d^6 -system. Another contributive factor is that the high electron density of the obs chelators (in **2**) observed within the HOMO configuration can potentially promote higher stability in complex **2**.

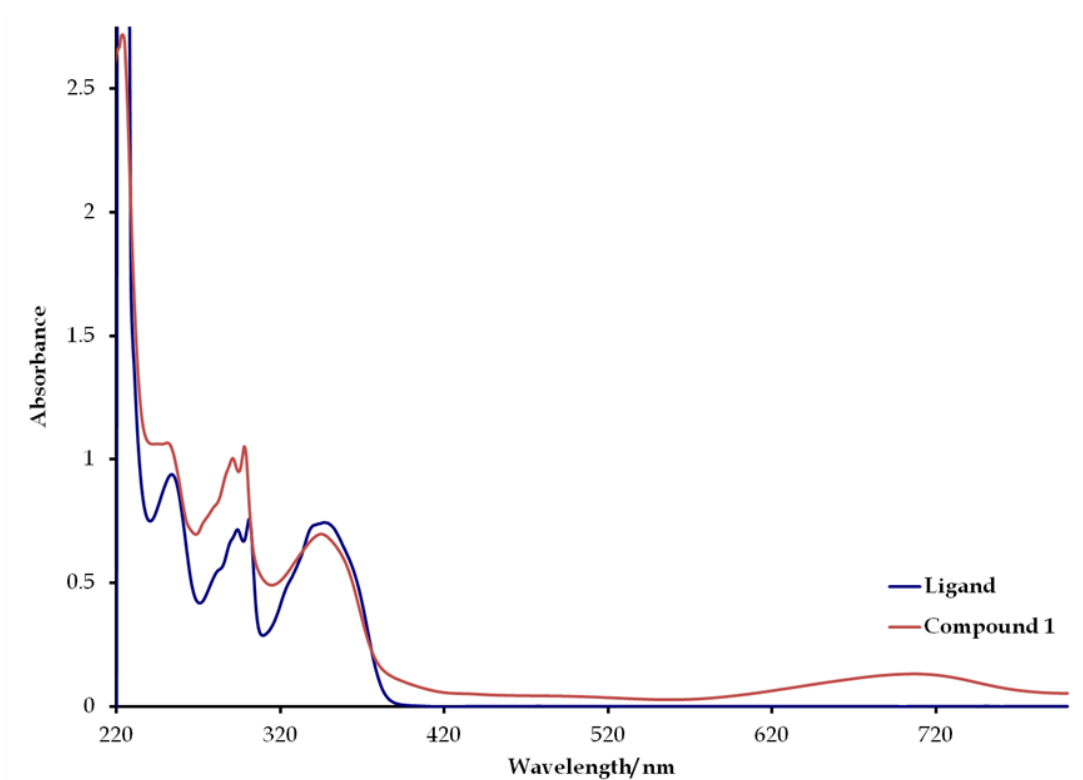


Figure 5.9: Overlay UV/Vis spectra of complex 1 and its ligand, Hobz.

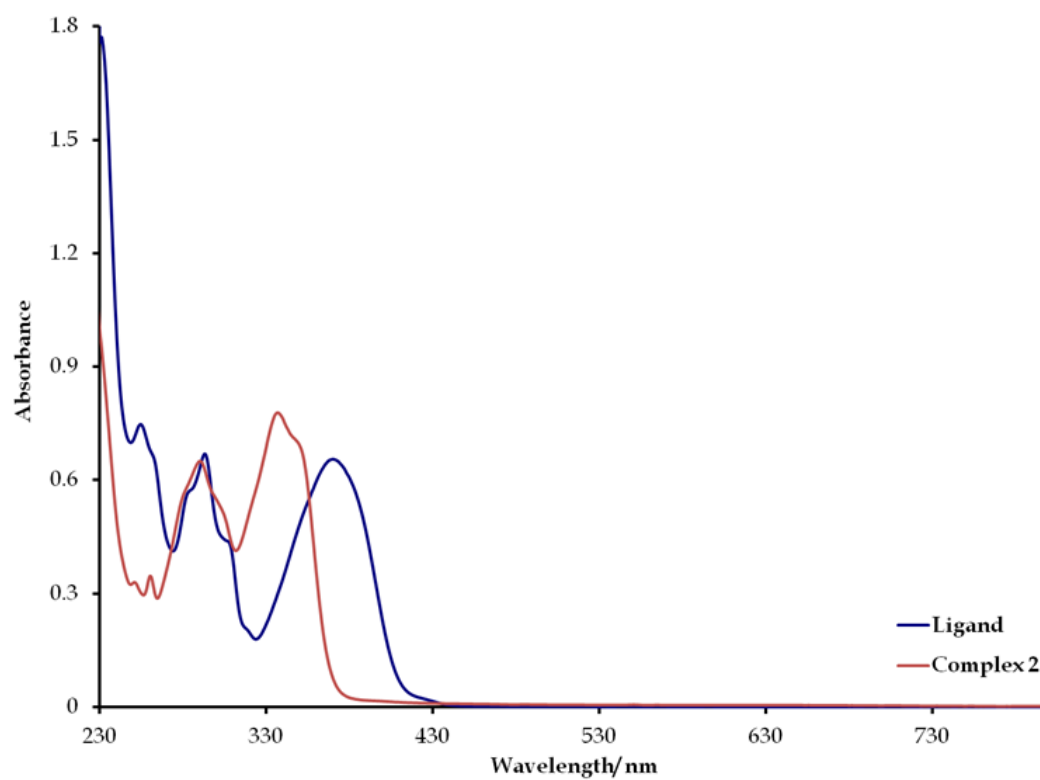
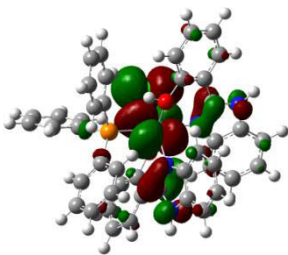
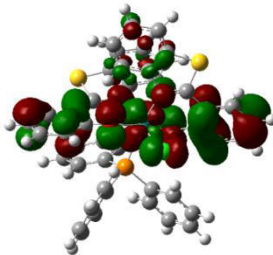
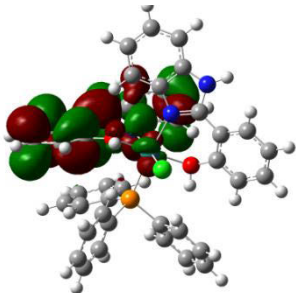
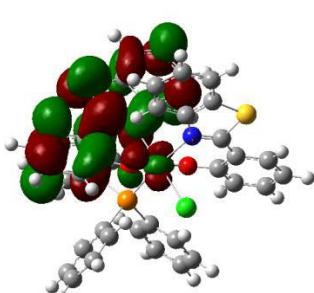


Figure 5.10: Overlay UV/Vis spectra of complex 2 and its ligand, Hobs.

Evaluating the optimized structures of the complex cation **1** and complex **2** (see **Table 5.1**) indicates that the complex cation **1** is energetically more favourable with an energy of -5.948×10^4 eV compared to complex **2** calculated with a total energy of -5.689×10^4 eV. This is also apparent from the lower band-gap energy of 3.189 eV computed for the complex cation of **1**. In complex **2**, the main contributions from the frontier orbitals of the heterocyclic chelators are observed within the Highest Occupied Molecular Orbital (HOMO) configuration. The corresponding frontier orbitals of compound **1** are virtually non-existent in the HOMO configuration while the electron density resides on one heterocyclic chelator in the Lowest Unoccupied Molecular Orbitals (LUMO) configurations of both metallic compounds **1** and **2**. In addition, the HOMO configurations of the optimized structures are also re-enforced by contributions from $2p_z$ and d_{yz} orbitals originating from the chloride co-ligand as well as from the metal atom, respectively.

Table 5.1: The DFT parameters of the complex cation of **1** and complex **2** where the energies is given in electron volts (eV).

	Complex cation of 1	Complex 2
Total Energy	-5.938×10^4	-5.689×10^4
HOMO		
LUMO		
HOMO Energy	-7.523	-5.323
LUMO Energy	-4.334	-2.087
Band-gap	3.189	3.236

ESR spectra of **2** (see Figures 5.11-5.13) were obtained both in the solid state and in dichloromethane at low and room temperatures, refer to Table 5.2. As expected, the influence of the '2+2' coordination modes of the bidentate obs chelators, affords distorted rhombic ESR spectra in the solid state with comparable g -values and these values were found to be similar to other low-spin d^5 ruthenium compounds within distorted octahedral geometries [12]. A classical isotropic singlet (g -value = 2.116) was attained for the liquid sample (at 298 K) but the frozen liquid sample (at 77 K) showed three distinctive signals owing to slower spin-lattice relaxation rates of the latter. In addition, the larger hyperfine coupling constants of the liquid samples in comparison to that of the solid samples indicates that the spin relaxation life-time of the frozen samples were longer. The low temperature ESR parameters of **2** in dichloromethane were similar to what was obtained for the diimine ruthenium(III) complex, [Ru(naphprop)Cl(CO)]; H₂naphprop = *bis*-(naphthaldehyde)propylenediimine in DMF at 77 K [22].

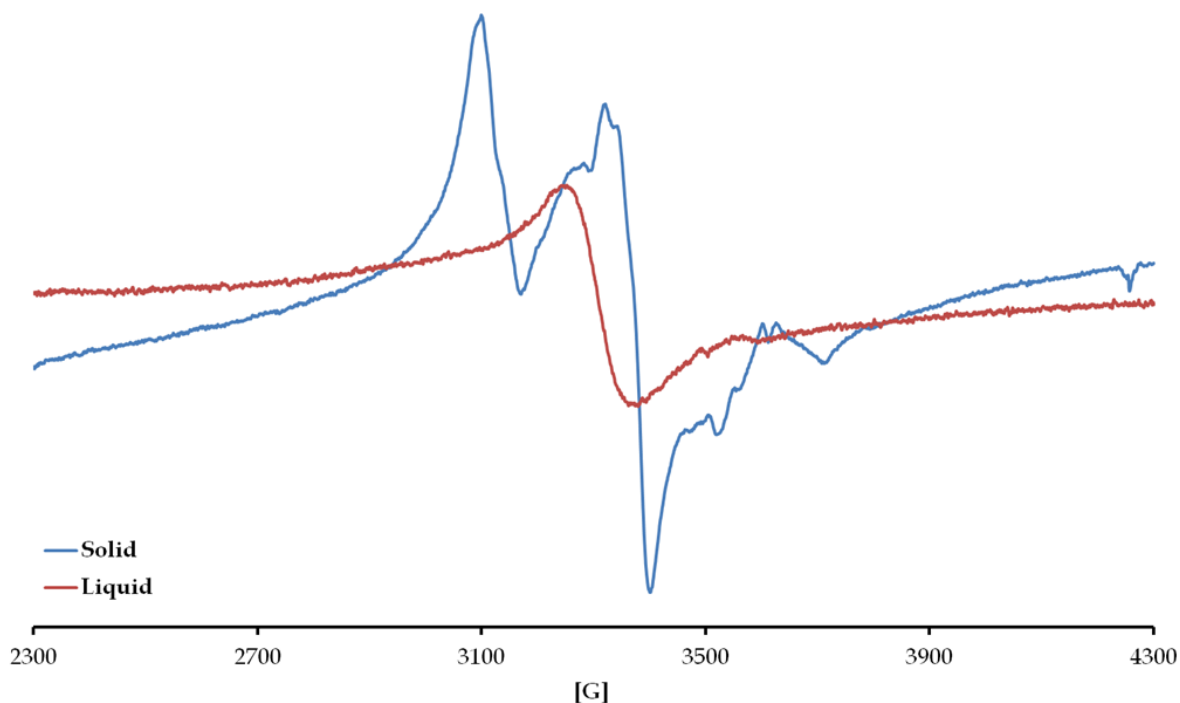


Figure 5.11: ESR spectra of the solid and liquid samples of **2** at room temperature.

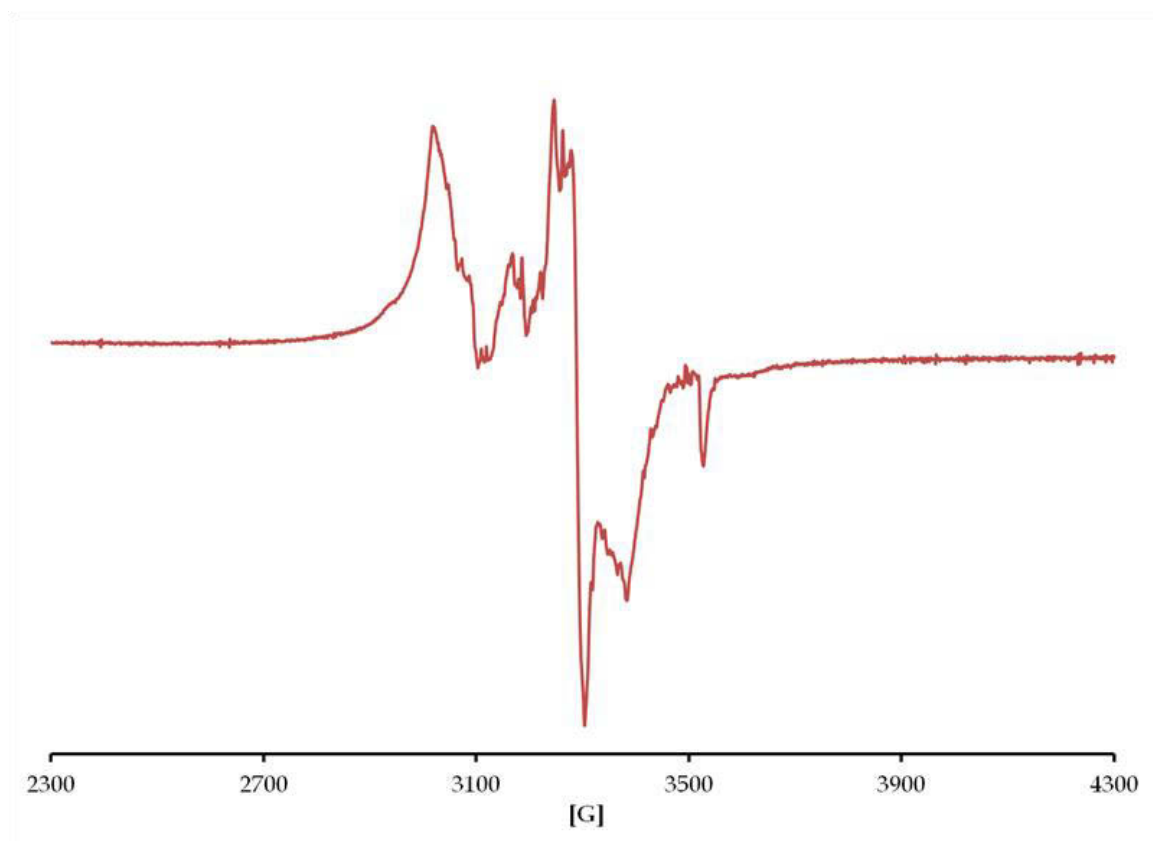


Figure 5.12: *Solid state ESR spectrum of complex 2 at 77 K.*

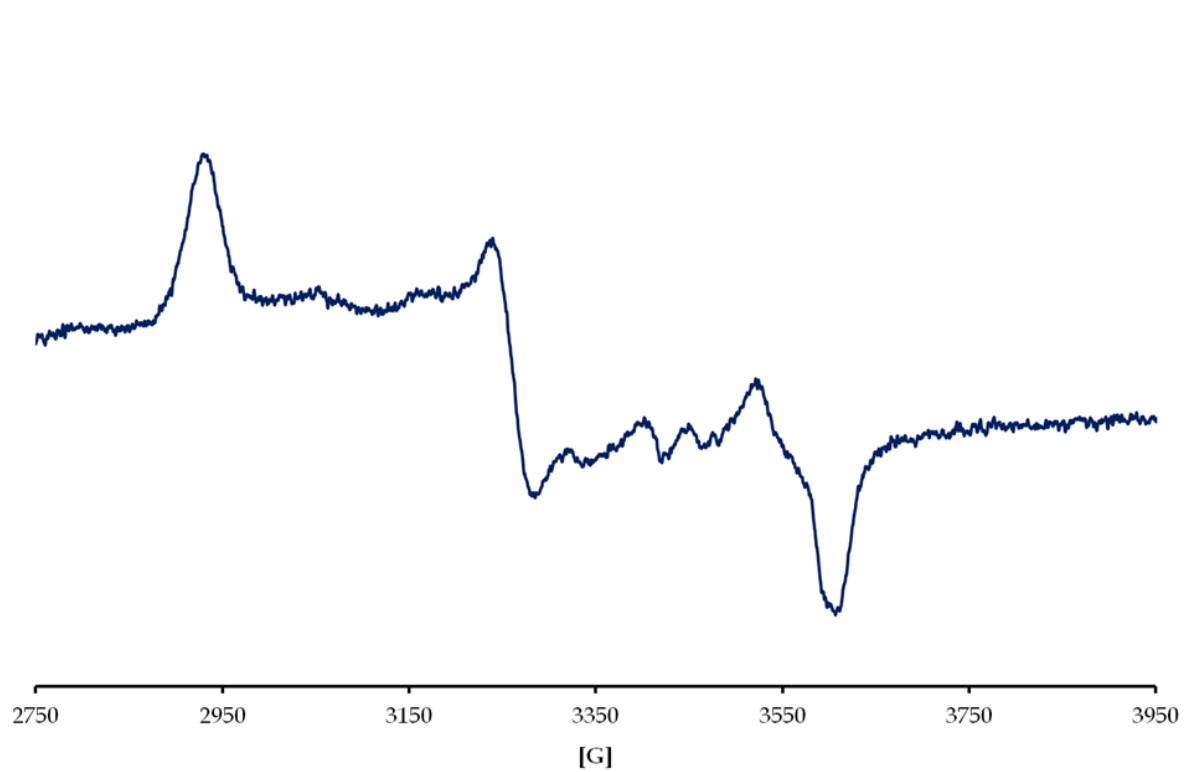


Figure 5.13: *Low temperature liquid ESR spectrum of complex 2.*

Table 5.2: ESR spectral analysis of complex **2** at room (denoted as **A**) and low temperatures (denoted as **B**).

Sample	State of sample	g_x	g_y	g_z	g_{iso}
298 K	Solid	2.267	2.082	1.973	-
	Liquid	-	-	-	2.116
77 K	Solid	2.264	2.0779	1.938	-
	Liquid	2.333	2.096	1.895	-

5.5.2 Electrochemistry

The voltammetric studies of the metallic compounds **1** and **2** showed single reductive redox processes ascribed to the Ru(I/II) and Ru(II/III) redox couple, respectively, see **Figure 5.14**. These redox couples exhibits both diffusion controlled behaviour at incrementing scan rates, see **Figures 5.15** and **5.16**. In addition, peak current ratios approaching one were observed for the respective redox couples which is reminiscent of one electron redox processes. The redox couple of compound **1** is classified as reversible since the peak to peak separation [$\Delta E(\mathbf{1}) = 90 \text{ mV}$] is the same as the standard, ferrocene ($\Delta E = 90 \text{ mV}$). Contrastingly, the peak to peak separation of compound **2** [$\Delta E = 80 \text{ mV}$] is smaller than that of ferrocene which is indicative that the redox couple is quasi-reversible. In addition, the smaller peak to peak separation of compound **1** indicates that it has faster electron transfer kinetics when compared to compound **1** and the standard, ferrocene. These halfwave potentials ($E_{1/2}$) were similar to other ruthenium(II/III) complexes found within literature *e.g.* *trans*-[RuCl(bzp)(PPh₃)₂] Hbzp = *N*-(2-hydroxybenzylidene)-benzimidazole) and the diamagnetic ruthenium complex, *trans*-[Ru(L)(CO)(PPh₃)₂] (H₂L = 4-bromobenzoylhydrazone) with halfwave potentials of 0.70 V and -0.81 V, respectively [12, 23].

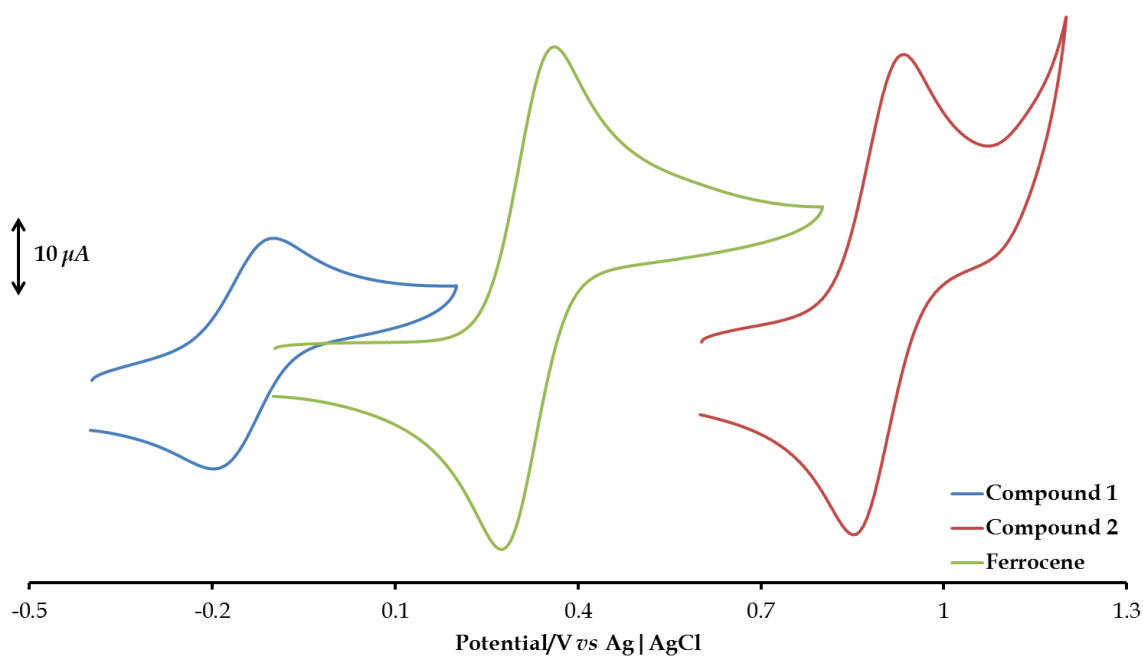


Figure 5.14: Overlay cyclic voltammograms (CVs) of compound **1** (at 300 mV/s), compound **2** (at 300 mV/s) and the standard, ferrocene (at 100 mV/s).

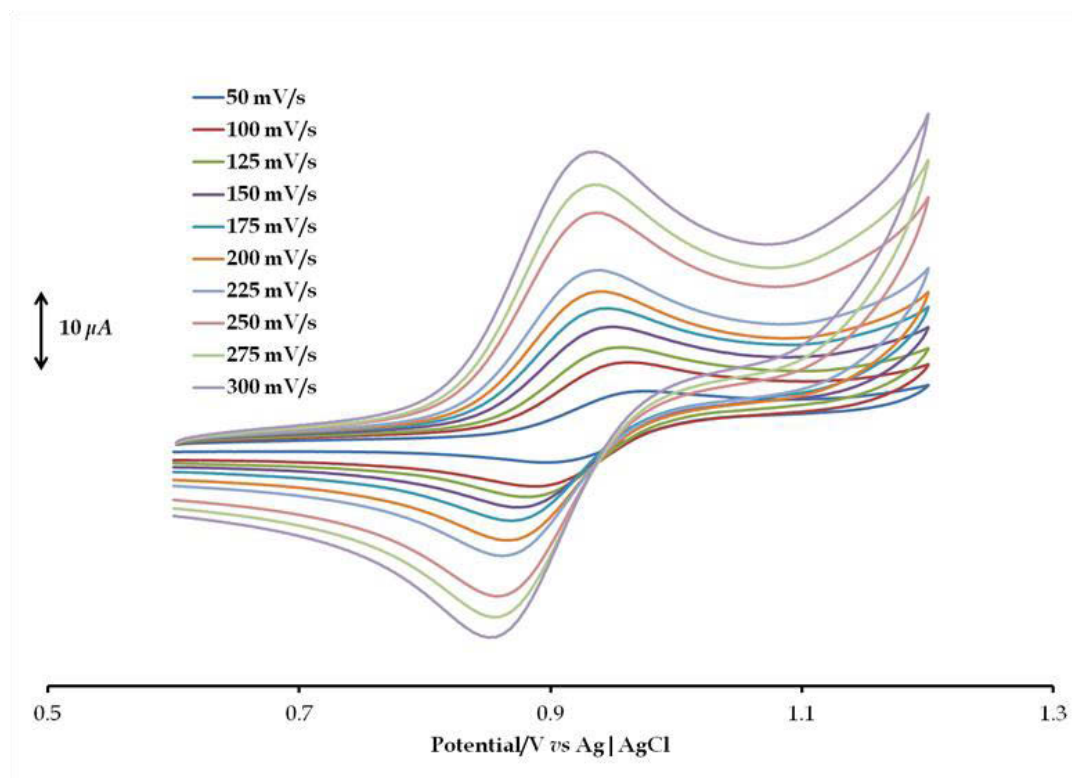


Figure 5.15: Overlay CVs of complex **1** at incrementing scan rates.

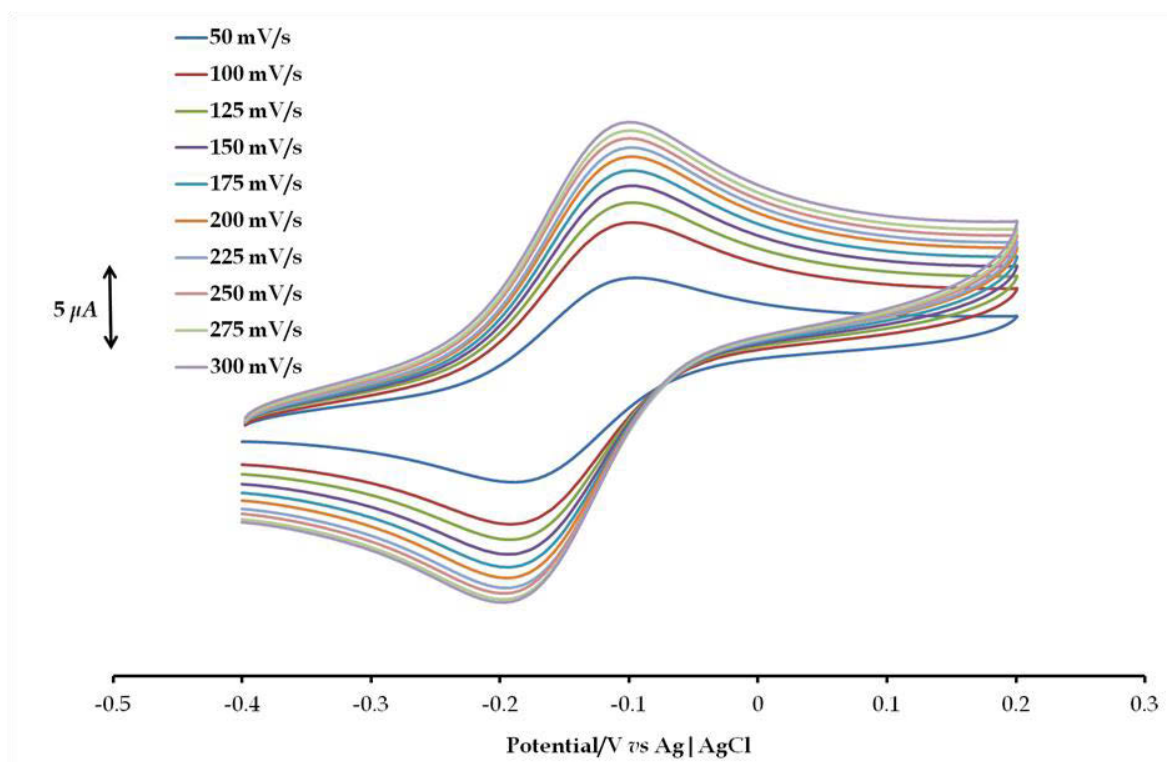


Figure 5.16: Overlay CVs of complex **2** at incrementing scan rates.

5.5.3 Crystal Structures

The mononuclear **1** and **2** compounds crystallize in $P2_1/n$ space-groups whereby their respective monoclinic unit-cells occupy four molecules each. Furthermore, the crystal lattice of **1** is stabilized by classical hydrogen-bonding interactions between the chloride counterions and the benzimidazole N-H groups of adjacent molecules [$\text{NH}\cdots\text{Cl} = 2.47(3) \text{ \AA}$]. In addition, further stabilization is afforded by the interaction between co-planar benzimidazole moieties (interplanar spacings of 3.594 \AA) which are above the distance for classical π - π -stacking interactions at 3.5 \AA . Both the metallic compounds exhibits distorted octahedrons given by the O1-Ru-O2 ($177.12(7)^\circ$ for **1** and $177.98(6)^\circ$ for **2**), N3-Ru-P ($173.65(5)^\circ$ for **1** and $174.18(5)^\circ$ for **2**) and N1-Ru-Cl1 ($172.40(5)^\circ$ for **1** and $173.40(6)^\circ$ for **2**) angles deviating from linearity. The non-ideal octahedral angles are accounted to the constrained O1-Ru-N1 ($86.11(7)^\circ$ for **1** and $87.31(7)^\circ$ for **2**) and O2-Ru-N2 ($85.69(7)^\circ$ for **1** and $87.48(7)^\circ$ for **2**) bite angles which

affords the RuO1C1C6C7N1 and RuO2C14C19C20N2 6-membered chelate rings (see **Figures 5.17** and **5.18**).

As expected, the Ru-N/O coordination bonds of **1** (Ru-N1 = 2.049(2) Å, Ru-N2 = 2.090(2) Å, Ru-O1 = 1.951(2) Å and Ru-O2 = 1.960(2) Å) is shorter than the corresponding bonds of **2** (Ru-N1 = 2.079(2) Å, Ru-N2 = 2.139(2) Å, Ru-O1 = 1.984(1) Å and Ru-O2 = 2.003(1) Å) which is ascribed to the higher Lewis character of the ruthenium centre in **2**. In contrast, the longer Ru-P and Ru-Cl bond lengths of **1** (Ru-P = 2.3811(8) Å and Ru-Cl = 2.4049(7) Å) in comparison to **2** (Ru-P = 2.3437(7) Å and Ru-Cl = 2.3783(6) Å), emanates from the variable stereoelectronic properties of the *trans*-positioned benzimidazole (for **1**) and benzothiazole (for **2**) moieties. Also noticeably, the Ru-N bond distances of **1** and **2** are different due to the difference in *trans*-influence imposed on these coordinated nitrogen atoms.

Surprisingly, the ruthenium atom attached to the deprotonated phenolic oxygen bond distances of **2** was different despite the fact that they are in *trans*-axial positions. However, the Ru-O coordination sphere bond lengths of **1** were similar to coordinated phenolic oxygen bonds found within stereoisomers of [Ru(tolylterpy)(Hpb)(H₂O)]PF₆, tollylterpy = 4'-(4-methylphenyl)-2,2':6',2''-terpyridine, Hpb = 2-hydroxyphenylbenzoxazole with bond distances of 1.9534(18) Å (for the *cis*-stereoisomer) and 1.9623(6) Å (for the *trans*-stereoisomer) [24]. The same applied to the Ru^{III}-O bond distances of **2** which were comparable to analogous bonds found in the paramagnetic Schiff base ruthenium complexes, [Ru(HahsH)(PPh₃)₂Cl₂].2CH₂Cl₂ [Ru-O = 2.023(3) Å] and [Ru(ahsH)(PPh₃)₂Cl₂] [Ru-O = 2.028(4) Å], H₂ahsH = *N*-acetyl-*N'*-(salicylidene)hydrazide [25]. The other coordination sphere bond distances of **1** and **2** were also within range as the corresponding bonds found within literature for ruthenium(II/III) complexes containing benzimidazole or benzothiazole moieties. Like in the case of where the 2-carboxylatebenzimidazole (ocbz) ligands coordinate in a '2+2' fashion as monoanionic N,O-bidentate chelators in the ruthenium(II) complex, *cis*-[Ru(ocbz)₂(PPh₃)₂] with Ru-N bond distances of 2.121(4) Å and 2.129(4) Å [26].

The C=N bonds ($C7-N1 = 1.329(2)$ Å and $C20-N3 = 1.335(2)$ Å) of compound **1** are readily distinguishable from its C7/20-N bonds ($C7-N2 = 1.357(3)$ Å and $C20-N4 = 1.355(3)$ Å) but the similar to the C=N bonds ($C7-N1 = 1.325(3)$ Å and $C20-N2 = 1.311(3)$ Å) found within complex **2** affirming their bond orders. Furthermore, the intraligand C-S ($S1-C7 = 1.728(3)$ Å, $S1-C8 = 1.730(3)$ Å, $S2-C20 = 1.735(2)$ Å and $S2-C21 = 1.733(2)$ Å) bond distances were nearly equidistant showing that the bond orders are one.

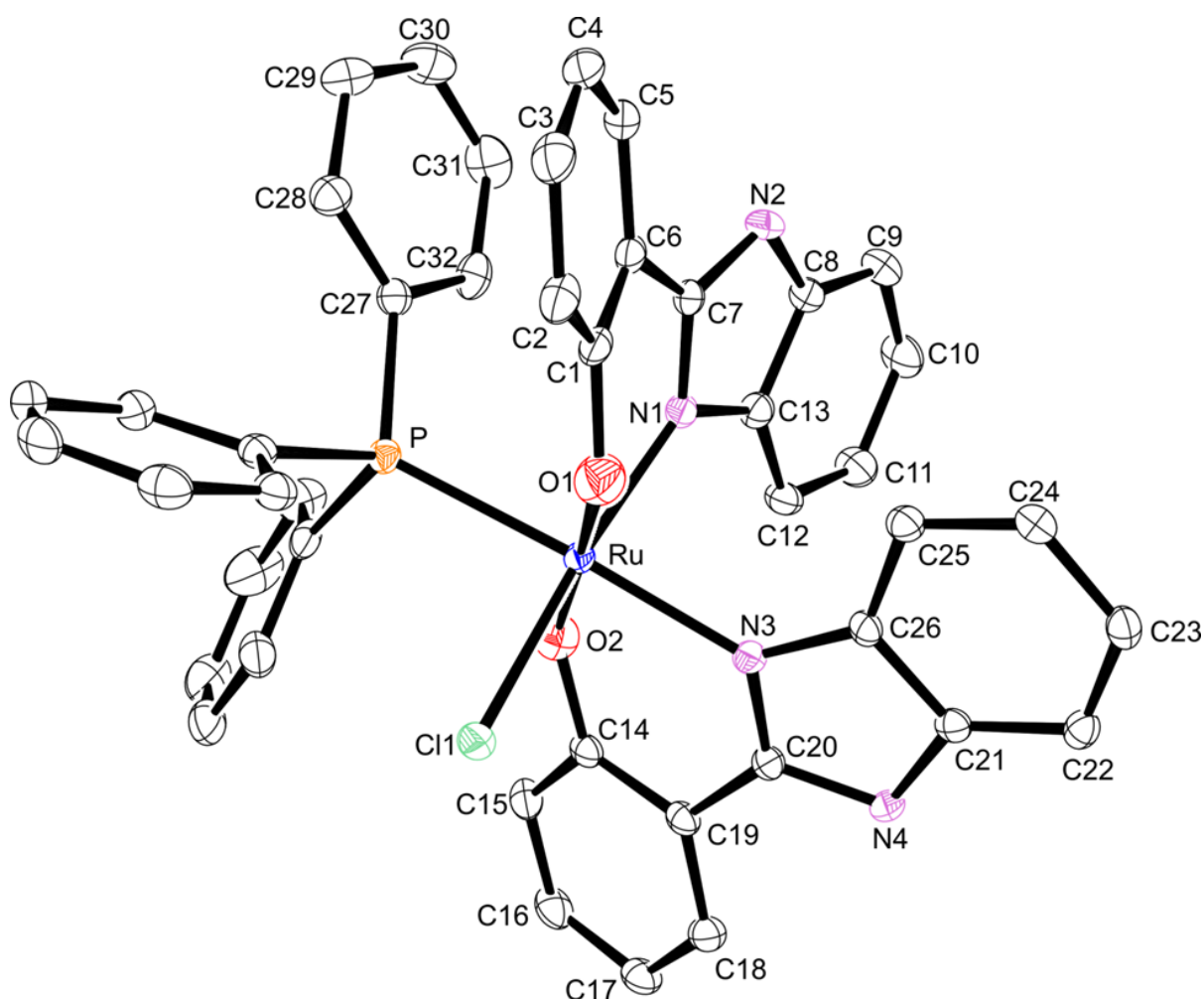


Figure 5.17: An ORTEP view of compound **1** showing 50 % probability displacement ellipsoids and the atom labelling. The hydrogen atoms were omitted for clarity.

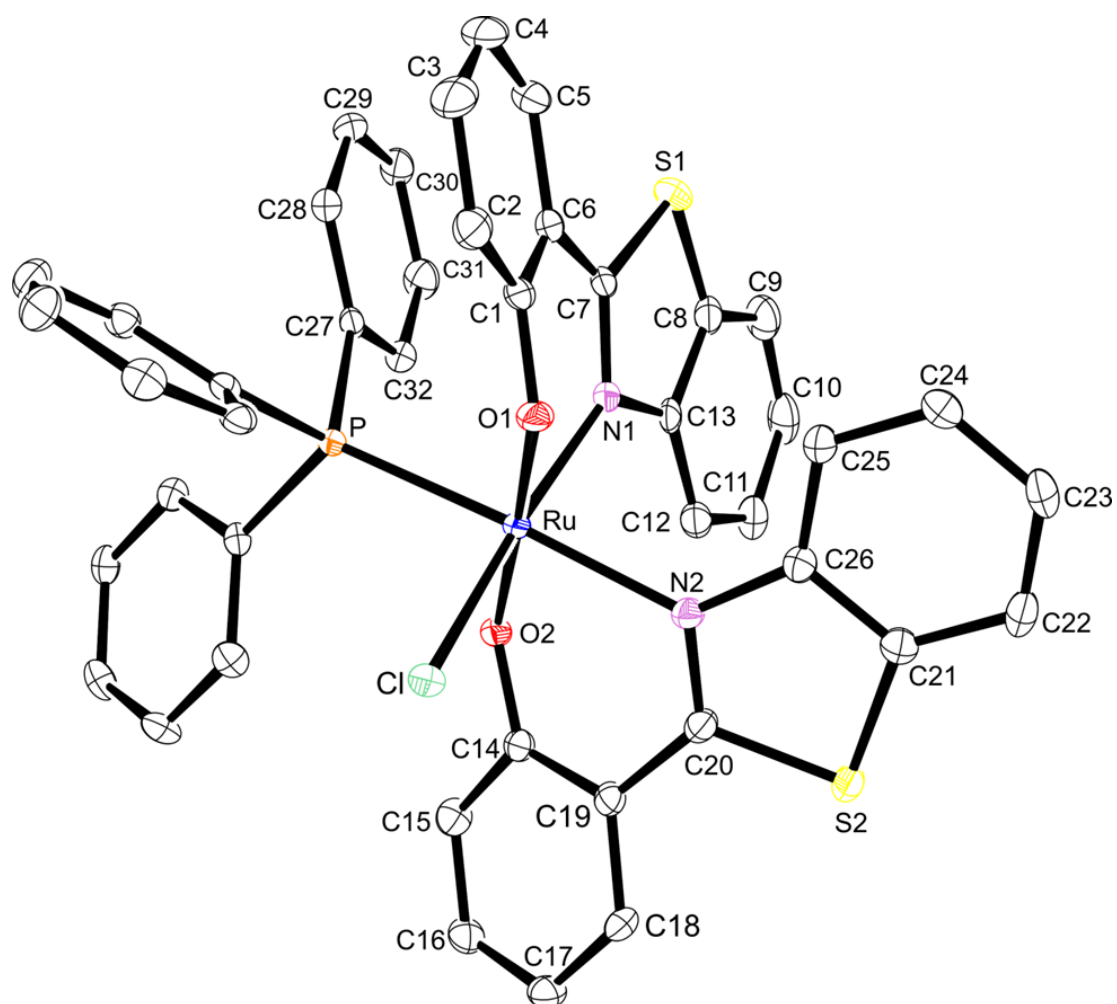


Figure 5.18: An ORTEP view of complex 2 showing 50 % probability displacement ellipsoids and the atom labelling. The hydrogen atoms were omitted for clarity.

Table 5.3: *Crystal data and structure refinement data.*

	1	2
Chemical formula	C ₄₄ H ₃₅ Cl ₂ N ₄ O ₂ PRu	C ₄₄ H ₃₁ ClN ₂ O ₂ PRuS ₂
Formula weight	854.70	851.32
Temperature (K)	100(2)	296(2)
Crystal system	Monoclinic	Monoclinic
Space group	P2 ₁ / <i>n</i>	P2 ₁ / <i>n</i>
Unit cell dimensions (Å, °)	<i>a</i> = 15.647(5)	<i>a</i> = 12.4367(5)
	<i>b</i> = 14.519(5)	<i>b</i> = 22.1300(9)
	<i>c</i> = 18.313(5)	<i>c</i> = 13.4062(5)
	α = 90.000(5)	α = 90.00
	β = 102.540(5)	β = 94.377(2)
	γ = 90.000(5)	γ = 90.00
Crystal size (mm)	0.24 × 0.11 × 0.09	0.21 × 0.17 × 0.09
V(Å ³)	4061.08	3678.95
Z	4	4
Density (calc.) (Mg/m ³)	1.398	1.537
Absorption coefficient (mm ⁻¹)	0.599	0.698
<i>F</i> (000)	1744	1732
θ range for data collection (deg)	1.55; 26.07	1.78; 26.05
Index ranges	-19 ≤ <i>h</i> ≤ 19 -17 ≤ <i>k</i> < 17 -22 ≤ <i>l</i> ≤ 22	-15 ≤ <i>h</i> ≤ 15 -27 ≤ <i>k</i> < 25 -16 ≤ <i>l</i> ≤ 14
Reflections measured	35293	31756
Observed reflections [<i>I</i> > 2σ(<i>I</i>)]	8028	7165
Independent reflections	7104	6012
Data/Restraints/parameters	7104/0/503	6012/0/478
Goodness of fit on <i>F</i> ²	1.057	1.026
Observed <i>R</i> , <i>wR</i> ²	0.0290; 0.0733	0.0288; 0.0618
<i>R</i> _{int}	0.014	0.001

Table 5.4: *Selected bond lengths [\AA] and bond angles [$^\circ$] for 1.*

	Experimental	Optimized
Ru-N1	2.049(2)	2.0880
Ru-N2	2.090(2)	2.1077
Ru-O1	1.951(2)	2.1103
Ru-O2	1.960(2)	2.1750
Ru-P	2.3811(8)	2.5119
Ru-Cl	2.4049(7)	2.5096
N1-C7	1.329(2)	1.3525
N2-C7	1.357(2)	1.3885
N3-C20	1.335(2)	1.3492
N4-C20	1.355(3)	1.3867
O1-Ru-O2	177.12(7)	173.63
N3-Ru-P	173.65(5)	173.74
N1-Ru-Cl1	172.40(5)	167.73
O1-Ru-N1	86.11(7)	86.23
O2-Ru-N2	87.48(7)	85.12

Table 5.6: *Selected bond lengths [\AA] and bond angles [$^\circ$] for 2.*

	Experimental	Optimized
Ru-N1	2.079(2)	2.1470
Ru-N2	2.139(2)	2.1454
Ru-O1	1.984(1)	2.0282
Ru-O2	2.003(1)	2.0811
Ru-P	2.3437(7)	2.5250
Ru-Cl	2.3783(6)	2.4675
N1-C7	1.325(3)	1.3384
N2-C20	1.311(3)	1.3345
S1-C7	1.728(3)	1.8347
S1-C8	1.730(3)	1.8002
S2-C20	1.735(2)	1.8365
S2-C21	1.733(2)	1.8013
O1-Ru-O2	177.98(6)	175.56
N3-Ru-P	174.18(5)	171.03
N1-Ru-Cl1	173.40(16)	173.21
O1-Ru-N1	87.31(7)	86.92
O2-Ru-N2	85.69(7)	87.76

5.6 References:

1. Vadori, M., Pacor, S., Vita, F., Zorzet, S., Cocchietto, M., Sava, G. *J. Inorg. Biochem.*, 2013, **118**, 21.
2. Groessl, M., Reisner, E., Hartinger, C.G., Eichinger, R., Semenova, O., Timerbaev, A.R., Jakupec, M.A., Arion, V.B., Keppler, B.K. *J. Med. Chem.*, 2007, **50**, 2185.
3. Aitken, J.B., Antony, S., Weekley, C.M., Lai, B., Spiccia, L., Harris, H.H. *Metallomics*, 2012, **4**, 1051.
4. Spillane, C.B., Dabo, M.N.V., Fletcher, N.C., Morgan, J.L.F. Keene, F.R., Haq, I., Buurma, N.J. *J. Inorg. Biochem.*, 2008, **102**, 673.
5. Novales, J., Jonkhoff, N., Acquaye, J.H. *Polyhedron*, 2013, **62**, 148.
6. Mei, W., Liu, Y., *Trans. Met. Chem.*, 2006, **31**, 272.
7. Chelopo, M.P., Pawar, S.A., Sokhela, M.K., Govender, T., Kruger, H.G., Maguire, G.E.M. *Eur. J. Med. Chem.*, 2013, **66**, 407.
8. Sampath, K., Jayabalakrishnan, C. *Arabian J. Chem.*, 2013, <http://dx.doi.org/10.1016/j.arabjc.2013.12.017>.
9. Bharti, N., Maurya, M.R., Naqvi, F., Azam, A. *Bioorg. Med. Chem. Lett.*, 2000, **10**, 2243.
10. Gupta, G., Sharma, G., Koch, B., Park, S., Lee, S.S., Kim, J. *New J. Chem.*, 2013, **37**, 2573.
11. Singh, A.K., Pandey, D.S., Xu, Q., Braunstein, P. *Coord. Chem. Rev.*, 2013, <http://dx.doi.org/10.1016/j.ccr.2013.09.009>.
12. Booysen, I.N., Abimbola, A., Munro, O.Q., Xulu, B. *Polyhedron*, 2014, <http://dx.doi.org/10.1016/j.poly.2014.02.009>.
13. Clarke, M.J. *Coord. Chem. Rev.*, 2002, **232**, 69.
14. Bruker APEX2, SAINT and SADABS. Bruker AXS Inc. (2010) Madison, Wisconsin, USA.
15. Sheldrick, G.M. *Acta Cryst.*, 2008, **A64**, 112.
16. Farrugia, L.J. *J. Appl. Cryst.*, 2012, **45**, 849.

17. Frisch, M.J., Trucks, G.W., Schlegel, H.B., Scuseria, G.E., Robb, M.A., Cheeseman, J.R., Scalmani, G., Barone, V., Mennucci, B., Petersson, G.A., Nakatsuji, H., Caricato, M., Li, X., Hratchian, H.P., Izmaylov, A.F., Bloino, J., Zheng, G., Sonnenberg, J.L., Hada, M., Ehara, M., Toyota, K., Fukuda, R., Hasegawa, J., Ishida, M., Nakajima, T., Honda, Y., Kitao, O., Nakai, H., Vreven, T., Montgomery Jr, J.A., Peralta, J.E., Ogliaro, F., Bearpark, M., Heyd, J.J., Brothers, E., Kudin, K.N., Staroverov, V.N., Kobayashi, R., Normand, J., Raghavachari, K., Rendell, A., Burant, J.C., Iyengar, S.S., Tomasi, J., Cossi, M., Rega, N., Millam, J.M., Klene, M., Knox, J.E., Cross, J.B., Bakken, V., Adamo, C., Jaramillo, J., Gomperts, R., Stratmann, R.E., Yazyev, O., Austin, A.J., Cammi, R., Pomelli, C., Ochterski, J.W., Martin, R.L., Morokuma, K., Zakrzewski, V.G., Voth, G.A., Salvador, P., Dannenberg, J.J., Dapprich, S., Daniels, A.D., Farkas, Ö., Foresman, J.B., Ortiz, J.V., Cioslowski, J., Fox, D.J. *Gaussian 09 (Revision A.01)*, 2009, Gaussian Inc., Wallingford CT.
18. Becke A.D. *J. Chem. Phys.*, 1993, **98**, 5648.
19. Mei, W., Liu, Y. *Trans. Met. Chem.*, 2005, **30**, 82.
20. Dunning Jr, T.H., Hay, P.J. *Modern Theoretical Chemistry*, Ed. H. F. Schaefer III, Vol. 3 (Plenum, New York, 1976) 1-28.
21. Rodrigues, C., Batista, A.A., Ellena, J., Castellano, E.E., Benítez, D., Cerecetto, H., González, M., Teixeira, L.R., Beraldo, H. *Eur. J. Med. Chem.*, 2010, **45**, 2847.
22. Khan, M.M.T., Srinivas, D., Kureshy, R.I., Khan, N.H. *Polyhedron*, 1991, **10**, 2559.
23. Prabhu, R.N., Ramesh, R. *J. Organomet. Chem.*, 2012, **718**, 43.
24. Novales, J., Jonkhoff, N., Acquaye, J.H. *Polyhedron*, 2013, **62**, 148.
25. Raveendran, R., Pal, S. *Polyhedron*, 2008, **27**, 655.
26. Małecki, J.G., Maro, A. *Polyhedron*, 2012, **40**, 125.

Chapter 6

Conclusion and Future Work

The foremost objectives of this research study were achieved in terms of the design, synthesis and characterization of novel ruthenium complexes with multidentate N-donor ligands. In all the formulated ruthenium compounds, the metal centres are stabilized by various multidentate N-donor ligands, *e.g.* by Schiff base bearings various biologically significant components including uracil (see Chapter 3), antipyrine or chromone moieties (see Chapter 4). Likewise in chapter 5, the analogous chelating behaviour of 2-hydroxyphenylbenz(othiazole/imidazole) chelators resulted in the characteristic octahedral geometries. Single crystal X-ray analysis of the resultant complexes also revealed that the mono-imine chelators coordinated to the *trans*-[Ru^{II/III}(PPh₃)₂] cores while the highly delocalized diimine and the '2+2' heterocyclic chelators replaced two bulky PPh₃ co-ligands of the metal precursor. The distinctive difference in the structural features of the mono-imine and diimine ruthenium compounds are also reflected in their attained electrochemical properties.

Future work entails exploring the anticancer and antimalarial activities of the formulated ruthenium compounds. Prior to evaluating the anticancer activities of the diimine and '2+2' heterocyclic ruthenium compounds, DNA binding capabilities of the aforementioned metallic compounds will be investigated towards calf thymus (CT)-DNA with the aid of UV/Vis spectroscopy. The prevalence of the bulky *trans-axial* triphenylphosphine co-ligands is clearly problematic for designing potentially new ruthenium anticancer agents. Ruthenium compounds with the bulky *trans*-[Ru(PPh₃)₂] core will not be able to intercalate between the DNA base pairs of the CT-DNA and thus the antimalarial studies will be conducted on these metallic compounds. To combat this design flaw, the ligands used in this study and proposed in the future work will be reacted with the metal precursor, (cymene)ruthenium dichloride dimer (see **Figure 6.1**) since as emphasized in Chapter 1, arene ruthenium(II) compounds have shown excellent DNA capabilities.

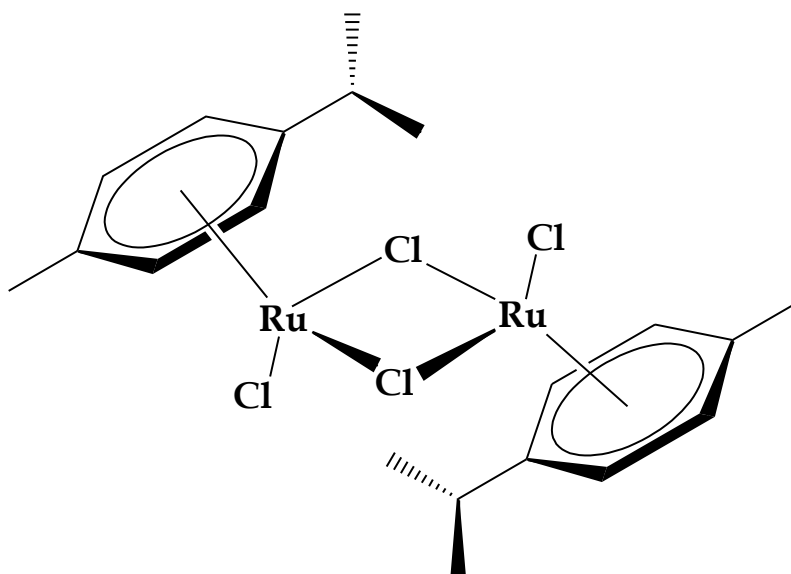


Figure 6.1: Structure of the (cymene)ruthenium dichloride dimer.

The scope of this study will be broadened to include the *bis*-heterocyclic ligands (see **Figure 6.2**) containing the benzothiazole and benzimidazole moieties used in Chapter 5. This should afford an interesting comparative study between the coordination modes as well as the biological activities of the mono- and *bis*-heterocyclic ruthenium compounds. The motivation for using these ligands arises from their ability to coordinate to a vast number of transition metals, as emphasized by their high coordination affinity to the iron(II) and rhenium(V) metal centres [1]. Furthermore, the reduction of the Schiff bases to their corresponding amines may eliminate occurrences of hydrolysis as these ligands are more hydrolytically stable.

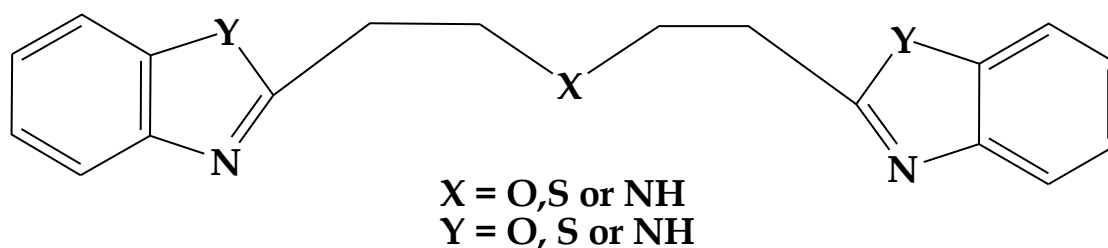


Figure 6.2: Generic structure of the *bis*-heterocyclic ligands.

Finally, not only has this research study produced an improved understanding and new knowledge of the coordination chemistry of ruthenium with biologically relevant Schiff base chelates, but it has also afforded impetus for the development of new ruthenium complexes for therapeutic applications.

Reference:

1. Böca, M., Jameson, R.F., Linert, W. *Coord. Chem. Rev.*, 2011, **255**, 290.